

**Alternative Models for Air Pollutant  
Effects on Visibility**

Thesis by  
Annmarie Eldering

In Partial Fulfillment of the Requirements  
for the Degree of  
Doctor of Philosophy

California Institute of Technology  
Pasadena, California

1994

(Submitted March 16, 1994)

©1994

Annmarie Eldering

All rights reserved

## Acknowledgements

There have been many, many people at Caltech and in the community that have been important to making graduate school a positive and rewarding experience for me. Naturally, my advisor, Dr. Glen Cass, deserves many thanks for his support and encouragement through the vicissitudes of research. His insight, experience in the field, and many useful comments made much of this work possible.

Sue Larson provided the foundation for the image processing-based visibility model, and Jeff Hall and Kevin Hussey of JPL provided invaluable expertise. The trajectory model rests on the shoulders of a number of previous students, particularly Rob Harley. The work of Lynn Hildemann was important to describing the composition of the particulate matter emissions from the air pollution sources studied here. Suzanne Hering was a helpful sounding board, and K.C. Moon was instrumental to obtaining the aerosol size distribution data.

The Center for Air Quality Analysis and the California Air Resources Board provided substantial financial support. Additional fellowships from the Switzer Foundation, Awards for Research College Scientists, and the American Association of University Women were of great usefulness during these years.

I would like to thank my friends at Caltech who helped create a stimulating and amusing environment. My fellow Cass group members were a

great resource for assistance on technical problems, computing problems, and homework problems.

There are many friends outside of the Caltech community who deserve a hearty thanks for their support through the years, among them Erin, T, Zan, and Bridget. The completion of this work was made much more pleasant by the distractions provided by Lisa Maggiore.

## Abstract

Air pollution causes visibility reduction in urban areas such as Los Angeles as well as in national parks and wilderness areas. In this work, alternative mathematical models are formulated that relate air pollutant emissions or ambient air pollutant concentrations to visual range or to changes in the appearance of a scenic vista.

The first model examined connects continuous measurements of airborne particle size distributions to resulting effects on visibility via Mie scattering calculations. The model is tested by application to data taken during the 1987 Southern California Air Quality study. The time series of measured light scattering coefficient values is reproduced well when redundant nephelometer measurements are available to assure that the measured light scattering coefficient values are not in doubt.

A source-oriented model for air pollutant effects on visibility next is assembled that computes light scattering directly from data on gas-phase and primary particle-phase air pollutant emissions from sources. Airborne particle mass concentrations are predicted accurately. The model predictions generally match the measured aerosol size distribution and chemical composition. Good agreement is attained between model predictions and measurements of atmospheric light scattering coefficient values.

An image processing-based visibility model is presented that displays model calculations as synthetic color photographs having the appearance of

a smog event. Beginning with a digitized clear day photograph of the scene of interest, a theoretically based model for light scattering and absorption is used to recalculate sky color and skylight addition between the observer and objects in the field of view in order to predict the appearance of the scene in the presence of heavy smog. Model verification data are collected experimentally, including photographs of chosen vistas and measurements of the atmospheric aerosol chemical composition and size distribution. The model performs well, producing representations of the sky color and objects in the field of view that are close to those seen in actual photographs. This model also is adapted to begin with data on landscape features taken from earth-orbiting satellites combined with digital terrain elevation data, such that the model could be applied on a global scale.

# Contents

|          |   |          |
|----------|---|----------|
| <b>1</b> | <b>Introduction</b>   | <b>1</b> |
| 1.1      | Motivation . . . . .  | 1        |
| 1.2      | Research Objectives . . . . .   | 3        |
| 1.3      | Approach . . . . .  | 4        |
| <b>2</b> | <b>Visibility Modeling Using Continuous Aerosol Size Distribution Monitors</b>                        | <b>7</b> |
| 2.1      | Introduction . . . . .  | 7        |
| 2.2      | Experimental Program . . . . .  | 12       |
| 2.2.1    | Aerosol Size Distributions . . . . .  | 12       |
| 2.2.2    | Aerosol Chemical Composition Measurements . . . . .   | 13       |
| 2.2.3    | Light Scattering Coefficient Data . . . . .   | 15       |
| 2.2.4    | Data Base Preparation . . . . .   | 20       |
| 2.3      | Correction of Aerosol Size Distribution Data Collected by the PMS Optical Particle Counters . . . . . | 21       |
| 2.4      | Creating a Combined Size Distribution for Use in Further Calculations . . . . .                       | 21       |
| 2.5      | Internal Consistency of the Aerosol Chemistry Data Base . . . . .                                     | 24       |
| 2.6      | Examination of the Aerosol Liquid Water Content . . . . .   | 26       |
| 2.7      | Estimation of Refractive Index . . . . .  | 28       |
| 2.8      | Calculation of the Extinction Coefficient . . . . .   | 30       |

|          |  |           |
|----------|--|-----------|
| 2.9      | Visibility Model Results . . . . .                                 | 30        |
| 2.9.1    | Visual Range Results . . . . .                                     | 38        |
| 2.9.2    | Comparison to Empirical Models for Light Scattering .              | 42        |
| 2.10     | Conclusions . . . . .  | 43        |
| <b>3</b> | <b>A Source – Oriented Model for Air Pollutant Effects on Vis-</b> |           |
|          | <b>ibility</b>   | <b>46</b> |
| 3.1      | Introduction . . . . .   | 46        |
| 3.1.1    | Conceptual Formulation of the Problem . . . . .                    | 47        |
| 3.1.2    | Mathematical Modeling of Air Pollutant Effects on Vis-             |           |
|          | ibility . . . . .  | 51        |
| 3.1.3    | Emissions Model . . . . .  | 54        |
| 3.1.4    | Advection . . . . .  | 59        |
| 3.1.5    | Gas Phase Chemical Kinetics . . . . .                              | 59        |
| 3.1.6    | Solar Radiation Fields . . . . .                                   | 60        |
| 3.1.7    | Dry Deposition . . . . .   | 60        |
| 3.1.8    | Diffusion of Gases to and from Particles . . . . .                 | 61        |
| 3.1.9    | Fog Calculations . . . . .   | 63        |
| 3.1.10   | Solution Technique . . . . .                                       | 66        |
| 3.1.11   | Light Scattering . . . . .   | 66        |
| 3.2      | Model Application . . . . .  | 67        |
| 3.2.1    | Particulate Emissions Inventory . . . . .                          | 69        |
| 3.2.2    | Gas-phase Emission Inventory . . . . .                             | 77        |
| 3.2.3    | Initial Conditions . . . . .                                       | 80        |
| 3.2.4    | Mapping the Occurrence of Fog . . . . .                            | 81        |
| 3.2.5    | Fog Calculations . . . . .   | 86        |

|          |  |            |
|----------|--|------------|
| 3.3      | Model Results . . . . .  | 87         |
| 3.3.1    | Gas-phase Species . . . . .                                      | 87         |
| 3.3.2    | Aerosol Mass Concentration . . . . .                             | 89         |
| 3.3.3    | Individual Aerosol Species . . . . .                             | 91         |
| 3.3.4    | Comparison with Impactor Measurements . . . . .                  | 95         |
| 3.3.5    | Aerosol Size Distribution . . . . .                              | 101        |
| 3.3.6    | Light Scattering Coefficient . . . . .                           | 107        |
| 3.4      | Conclusions . . . . .  | 107        |
| <b>4</b> | <b>An Image Processing Based Visibility Model</b>                | <b>111</b> |
| 4.1      | Introduction . . . . .   | 111        |
| 4.2      | Formulation of the Model . . . . .                               | 112        |
| 4.2.1    | Sky Radiance Images . . . . .                                    | 115        |
| 4.2.2    | Object Inherent Radiance Images . . . . .                        | 117        |
| 4.2.3    | Prediction of the Appearance of Regional Haze Episodes           | 119        |
| 4.3      | Experimental Program . . . . .                                   | 119        |
| 4.3.1    | Aerosol Chemical Characterization . . . . .                      | 122        |
| 4.3.2    | Calculation of the Extinction Coefficient . . . . .              | 124        |
| 4.3.3    | Verification of Radiative Transfer Module . . . . .              | 125        |
| 4.4      | Model Application . . . . .                                      | 133        |
| 4.5      | Results . . . . .  | 134        |
| 4.6      | Conclusions . . . . .  | 141        |
| <b>5</b> | <b>A Visibility Model Based on Satellite-Generated Landscape</b> |            |
|          | <b>Data</b>  | <b>142</b> |
| 5.1      | Introduction . . . . .   | 142        |
| 5.2      | Image Processing-based Visibility Models . . . . .               | 143        |

|          |   |            |
|----------|---|------------|
| 5.3      | A New Model: Conceptual Framework . . . . .   | 148        |
| 5.4      | Application . . . . .                         | 149        |
| 5.5      | Evaluation of Model Performance . . . . .     | 153        |
| 5.6      | Conclusions . . . . .                         | 162        |
| <b>6</b> | <b>Conclusions</b>                            | <b>164</b> |
| 6.1      | Summary of Results . . . . .                  | 164        |
| 6.2      | Recommendations for Future Research . . . . . | 168        |
|          | <b>Bibliography</b>                           | <b>169</b> |

## List of Tables

|     |   |     |
|-----|---|-----|
| 2.1 | Sites and Dates of SCAQS Intensive Field Experiments . . . . .  | 11  |
| 2.2 | Methods Used to Assign Size Distributions . . . . .   | 32  |
| 2.3 | Comparison of Modeled Light Scattering Coefficient Values to<br>Nephelometer Measurements of the Light Scattering Coeffi-<br>cient (all data) . . . . . | 36  |
| 3.1 | Sulfur Species Aqueous Oxidation Rate Expressions . . . . .   | 65  |
| 3.2 | PM10 Emissions in the South Coast Air Basin . . . . .   | 74  |
| 3.3 | PM2.5 Emissions in the South Coast Air Basin . . . . .  | 75  |
| 3.4 | Source-Specific PM10 Emissions for the South Coast Air Basin  | 78  |
| 3.5 | Initial Conditions . . . . .  | 82  |
| 3.6 | Analysis of Model Performance . . . . .   | 92  |
| 4.1 | Base Case and Perturbed Inputs to Radiative Transfer Module   | 129 |
| 4.2 | Comparison of Radiometer and Model . . . . .  | 130 |

## List of Figures

|     |   |    |
|-----|---|----|
| 2.1 | Map of the Los Angeles Area . . . . .   | 10 |
| 2.2 | SCAQs Sampler System . . . . .  | 14 |
| 2.3 | Comparison of concurrent light scattering measurements . . .  | 17 |
| 2.4 | An example of the final aerosol size distribution created for<br>use in visibility modeling. . . . .  | 23 |
| 2.5 | An example of the ion balance and aerosol chemistry . . . . .   | 25 |
| 2.6 | Time Series Plots of Scattering Coefficient for Case A . . . . .  | 33 |
| 2.7 | Time Series Plots of Scattering Coefficient for Case C . . . . .  | 35 |
| 2.8 | Time Series Plots of Scattering Coefficient for Cases C and D   | 39 |
| 2.9 | Time Series Plots of Scattering Coefficient for Cases C and D   | 41 |
| 3.1 | Source-specific primary particle size distribution . . . . .  | 57 |
| 3.2 | An example of the path of an air parcel arriving at Claremont.  | 70 |
| 3.3 | Emissions of the ARB particulate matter inventory and re-<br>vised inventory as a function of particle diameter and chemical<br>speciation. . . . . | 79 |
| 3.4 | Initial condition particle size distributions. . . . .  | 83 |
| 3.5 | Time series plots of observed and predicted gas-phase pollu-<br>tant concentrations on August 28, 1987 at Claremont, California                     | 88 |
| 3.6 | Time series plots of observed and predicted particle-phase con-<br>centrations on August 28, 1987 at Claremont, California . . .                    | 90 |

|      |  |     |
|------|--|-----|
| 3.7  | Time series plots of observed and predicted PM <sub>2.5</sub> SO <sub>4</sub> <sup>2-</sup> concentrations . . . . .   | 94  |
| 3.8  | Basecase model predictions of the mass distribution of individual chemical species compared to impactor measurements during the sampling period 0900-1300 PST on August 28, 1987, at Claremont, California. . . . .  | 96  |
| 3.9  | Basecase model predictions of the mass distribution of individual chemical species compared to impactor measurements during the sampling period 1700-2400 PST on August 28, 1987, at Claremont, California. . . . .  | 97  |
| 3.10 | Histograms of the frequency of occurrence of concentration residuals . . . . .   | 100 |
| 3.11 | The aerosol size distribution as measured by electrical aerosol analyzers and optical particle counters and the aerosol size distribution predicted by the basecase model calculations for air parcels arriving at Claremont at 6-hour intervals on August 28, 1987. . . . . | 103 |
| 3.12 | The size distribution of aerosol chemical composition as predicted by the basecase model at Claremont, California, on August 28, 1987 (0500 and 1100 PST). . . . .   | 105 |
| 3.13 | The size distribution of aerosol chemical composition as predicted by the basecase model at Claremont, California, on August 28, 1987, (1700 and 2300 PST). . . . .  | 106 |
| 3.14 | Model predictions and observations of particle light scattering coefficient and visual range. . . . .  | 108 |

|     |  |     |
|-----|--|-----|
| 4.1 | Actual photograph and synthetic images from photograph-based visibility model . . . . .  | 121 |
| 4.2 | Measured and modeled skylight radiance intensity . . . . .   | 128 |
| 4.3 | Measured and modeled chromaticity coordinates of sky . . . . .   | 132 |
| 4.4 | Frequency distribution of numerical densities for synthetic and actual images shown in Figure 4.1. . . . .                                     | 136 |
| 4.5 | Contour diagrams of difference between actual and synthetic photograph-based images . . . . .  | 137 |
| 4.6 | Numerical density differences between actual photographs and images from photograph-based visibility model as a function of distance . . . . . | 139 |
| 5.1 | Comparison of images from alternative visibility models . . . . .  | 147 |
| 5.2 | Frequency distribution of numerical densities for San Gabriel Mountains images shown in Figure 5.1. . . . .                                    | 155 |
| 5.3 | Frequency distribution of numerical densities for Downtown Pasadena images shown in Figure 4.1(d). . . . .                                     | 156 |
| 5.4 | Contour diagrams of difference between actual and synthetic images from satellite-based visibility model. . . . .                              | 158 |
| 5.5 | Numerical density differences between images as a function of distance between actual and satellite-based synthetic photographs . . . . .      | 159 |

# 1 Introduction

## 1.1 Motivation

Many urban and remote areas experience visibility degradation. Highly polluted areas such as Los Angeles suffer from visibility reduction, but lower pollutant levels also impair visibility at locations such as the Grand Canyon, which has scenic vistas stretching over large distances. Visibility degradation is caused by airborne particles and light-absorbing gases, and is one of the most widely publicized effects of air pollution.

Visibility standards have been set by some states, and there is federal legislation in the United States regarding visibility protection, particularly in national parks and wilderness areas (NRC, 1993). To understand how to reach such visibility goals or standards, one must be able to relate the emissions of air pollutants to the visual aspects of the resulting air pollution problem. To reach such an understanding, one must have knowledge of a series of processes: the level of emission of particulate air pollutants and gas-phase aerosol precursors, the transport and atmospheric chemical reactions that determine aerosol and gaseous pollutant ambient concentrations, the relationship between aerosol size distribution and chemical composition that determines the atmospheric light extinction coefficient, and the changes in the appearance of a scene that result from increased light scattering and absorption in the atmosphere.

The present understanding of the effect of pollutant emissions on visibil-

ity fails to provide a complete description of the processes outlined above in two important respects. First, present procedures for predicting atmospheric light scattering and absorption directly from source emissions are based on a rough approximation of the actual processes that occur in the atmosphere. Second, even if light scattering levels could be computed accurately from source emissions, the reported value of the atmospheric light extinction coefficient that results from such a calculation is a poor tool for communicating the effect of air pollution on the appearance of a scene.

Although it is well understood that aerosols and light absorbing gases cause visibility degradation, the majority of work to date, within the air pollution control community, has focused on relating ambient particle mass concentrations and bulk aerosol chemical properties to visibility degradation (Trijonis *et al.*, 1990; NRC, 1993), when in fact the size distribution of the aerosol and the chemical composition of the particles are extremely important to the visibility effects (Ouimette and Flagan, 1982; Larson *et al.*, 1988). To truly understand the relationship between pollutant emissions and visibility degradation, one must understand the relationship between particulate matter and gaseous pollutant emissions and the size distribution and chemical composition of the ambient particulate matter concentrations. A significant portion of ambient aerosol material is secondary in origin: it is material that is produced by gas phase atmospheric chemical reactions, then transported from the gas phase to the particle phase. The size distribution assumed by this newly formed particulate matter depends on the size distribution of the pre-existing aerosol onto which the secondary aerosol condenses, yet the primary emissions of particulate matter have not been characterized in great detail, chemically or by size distribution, in previous work. This problem

should be attacked directly by creating a mechanistic model for the effect of air pollutant emissions on visibility that deals directly with prediction of the size- and chemical-composition distribution of both primary and secondary aerosols.

The second difficulty identified above, that of clearly communicating the effect of light scattering and light absorption on the appearance of a scene, also must be tackled directly. The extent of visibility degradation is frequently expressed in terms of the atmospheric light extinction coefficient. This is a useful parameter, particularly because it can be used to estimate the visual range, but it does not provide much information about the actual appearance of the scene. Ideally, one would like to be able to produce information that describes the appearance of a scene under various levels of air pollution. A photograph of a scene provides such information on the visibility at near-field, mid-field and far-field points, rather than describing only the distance to extinction. If air quality modeling methods that seek to produce synthetic color photographs of the appearance of a scene in the presence of specified levels of air pollution could be perfected, then a means for easily communicating the effect of visibility model calculations would be in hand.

## **1.2 Research Objectives**

The objective of this thesis is to formulate and evaluate a number of alternative mathematical models that relate air pollution problems to the resulting effects on visibility, with an eye towards solving the technical and scientific problems identified above. The visibility modeling problem will be approached at three levels. First a model is sought that relates the measured

ambient particulate matter concentrations, chemical composition and size distribution, plus gaseous pollutant concentrations to the atmospheric light extinction coefficient and to the resulting distance at which large objects become indistinguishable from their surroundings as seen by a human observer (visual range). Next, a model is sought that will predict the airborne particle concentration, size distribution, and chemical composition (and gaseous pollutant concentrations) directly from source emissions such that visual range can be estimated directly from data on activities at the pollutant sources. Such a model is needed in order to examine the effect that proposed emissions control procedures would have on visibility. Completion of this work will also contribute to the understanding of the interaction of primary particle emissions from sources with secondary production of new particulate matter by atmospheric chemical reaction, and how that interaction shapes the atmospheric particle size distribution. Finally, models are sought that can create full-color photographs of the likely appearance of a scene in the presence of a specified level of air pollution. By linking the model for the effect of emissions on airborne particulate matter and gaseous pollutant properties to the synthetic photograph-based model for the effect of pollutant properties on the visual appearance of a scene, it should be possible in the future to communicate a great deal of information on the effect of proposed emission controls on visual air quality in advance of the adoption of such control programs.

### **1.3 Approach**

An overview of the remaining chapters will be provided in this section. In Chapter 2, a modeling effort is described in which the atmospheric light ex-

inction coefficient is predicted from the time series of the airborne particle chemical composition and size distribution measurements made during the 1987 Southern California Air Quality Study (SCAQS). This chapter seeks to test the consistency with which a regional air pollution problem can be related to a regional visibility problem based on atmospheric pollutant data that could be collected by a routine air monitoring network. The data collected during the SCAQS experiment would also be useful for the validation of integrated models that predict aerosol chemical composition and size distribution directly from emissions, a further objective of this study. Therefore, considerable effort will be expended to examine the quality of the SCAQS aerosol data base, in an effort to assess its potential as an air quality model validation data set for use in verifying emissions to air quality models that predict size-distributed chemically complex aerosol concentrations.

In Chapter 3, a mechanistic model for the prediction of visual range that is driven directly by data on source emissions and meteorological observations is formulated and exercised. The model assembled begins with data on particulate matter,  $\text{SO}_2$ ,  $\text{NO}_x$ , organic vapor, and ammonia emissions from sources and includes: (1) a description of the size distribution and chemical composition of particulate matter emissions from the major urban source types, (2) a description of the speciation of volatile organic vapor emissions from sources, (3) atmospheric transport and chemical reactions, (4) transport from the gas phase to the particle phase, (5) fog chemistry, plus (6) calculation of light scattering and absorption by the resultant ambient pollutant concentrations. Model predictions are tested against observations taken during the 1987 Southern California Air Quality Study (SCAQS).

Chapters 4 and 5 present two alternative image-processing based visibility

models. The improved image processing-based visibility model of Chapter 4 begins with a ground-based photograph of a clear day scene that is scanned through a microdensitometer and color separation filters in order to create an electronic image of the scene. The visibility model then employs light scattering and absorption calculations to recalculate the light intensity received at the location from which the picture was taken in the presence of a specified level of air pollution. Solution of the radiative transfer equation is used to compute sky color and skylight intensities at the location of the observer. The results of the model calculations are then used to create a synthetic color photograph of the predicted appearance of the scene in the presence of the smog event studied.

The image processing-based visibility model just described requires that clear day photographs be taken. In a location like Los Angeles, clear days are rare, and thus, clear day photographs are difficult to obtain. In Chapter 5, a model is developed that can create simulated images of the appearance of a scene under either clear sky or heavy smog conditions, based on synthetic terrain images created from Earth orbiting satellite data. These images are quite similar to actual ground-based photographs. This visibility model provides the possibility of world-wide application because the necessary satellite data are available globally.

## 2 Visibility Modeling Using Continuous Aerosol Size Distribution Monitors

### 2.1 Introduction

The severe visibility reduction that occurs in the Los Angeles area atmosphere is one of the most widely publicized effects of air pollution. On about 25 percent of the days of the summer months, visual range is reduced to less than 9 km at midday in Southern California communities such as San Bernardino and Upland, and to less than 11 km in Pasadena (Larson and Cass, 1989). Visibility phenomena can be connected to air pollutant properties, including aerosol chemical composition, relative humidity, and aerosol size distributions (Middleton, 1952). Empirical visibility models based on regression analysis that use aerosol chemical composition and relative humidity data as surrogates for aerosol size and solubility have been formulated and tested (White and Roberts, 1977; Cass, 1979; Groblicki *et al.*, 1981). Such models have shown that sulfate and nitrate aerosols are important determinants of local visibility reduction. Empirical models of this sort can be supported by aerosol composition data collected by routine air monitoring networks, as demonstrated by Cass (1979), Trijonis (1979; 1982ab), and Trijonis *et al.*

---

<sup>0</sup>Reference: Eldering A.; Cass, G. R.; Moon, K. C. An Air Monitoring Network using Size Distribution Monitors: Connecting Pollutant Properties to Visibility via Mie Scattering Calculations. *Atmos. Environ.*, Part A, in press.

(1990).

More recent studies (Ouimette and Flagan, 1982; Larson *et al.*, 1988; Larson and Cass, 1989) have shown that visibility models based directly on Mie theory calculations can be used to describe local visibility reduction phenomena. These models show that aerosol carbon species in addition to sulfates and nitrates play an important role in governing light scattering and absorption in the Southern California atmosphere. Such models based on Mie theory require both a complete chemical analysis of the aerosol samples taken over short periods of time (e.g., 4-hr averages or shorter) accompanied by detailed aerosol size distribution measurements. Such data are not at present available on a routine basis from governmental air monitoring networks.

Additional interest in acquiring size distributed aerosol data arises from the ongoing development of trajectory-based and grid-based aerosol processes air quality models. Such models seek to predict the size distribution and chemical composition of airborne particulate matter directly from data on primary pollutant emissions. Considerable progress has been made on the construction of algorithms for predicting sulfate formation during fogs (Pandis *et al.*, 1992b), nitrate formation (Russell and Cass, 1986; Russell *et al.*, 1988; Wexler and Seinfeld, 1992) and secondary organic aerosol formation (Pandis *et al.*, 1992a). Test calculations involving the evolution of the aerosol size distribution have been reported (Pilinis and Seinfeld, 1988). In the near future, integrated models that combine these features will become available. Those models must be tested against aerosol size distribution and chemical composition data from field experiments, yet such data bases are not widely available.

Two questions thus are posed, "Is it feasible to operate a routine air

monitoring network that supplies data sufficient to support the evaluation of air quality models that produce predictions of aerosol size distributions and chemical composition?" "Can such data also be used to support the characterization of regional visibility problems via visibility models based on Mie theory calculations?"

During the summer and fall of 1987, an air monitoring network designed in part to answer these questions was deployed in the Los Angeles area as part of the Southern California Air Quality Study (SCAQS). Filter-based sampling to determine aerosol mass concentration and chemical properties in two particle size ranges ( $d_p < 2.5 \mu\text{m}$ ;  $d_p < 10 \mu\text{m}$ ) was conducted over consecutive 4-hour time periods during 8 air pollution episodes covering 17 different days (see Table 2.1). Aerosol size distributions were measured continuously using electrical aerosol analyzers (EAA) and optical particle counters (OPC) at the Claremont, Long Beach, Rubidoux, and Central Los Angeles sites shown in Figure 2.1 on the dates shown in Table 2.1. Integrating nephelometers were used to measure the aerosol scattering coefficient at each site. This combination of aerosol size distribution data derived from automated operation of EAA's and OPC's plus filter based aerosol chemical data from which particle solubility and refractive index values can be estimated probably constitutes the least expensive combination of routine measurements that could be employed to meet the input data requirements of visibility models based on Mie theory calculations. In the present chapter, we describe the extent to which the time series of SCAQS air monitoring network data can be used to characterize airborne particle size distributions and chemical identity. Then we connect those data to the time series of atmospheric light scattering coefficient values via Mie theory calculations using the methods proposed by

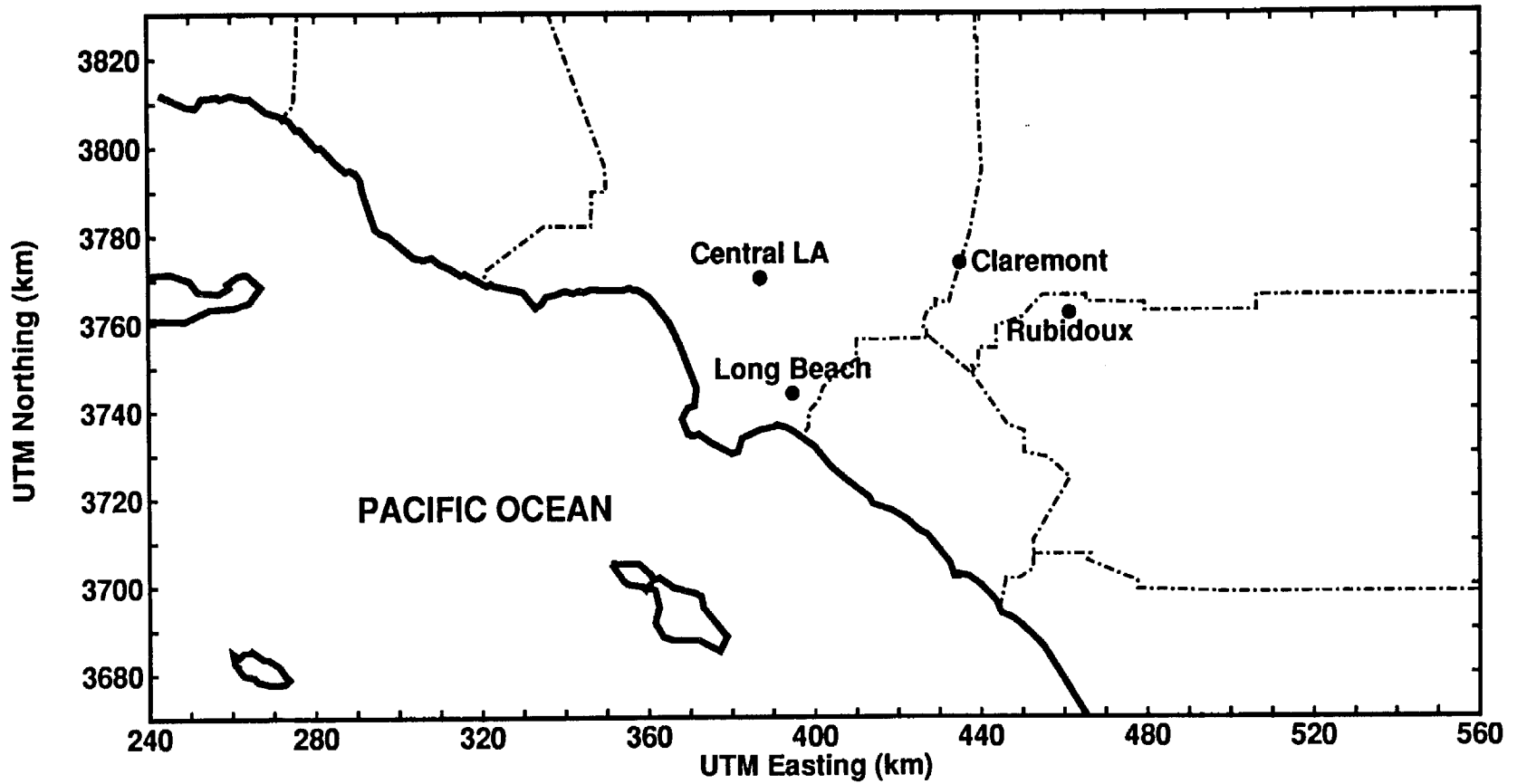


Figure 2.1: A map of Southern California showing the locations of the aerosol size distribution monitoring network operated during SCAQS.

Table 2.1: Sites and Dates of SCAQS Intensive Field Experiments

| Sites      | Location                  | sampling schedule   |                   |
|------------|---------------------------|---------------------|-------------------|
|            |                           | summer <sup>a</sup> | fall <sup>b</sup> |
| Claremont  | Claremont McKenna College | ✓                   |                   |
| Long Beach | Long Beach City College   | ✓                   | ✓                 |
| Rubidoux   | SCAQMD Monitoring Station | ✓                   |                   |
| Central LA | SCAQMD Monitoring Station |                     | ✓                 |

---

<sup>a</sup>1987 summer dates: June 19, June 24–25, July 13–15, August 27–29, September 02–03

<sup>b</sup>1987 fall dates: November 11–13, December 03, December 10–11

Larson and Cass (1989). Model predictions are compared to both nephelometer measurements of the atmospheric light scattering coefficient and to visual range values recorded by human observers.

## 2.2 Experimental Program

The overall design of the Southern California Air Quality Study experiments is described by Blumenthal *et al.* (1986) and Hering and Blumenthal (1989). Only those aerosol characterization experiments important to the present work will be recounted here. The SCAQS field program ran for nine weeks in the summer and four weeks in the fall of 1987. During these periods, several one to three day episodes were selected for intensive sampling. Aerosol size distribution measurements were made at the Claremont, Rubidoux, and Long Beach sites during the summer, and at the Long Beach and Central Los Angeles sites during the fall experiments. A number of documents are available that provide additional experimental details (Hering and Blumenthal, 1989; Hering, 1990).

### 2.2.1 Aerosol Size Distributions

Aerosol size distributions were measured at each site using an electrical aerosol analyzer (EAA, TSI Model 3030) for particles from 0.007  $\mu\text{m}$  to 0.42  $\mu\text{m}$  in diameter; a Particle Measuring Systems LAS-X active scattering laser optical counter (PMS OPC) for particles 0.095 to 2.83  $\mu\text{m}$  in diameter, and a Climet 208 white light optical particle counter (Climet OPC) for particles in the diameter range from 0.72 to 9  $\mu\text{m}$ . Data were acquired over consecutive four-minute averaging times, and then averaged to one hour periods.

### 2.2.2 Aerosol Chemical Composition Measurements

Aerosol mass concentrations and chemical composition were measured using the SCAQS sampler developed for this study by Fitz *et al.* (1989) (see Figure 2.2). Aerosol samples were taken in two particle size fractions, corresponding to aerodynamic particle diameters of less than  $2.5 \mu\text{m}$  (PM<sub>2.5</sub>) and less than  $10 \mu\text{m}$  (PM<sub>10</sub>). Fine particle (PM<sub>2.5</sub>) and PM<sub>10</sub> samples were collected on 47mm diameter Teflon filters that were then analyzed to determine aerosol mass, trace element, and ionic species concentrations. Gravimetric techniques were used to determine the aerosol mass concentrations. Ion chromatography was used for the analysis of  $\text{NO}_3^-$ ,  $\text{SO}_4^{2-}$ , and  $\text{Cl}^-$ . Ammonium ion concentrations were determined by colorimetry. Atomic absorption spectrophotometry was used to measure PM<sub>10</sub> sodium concentrations. Samples collected on 47mm diameter pre-fired quartz fiber filters were analyzed for organic carbon (OC) and elemental carbon (EC) concentrations by the dual temperature zone furnace oxidation method (Chan and Durkee, 1989). Trace element concentrations were measured by X-ray fluorescence (XRF), and were corrected for deposit non-uniformity on the filters according to the recommendations of Matsumura and Cahill (1991). A 47mm diameter Nuclepore filter was used for particle light absorption ( $b_{abs}$ ) determinations by the integrating plate method (Lin *et al.*, 1973).

The SCAQS sampler was used to collect five samples per day on intensive study days, with sampling periods of four hours (daytime) and five to seven hours (nighttime) duration. Samples were changed at 2400, 0500, 0900, 1300, and 1700 hours PST in the summer, and at 2400, 0600, 1000, 1400, and 1800 hours PST in the fall. These sampling durations are the longest of the measurements needed in the present visibility modeling study, and thus other

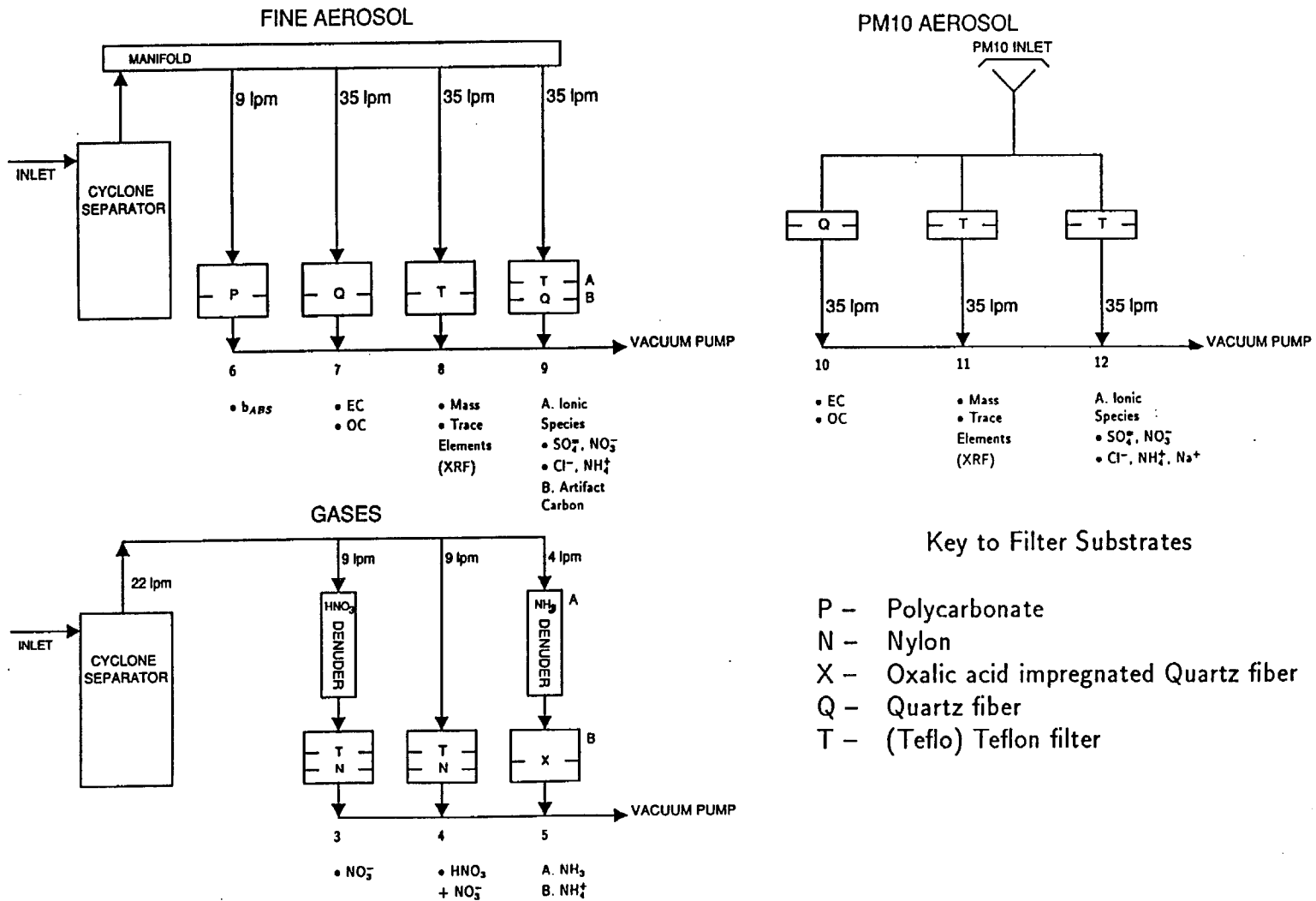


Figure 2.2 – SCAQS sampler used for filter-based measurements of PM<sub>2.5</sub> and PM<sub>10</sub> aerosol mass concentrations and chemical composition; chemical analyses performed on each sample are indicated below each branch of the sampling system.

data will be averaged to match these sampling periods.

An effort was made to correct for the possible volatilization of aerosol nitrate and ammonium ion collected on Teflon filters (Appel *et al.*, 1980; Solomon *et al.*, 1988). Along with the Teflon filter samples collected and analyzed for inorganic ions, measurements were made of fine particle nitrate and vapor phase  $\text{HNO}_3$  by the denuder difference method (see Hering *et al.*, 1988; Solomon *et al.*, 1988). The difference between the fine particle nitrate collected following the  $\text{HNO}_3$  denuder and that measured on the fine particle Teflon filter (branch 9 of Figure 2.2) was taken as an indication of the amount of  $\text{NH}_4\text{NO}_3$  volatilized from the Teflon filter. The nitrate concentration correction determined in this manner was added to both the fine particle and PM10 nitrate concentrations as measured on the Teflon filters in sample lines 9 and 12 of Figure 2.2 along with stoichiometrically equivalent amounts of ammonium ion. The total filter masses were adjusted upwards by the sum of the nitrate and equivalent ammonium ion concentration corrections.

### 2.2.3 Light Scattering Coefficient Data

Measurements of light scattering coefficient values were made at all of the sites shown in Figure 2.1. Particle light scattering coefficient values were measured using SCAQS network (SC) nephelometers by Aerovironment, Inc. or by the South Coast Air Quality Management District (SCAQMD). Meteorology Research, Inc. (MRI) 1560's series nephelometers with heated inlets were used by those two organizations at all sites except Rubidoux. These instruments were spanned and zeroed nominally every three days and were calibrated to read zero when observing only Rayleigh scattering by air molecules, thereby measuring only the scattering of light due to particles. These instru-

ments are most sensitive at a wavelength of 525 nm (Ruby and Waggoner, 1981). Scientists from the University of Illinois (UI) (Claremont and Rubidoux, summer) and General Motors Research Laboratories (GM) (Claremont in summer and Long Beach in fall) also collected light scattering data using slightly different instrumentation. The instrumentation used by GM was an MRI 1550 nephelometer with heated inlet, which is most sensitive at a wavelength of 475 nm (Ruby and Waggoner, 1981). That instrument was renovated with a new light source before this experiment and was spanned and zeroed frequently during the SCAQS experiment. GM data were corrected for zero and span drift before the data were reported. The UI data were collected from two temperature programmed nephelometers (Rood *et al.*, 1987). The UI nephelometer data used here are from a system situated outdoors in the shade at ambient temperature and that was recalibrated every three days. That nephelometer is geometrically similar to MRI 1550 nephelometers, but the optics were similar to an MRI 1560 nephelometer which is most sensitive at a wavelength of 525 nm.

Duplicate light scattering data sets were available from independent investigators for the summer period at Claremont (SC, UI, and GM) and for the fall period at Long Beach (SC and GM) as shown in Figure 2.3. The similarities and differences between the measurements are interesting. The SC and UI measurements were made at the same wavelength, but the SC nephelometer had an inlet that was heated continuously, whereas the UI data used here were taken under ambient temperature conditions. A comparison of these data show that the scattering coefficient values reported by SC were consistently smaller than those reported by UI. The heated inlet would be expected to be responsible for some of this result, as the objective of a heated

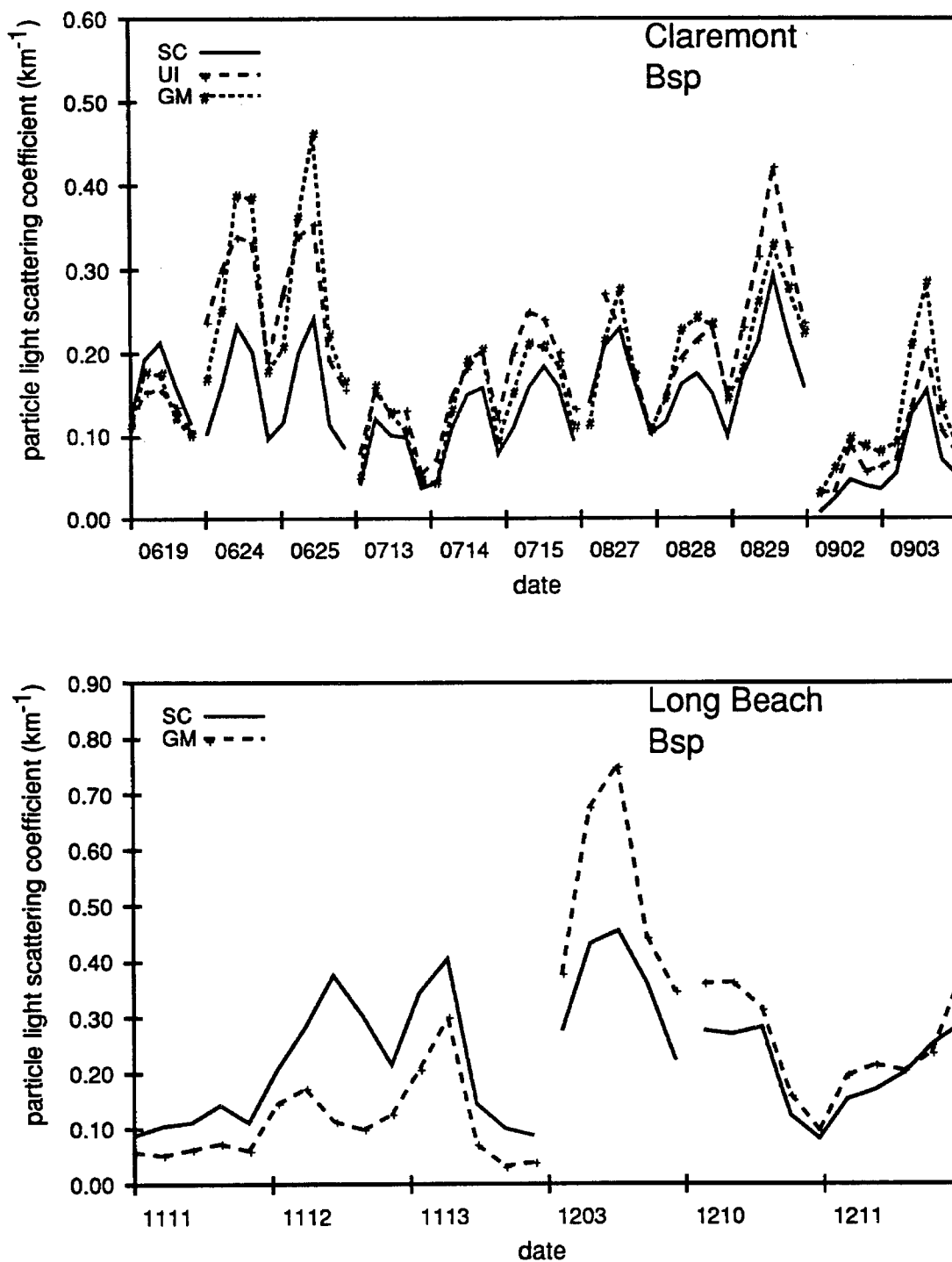


Figure 2.3: Concurrent measurements of light scattering by particles made by different investigators during SCAQS. Dates are given as month, date (i.e., 0619 is June 19, 1987).

nephelometer is to measure the light scattering by dry particles (i.e., following removal of aerosol water). The instrument used by SC is most sensitive at 525 nm, and the instrument used by GM is most sensitive at 475 nm. Light scattering by atmospheric particles is wavelength dependent, with the light scattering greater at 475 nm than at 525 nm (Middleton, 1952). A comparison of the GM and SC data at Claremont shows that this expected ordering of the data is reflected in the data base most of the time. The scattering coefficient values measured by GM are almost always larger than the values reported by SC, frequently by more than the factor of about 1.1 that would be expected for measurements made at 475 and 525 nm. As noted earlier, the frequency with which the instruments at Claremont were spanned and zeroed varies between investigators. It is logical to believe that zero drift over the course of time could explain the nearly identical readings of these instruments at the start of the experiments followed by a high correlation but separation of their output data streams over time.

At Long Beach, half of the scattering coefficient values reported from SC nephelometers are larger than those reported simultaneously by GM, and vice versa. These differences seen in simultaneous measurements of the scattering coefficient suggest that not all of the nephelometer measurements at Long Beach can be correct, and that no visibility model can be expected to produce exact agreement with all measured light scattering values at Long Beach in this case because the light scattering data are in conflict to some degree. While the author of the present chapter did not make any of the nephelometer measurements in question, it is possible to inquire into the possible causes for the observed differences between instruments. Further investigation of the nephelometers used at Long Beach was conducted by

contacting the owners of those instruments and asking for any information that would be relevant to resolving these discrepancies. It was learned that the SC nephelometer used at Long Beach during the summer period only has since been disassembled for renovation and was found to have an optical filter missing. The SC nephelometer used at Central Los Angeles during the fall time period was later serviced and was found to produce light scattering readings that were lower than actual. Therefore, the SC nephelometer data at Long Beach in the summer and at Central Los Angeles in the fall should be viewed as being of doubtful accuracy.

Nephelometers in theory have a response that is directly proportional to the atmospheric scattering coefficient. There are two effects that distort this: The design of the nephelometer inlet can cause particle losses for large particles, and therefore not accurately measure coarse particle scattering. There is also concern that the geometry of the nephelometer causes light scattered near 0 and 180 degrees to escape detection in the instrument (Sloane *et al.*, 1991; Hasan and Lewis, 1983). Investigations into this truncation error have shown that for aerosol size distributions like the ones measured in this experiment, with a geometric mean diameter on the order of 1 micron, the truncation factor is around 5 to 10 percent. Due to the coarse particle losses and small truncation error, model predictions of the light scattering coefficient derived directly from aerosol size distribution data via Mie theory calculations are expected to somewhat exceed the values measured by typical nephelometers.

### 2.2.4 Data Base Preparation

Data missing from the SCAQS data base were replaced by closely related measurements where possible. Relative humidity data at the Long Beach SCAQS monitoring site were missing from the SCAQS data set for the summer dates. Relative humidity data collected by the Federal Aviation Administration (FAA) at Dougherty Field in Long Beach were substituted. This air field is located 1.7 km southwest of the Long Beach SCAQS air monitoring site. Certain Claremont PM10  $\text{NH}_4^+$  data that were missing were replaced by estimates obtained from the available fine particle  $\text{NH}_4^+$  data. Regression of the reported PM10  $\text{NH}_4^+$  data on PM2.5  $\text{NH}_4^+$  data at Claremont first was performed to assess the typical relationship between these two parameters. The missing PM10  $\text{NH}_4^+$  values then were estimated from the available PM2.5  $\text{NH}_4^+$  data using the resulting regression equation. This is not expected to lead to significant error since the overwhelming majority of the  $\text{NH}_4^+$  was found in fine particles during SCAQS. (The dates and sampling periods where such replacement occurred were August 27, sampling period 5, August 28, all sampling periods, and August 29, sampling periods 1-4.) Ammonium ion data also were estimated by regression analysis for six data points in the Long Beach data set. In four cases, missing data on coarse particle  $\text{Na}^+$  concentrations were estimated by completing an ion balance on the PM10 samples. This is not expected to lead to appreciable error because, as will be shown later, light scattering by large particles between 2.5 and 10  $\mu\text{m}$  diameter makes only a small contribution to the calculated light scattering coefficient values. In an effort to maximize the days available for modeling, all data that had been marked invalid were examined closely. At the end of the data base preparation step, only 18 of 225 possible time periods did not

contain a set of data on aerosol size distribution, aerosol chemical composition, temperature, and relative humidity sufficient to support light scattering calculations.

### **2.3 Correction of Aerosol Size Distribution Data Collected by the PMS Optical Particle Counters**

Experiments were performed in July of 1987 by Hering and McMurry (1991) to determine the response of a single optical particle counter to monodisperse fractions of Los Angeles area ambient aerosols. Measurements were made at Claremont to calibrate an instrument optically identical to the PMS laser OPC's used in the SCAQS study. The ambient aerosols were found to scatter less light than the polystyrene latex spheres (PSL) that are used for the factory calibration of these instruments, but about the same amount of light as oleic acid, which has a lower refractive index. Because of this difference in response between atmospheric aerosols and polystyrene latex spheres, these instruments, if used in accordance with the manufacturer's calibration report, will produce an incorrect indication of the atmospheric particle size distribution. Therefore, in the present study, the particle diameters reported from the PMS OPC's are corrected according to the results of Hering and McMurry in order to recover the actual size distribution of the atmospheric aerosol.

### **2.4 Creating a Combined Size Distribution for Use in Further Calculations**

Aerosol size distributions were created by merging the data from several instruments. The PMS laser OPC nominally reports particle counts over the

diameter range from  $0.095 \mu\text{m}$  to  $2.83 \mu\text{m}$ . However, the experiments of Hering and McMurry (1991) provide correction factors for converting the manufacturer's PSL equivalent particle diameters to Los Angeles ambient aerosol equivalent diameters only over the range of sizes larger than  $0.2 \mu\text{m}$  in diameter. Therefore, the smallest particles counted by the PMS OPC's are less well characterized than those at the larger end of that instrument's range of operation. Conversely, the EAA is most reliable at small particle diameters. Consequently, the EAA data were used to describe the aerosol size distribution over the range from  $0.007$  to  $0.23 \mu\text{m}$  particle diameter while the PMS OPC data were used to describe particles  $0.23 \mu\text{m}$  to  $2.83 \mu\text{m}$  in diameter. While the Climet OPC's nominally measure particles up to  $9 \mu\text{m}$  in diameter, these instruments were frequently found to record very low number counts in the range from  $2$  to  $9 \mu\text{m}$  particle diameter. Particle mass and volume concentrations in the  $2.5$  to  $10 \mu\text{m}$  size range obtained from the difference between PM<sub>2.5</sub> and PM<sub>10</sub> filter samples were computed and compared to the Climet data over the same size range. It was found that the Climet instruments significantly underestimated the volume (hence mass) of particles in that size range. As a result of this finding, the particle size distribution in the diameter range from  $2.5$  to  $10 \mu\text{m}$  was estimated using a constant value of  $dV/d\log d_p$  over that diameter range with a total aerosol volume concentration equal to that inferred from the filter data. These relatively large particles are not particularly efficient scatterers of light. It will be shown later that this approximation is suitably accurate for the purposes of the present study. Examples of aerosol size distributions developed in this manner are shown in Figure 2.4. The appearance of two modes in the sub-micron portion of the size distribution shown in Figure 2.4 is characteristic of

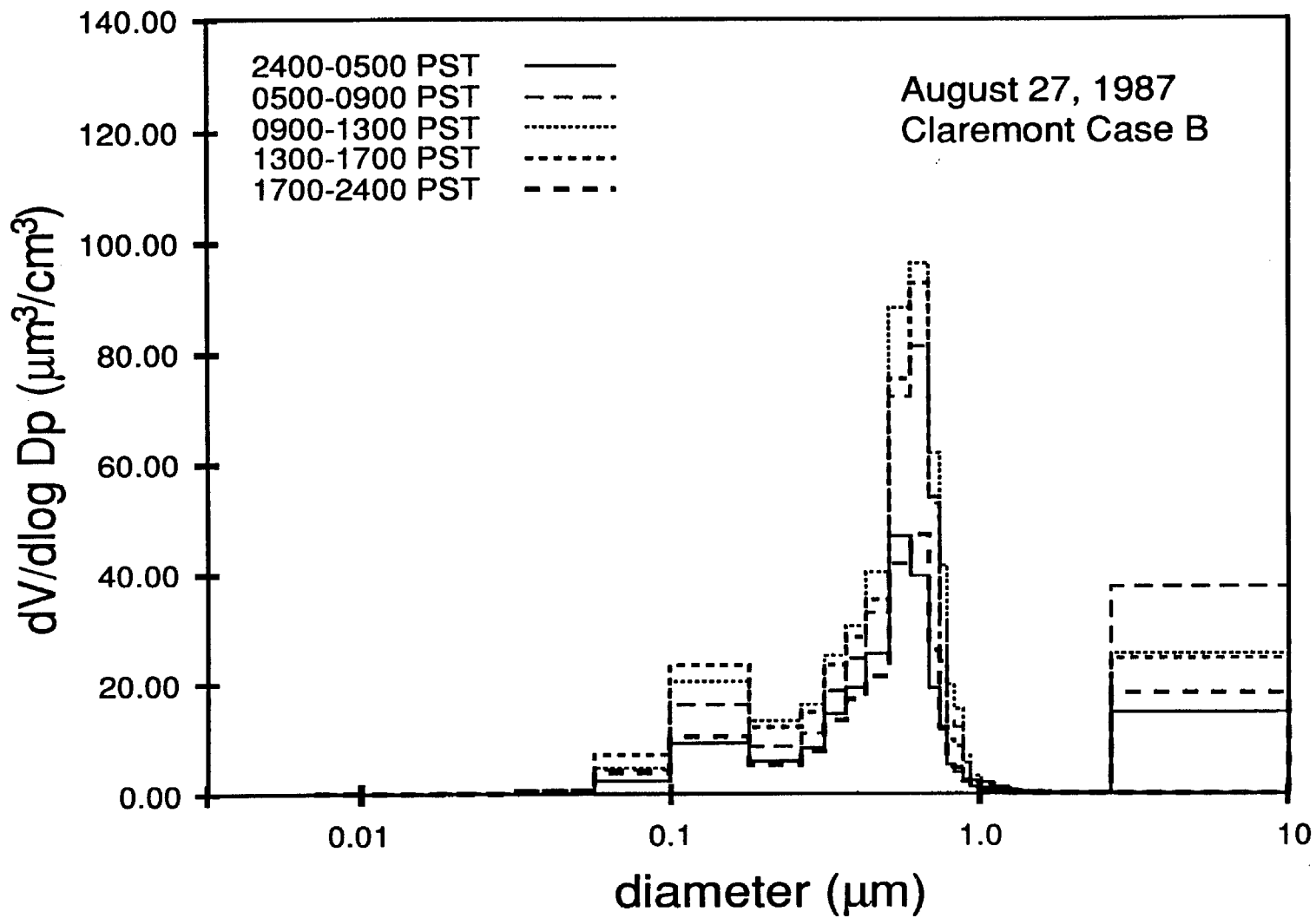


Figure 2.4: An example of the final aerosol size distribution created for use in visibility modeling.

the SCAQS continuous monitoring data set and is also seen in the impactor measurements reported by John *et al.* (1990).

## 2.5 Internal Consistency of the Aerosol Chemistry Data Base

A series of consistency checks were performed on the aerosol chemistry data sets to confirm the quality and usefulness of the data base. Ion balances first were constructed for the water soluble components of each complete aerosol sample. An example is shown in Figure 2.5a. The anion versus cation balances on each sample at all sites are in good order, indicating that the data on these important water soluble species are internally consistent. The average ratio of PM10 cations to anions at Claremont, Downtown Los Angeles, Long Beach in the summer and fall, and Rubidoux was 0.94, 0.84, 0.99, 0.87, and 0.83, respectively.

Next, a material balance was constructed for each aerosol sample in which the sum of the mass concentrations of all chemically identified aerosol species was compared against the gravimetrically measured mass concentration. The procedure used was similar to that of Stelson and Seinfeld (1981), Gray *et al.* (1986), and Larson *et al.* (1988). For each aerosol sampling period at each monitoring site, the measured trace metals were converted to their common oxides. Organic carbon was multiplied by a factor of 1.4 in order to estimate the mass of organic compounds present. Ionic species concentrations were converted to equivalent ionic compound concentrations by associating anions with cations in the following order:  $NaCl$ ,  $(NH_4)_2SO_4$ ,  $NH_4NO_3$ ,  $NaNO_3$ ,  $NH_4HSO_4$ , and  $H_2SO_4$  until all ionic species are consumed. Then the estimated trace metals oxides, organic compounds, elemental carbon, and

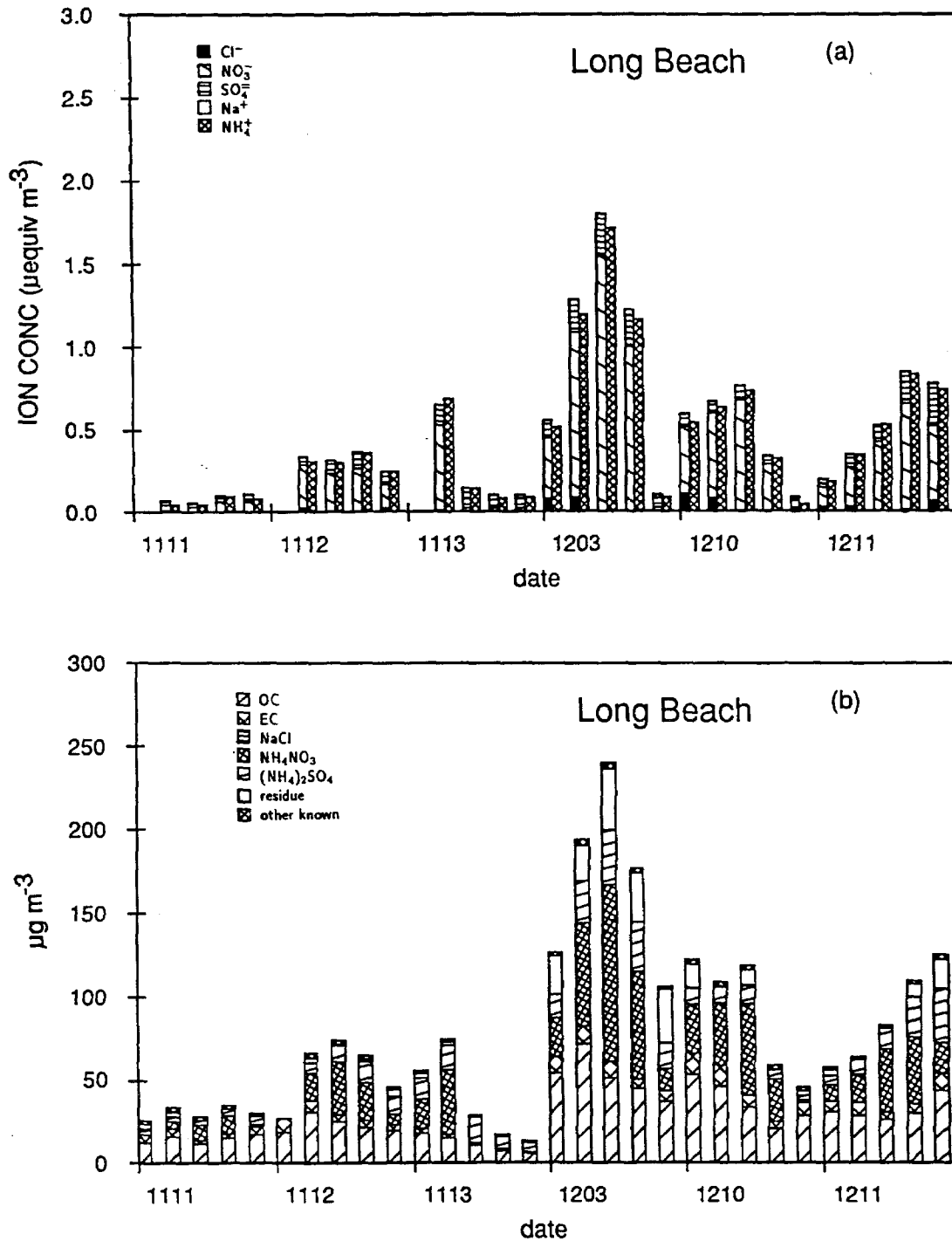


Figure 2.5: An example of the ion balances (above) and material balances (below) constructed for PM<sub>2.5</sub> aerosols. The residue appearing in the lower figure represents the differences between the gravimetrically determined mass concentration and the sum of the chemical components.

ionic species concentration values were summed. The total mass of identified chemical species was then compared to the gravimetrically determined filter mass (referred to as measured mass) as shown in the example given in Figure 2.5b. The average ratio of the sum of the identified individual chemical species to the measured  $PM_{2.5}$  filter mass for the summer data at Claremont, Long Beach, and Rubidoux was 0.84, 0.80, and 0.82, respectively, with very few cases of overprediction. For the fall, at Central Los Angeles and Long Beach, the ratio of chemically identified to gravimetrically identified  $PM_{2.5}$  filter mass was 0.75 and 0.95 respectively. Some of the unidentified mass remaining is thought to be liquid water retained in the filter samples despite desiccation.

## **2.6 Examination of the Aerosol Liquid Water Content**

The gravimetric mass determinations made from filter samples were nominally measured at  $45 \pm 5\%$  relative humidity. At such low relative humidity much of the water present in the aerosol under atmospheric conditions has been removed prior to weighing. The heated nephelometers likewise were expected to remove water from the ambient aerosol, while the effect of the OPC's on aerosol water retention initially was unclear. Therefore, a series of analyses were undertaken to assess the effect of water retention on each data set.

Comparisons of aerosol volume seen by the size distribution measurement instruments to aerosol volume inferred from the filter data show excellent agreement in most cases. Regression of  $PM_{2.5}$  volume from the size distribution instrumentation on  $PM_{2.5}$  volume inferred from the filter samples

yields correlation coefficients for the summer periods at Claremont, Long Beach and Rubidoux of 0.93, 0.70, and 0.86, respectively. The correlation coefficients for this regression for the fall sites at Downtown Los Angeles and Long Beach are 0.97 and 0.98, respectively. There is no bias that is related to relative humidity, nor any temporal patterns of difference (e.g., day/night systematic differences). At all sites, regression of the ratio of aerosol volume measured from the size distribution data to aerosol volume inferred from the filter data on relative humidity yields regression coefficients for the slope that are zero, within the 95% confidence limits. If there was water in the aerosol when the scattering coefficient was measured by the nephelometers, but not when the fine particle mass was measured on the filters, then the ratio of reported fine particle mass concentration to  $b_{scat}$  would change as a function of the relative humidity. The relationship between the fine particle mass concentration measured at 45% relative humidity and the measured scattering coefficient was examined graphically and does not show any temporal variations that suggest systematic differences in water content as a function of the time of day.

Next, a technique was selected to estimate the amount of water present in the original aerosol as it existed while suspended in the free atmosphere. The method used is adapted from Sloane (1984b). Using this method, the concentration of soluble aerosol mass is calculated from the chemical composition of the filter samples. The van't Hoff equation is then applied to calculate the water present. The aerosol volume inferred from the filter samples was regressed on the aerosol volume inferred from the aerosol size distribution instruments both without addition of aerosol water and with addition of aerosol water. The case with addition of aerosol water refers to the addition of the

amount of water thought to be present originally under ambient conditions. The correlation coefficient for the regression of the filter-based aerosol volume data on the size distribution instrument-based aerosol volume data was consistently higher for the case without water addition to the filter samples than for the case with water addition to the filter samples.

The above tests suggest that the light scattering coefficient measurements made using heated inlet nephelometers, the particle size distribution measurements obtained from the optical particle counters, and the gravimetric filter measurements made after desiccation were all conducted on aerosols that were in similar states of water retention. In short, all of the sampling procedures used apparently dried out the aerosol before measurements were made. Therefore, visibility model verification tests reported here first will compare predicted and measured aerosol scattering at low relative humidity conditions. Then in a second stage of the investigation, an estimate will be made of the amount of light scattering that would occur at the ambient relative humidities that prevailed at the time of sample collection.

## **2.7 Estimation of Refractive Index**

Two candidate methods for estimating the refractive index of the aerosol were examined. The availability of bulk chemical composition information for PM<sub>2.5</sub> and PM<sub>10</sub> samples rather than data on single particle chemical composition forces the assumption that the aerosol is internally mixed, at least in each size group. The first method tested is based on the work of Stelson (1990). In this method the refractive index for the aerosol is estimated from the partial molar refractions of the individual chemical species that make up the aerosol. In the second method, a volume-averaged refractive index

is computed. The aerosol chemical composition data described earlier as having been constructed during the aerosol mass balance analysis were used in conjunction with density and refractive index information (Weast, 1985; Sloane, 1984b) to compute refractive index values for the aerosol that are the weighted sum of the refractive indexes of the individual species. The weighting factors are the volume fraction contributed by each chemical substance. Aerosol light absorption depends on the complex part of the refractive index which in these calculations is determined by the elemental carbon content of the aerosol; pure elemental carbon (black carbon) is assumed to have a refractive index of  $1.9 + 0.6i$  (Sloane, 1984b).

It was found that when using either refractive indices based on partial molar refractions or volume-averaged refractive indices, the differences in the present cases are so small that the two methods produce nearly indistinguishable light scattering results, given the same aerosol size distributions within a Mie scattering calculation.

The effect on light scattering calculations of the assumption that the aerosol is internally mixed in a chemical sense is harder to judge, but some evidence exists. Both the work of Ligocki *et al.* (1990) and Zhang *et al.* (1993) show that Los Angeles area atmospheric particulate matter displays many characteristics of an external mixture with different particles having differing chemical composition. However, both Larson *et al.* (1989) and Zhang (1990) have shown that there is little difference in the extinction coefficient calculated for Los Angeles ambient aerosols using external versus internal mixture models.

## 2.8 Calculation of the Extinction Coefficient

The atmospheric light extinction coefficient can be expressed as the sum of four contributions.

$$b_{ext} = b_{sp} + b_{ap} + b_{sg} + b_{ag} \quad (2.1)$$

The extinction coefficient is the sum of the components due to light scattering by particles,  $b_{sp}$ , light absorption by particles,  $b_{ap}$ , scattering of light by gases,  $b_{sg}$ , also known as Rayleigh scattering when the gas is air, and light absorption by gases  $b_{ag}$ . Light scattering and absorption by particles is calculated from Mie theory (Sloane, 1984a). The refractive index values and aerosol size distribution are required to perform the Mie scattering calculation. The scattering and absorption efficiencies are calculated for each diameter interval of the aerosol particle size distribution. Then  $b_{sp}$  and  $b_{ap}$  are calculated by integrating the product of the scattering and absorption efficiency factors for particles of each size and the number of such particles per unit air volume over the diameter range represented by the aerosol size distribution. Light absorption by  $\text{NO}_2$  gas is calculated according to the wavelength dependent absorption coefficients reported by Hodkinson (1966). Scattering by gases is calculated as Rayleigh scattering, with  $b_{sg} = 1.5 * 10^{-5} m^{-1}$  at a wavelength of 550 nm, and  $b_{sg}$  varying with wavelength as  $\lambda^{-4}$  (Penndorf, 1957). These calculation procedures are described in detail by Larson *et al.* (1988).

## 2.9 Visibility Model Results

Data on the aerosol size distribution and refractive index corresponding to each short term sampling period were supplied to a Mie scattering code using procedures similar to those of Larson *et al.* (1988) and Larson and

Cass (1989). The particle light scattering coefficient,  $b_{sp}$  of equation 2.1, was calculated as a function of wavelength. These results then were compared to values of the particle light scattering coefficient as determined experimentally by the integrating nephelometers.

Three sets of calculations are presented here that will be referred to as cases A, B, and C, as listed in Table 2.2. These represent a progression from a model based on the instrumental dry fine particle size distribution and chemical composition data alone (A), to one in which light scattering by dry particles in the diameter range of 2.5 to 10  $\mu\text{m}$  is added to the scattering by dry fine particles (B), to one where the dry fine particle size distribution is corrected to match the aerosol volume inferred from the fine particle filter samples (C). In these calculations, the refractive index of the dry aerosol will be estimated using the volume-average of the refractive indices of the individual chemical components of the aerosol as described earlier. In each case, calculated scattering by dry particles can be compared to nephelometer measurements of scattering by dry particles at the wavelength of maximum sensitivity of each particular nephelometer.

Results of the model calculations for light scattering by dry fine particles (case A) are shown in time series in Figure 2.6. The summer data sets at Claremont, Rubidoux and Long Beach appear in a pair of side-by-side graphs for each site, while the shorter fall data sets at Long Beach and Central Los Angeles are at the bottom of the figure. Figure 2.6 shows that light scattering by particles at Claremont as measured by GM is explained quite well based on light scattering by a dry aerosol. Both the magnitude and the temporal trends of the measured light scattering coefficient values are reproduced. In the summer period at Long Beach, the model calculations explain light

Table 2.2: Methods Used to Assign Size Distributions

| Case | Size Distribution Description  |
|------|--|
| A    | dry fine aerosol size distribution;<br>EAA 0.007 to 0.23 $\mu\text{m}$ , PMS OPC 0.23 to 2.83 $\mu\text{m}$ diameter   |
| B    | dry aerosol size distribution extended to 10 $\mu\text{m}$ diameter;<br>Case A with constant size distribution from 2.5 to 10 $\mu\text{m}$ diameter   |
| C    | extended dry aerosol size distribution corrected to match filter data;<br>Case B with fine particle size distribution scaled to match<br>aerosol volume determined from PM2.5 filter samples |
| D    | wetted aerosol;<br>Case C with water added to coarse and fine aerosol according to Sloane's method;<br>size distribution scaled up to match computed wet aerosol volume                      |

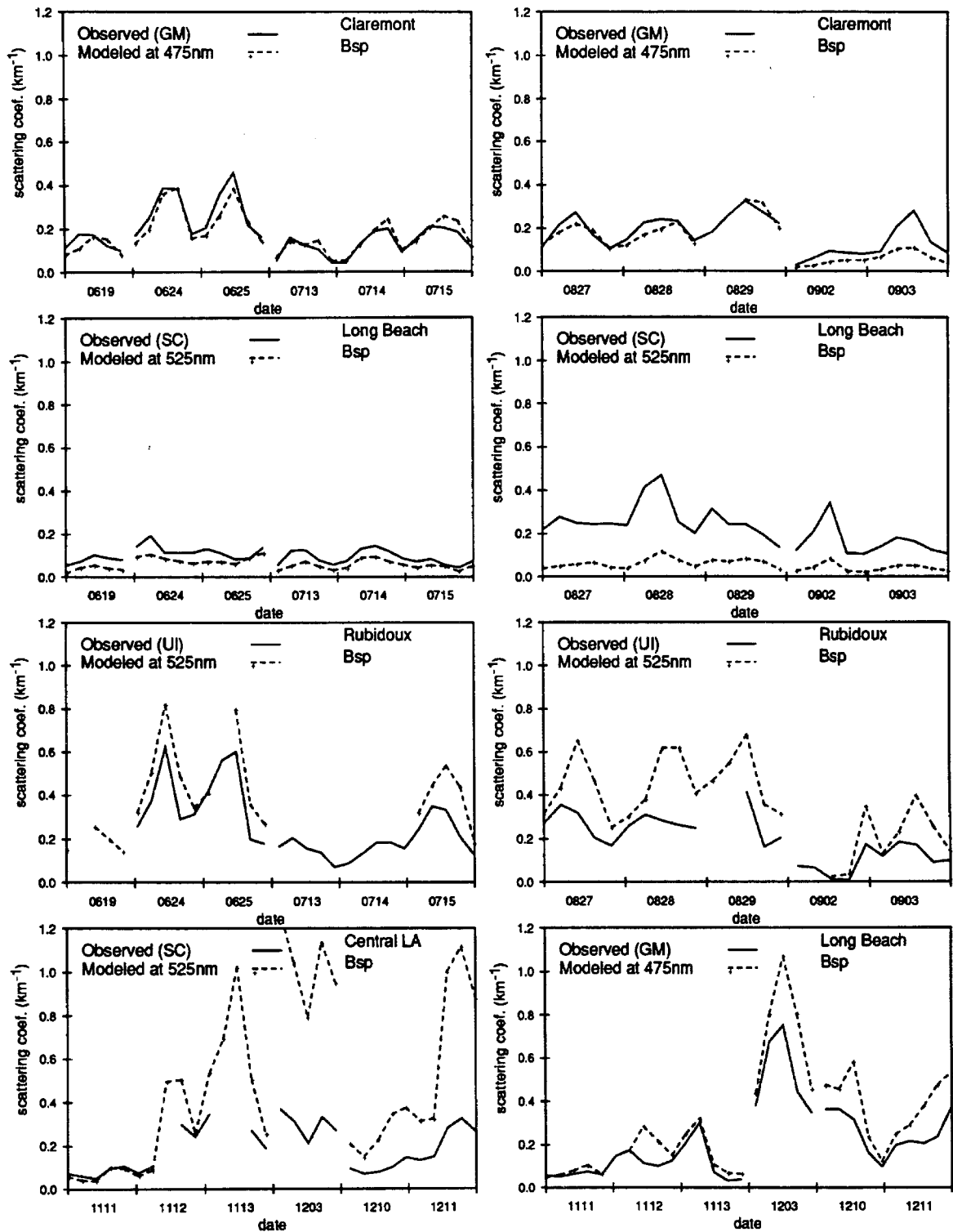


Figure 2.6: Comparison of calculated light scattering by dry fine particles to nephelometer measurements of the particle light scattering coefficient (Case A).

scattering levels fairly well during June and July but underpredict the light scattering coefficient in August and September. The GM data at Long Beach are modeled well in the fall period.

The effect of inclusion of particles in the 2.5  $\mu\text{m}$  to 10  $\mu\text{m}$  size range (Case B) does not noticeably affect the calculated particle light scattering coefficient values. Hence, the model will not be particularly sensitive to the approximate size distribution used for particles in this larger size range.

Time series plots in Figure 2.7 show the results of scaling the aerosol size distribution so that the dry aerosol volume matches that inferred from the filter samples (Case C). Predictions and observations are still in close agreement at Claremont at all times and at Long Beach in June, July, November, and December. Agreement at Central Los Angeles is improved. The correlation coefficient at Rubidoux is not higher for this case, but all of the large overpredictions are reduced in this case.

Particle light scattering coefficient values at each site predicted from the model for Cases A, B, and C were compared with all of the available nephelometer data. The results are shown in Table 2.3. Results at Claremont show little bias between predictions and observations and small variance in the residual difference between predictions and observations. Model results at Claremont are highly correlated with the observations. Poorer agreement between measurements and model results occurs primarily in those cases (Central LA fall and Long Beach summer) where a single nephelometer is present that was subsequently found to have experienced maintenance problems and where there is no possibility of comparison against a second instrument.

Next, water addition to the aerosol was simulated (approximately) in

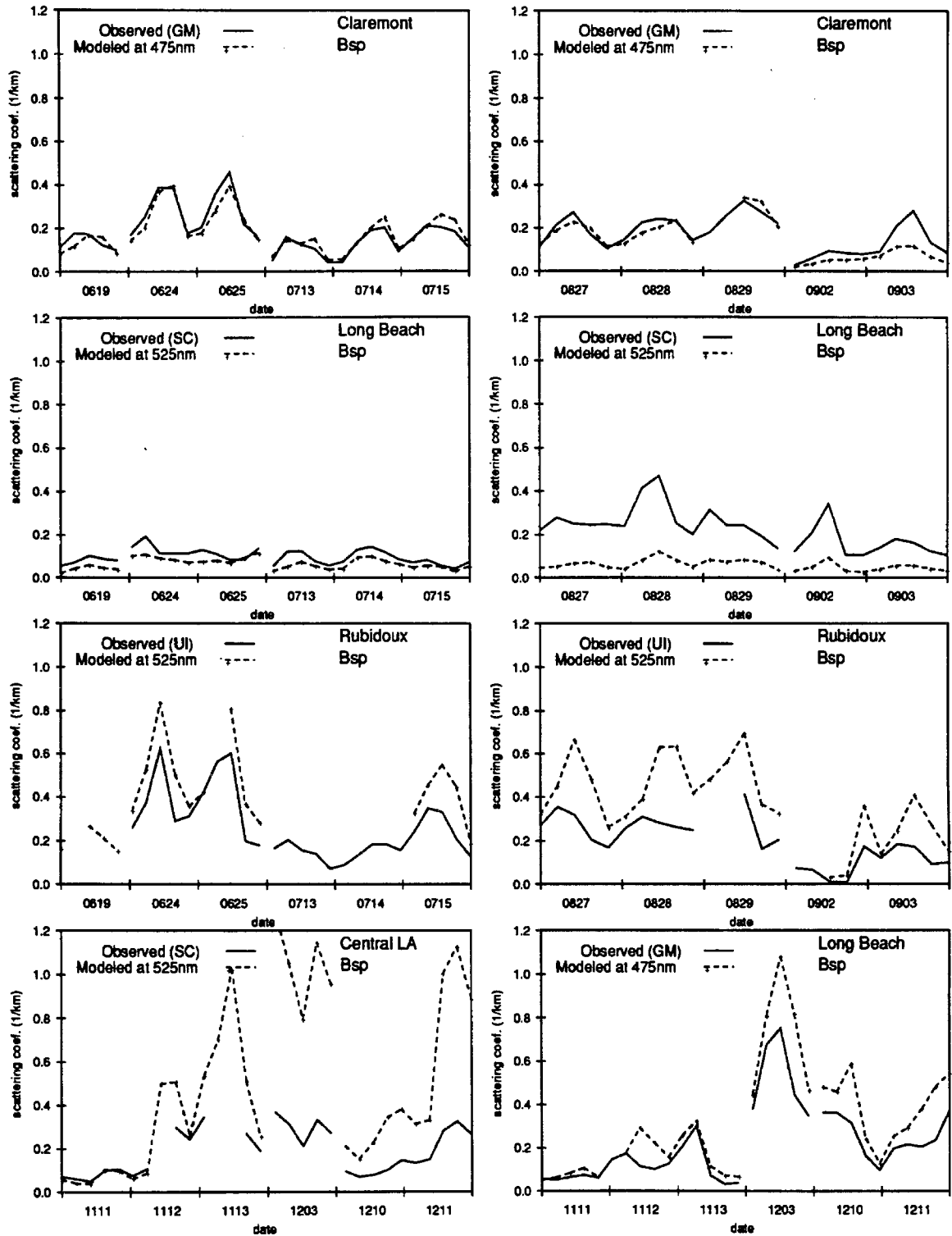


Figure 2.7: Comparison of calculated light scattering by particles to nephelometer measurements of the particle light scattering coefficient after having corrected the aerosol volume distributions to match the aerosol volume inferred from simultaneous filter samples (Case C).

Table 2.3: Comparison of Modeled Light Scattering Coefficient Values to Nephelometer Measurements of the Light Scattering Coefficient (all data)

| Site and<br>Nephelometer <sup>(a)</sup> | Case <sup>(b)</sup> | bias<br>( $\text{km}^{-1}$ ) <sup>(c)</sup> | variance<br>of residuals | n  | correlation<br>coefficient <sup>(d)</sup><br>(r) |
|---|---------------------|---|--------------------------|----|--|
| <i>summer</i>                           |                     |   |                          |    |  |
| Claremont SC                            | A                   | 0.04  | 0.002                    | 53 | 0.85   |
| Claremont SC                            | B                   | 0.04  | 0.002                    | 53 | 0.85   |
| Claremont SC                            | C                   | 0.10  | 0.003                    | 53 | 0.91   |
| Claremont SC                            | E                   | 0.05  | 0.002                    | 53 | 0.89   |
| Claremont GM                            | A                   | 0.01  | 0.002                    | 53 | 0.90   |
| Claremont GM                            | B                   | 0.01  | 0.002                    | 53 | 0.91   |
| Claremont GM                            | C                   | 0.07  | 0.001                    | 53 | 0.95   |
| Claremont GM                            | E                   | 0.01  | 0.001                    | 53 | 0.95   |
| Claremont UI                            | A                   | -0.01                                       | 0.001                    | 52 | 0.91   |
| Claremont UI                            | B                   | 0.00  | 0.001                    | 52 | 0.92   |
| Claremont UI                            | C                   | 0.05  | 0.001                    | 52 | 0.94   |
| Claremont UI                            | E                   | 0.00  | 0.001                    | 52 | 0.91   |
| Long Beach SC                           | A                   | -0.08                                       | 0.007                    | 55 | 0.46   |
| Long Beach SC                           | B                   | -0.07                                       | 0.007                    | 55 | 0.46   |
| Long Beach SC                           | C                   | -0.03                                       | 0.005                    | 55 | 0.68   |
| Long Beach SC                           | E                   | -0.05                                       | 0.004                    | 55 | 0.78   |
| Rubidoux UI                             | A                   | 0.15  | 0.012                    | 36 | 0.82   |
| Rubidoux UI                             | B                   | 0.16  | 0.013                    | 36 | 0.82   |
| Rubidoux UI                             | C                   | 0.08  | 0.012                    | 36 | 0.71   |
| Rubidoux UI                             | E                   | 0.05  | 0.008                    | 36 | 0.76   |

Table 2.3 (continued):

| Site and<br>Nephelometer <sup>(a)</sup> | Case <sup>(b)</sup> | bias<br>( $\text{km}^{-1}$ ) <sup>(c)</sup> | variance<br>of residuals | n  | correlation<br>coefficient <sup>(d)</sup><br>(r) |
|---|---------------------|---|--------------------------|----|--|
| <i>fall</i>                             |                     |   |                          |    |  |
| Central LA SC                           | A                   | 0.30  | 0.099                    | 27 | 0.87   |
| Central LA SC                           | B                   | 0.31  | 0.101                    | 27 | 0.87   |
| Central LA SC                           | C                   | 0.14  | 0.020                    | 27 | 0.88   |
| Central LA SC                           | E                   | 0.12  | 0.013                    | 27 | 0.82   |
| Long Beach SC                           | A                   | 0.08  | 0.027                    | 29 | 0.78   |
| Long Beach SC                           | B                   | 0.09  | 0.028                    | 29 | 0.78   |
| Long Beach SC                           | C                   | 0.09  | 0.027                    | 29 | 0.83   |
| Long Beach SC                           | E                   | 0.06  | 0.018                    | 29 | 0.81   |
| Long Beach GM                           | A                   | 0.12  | 0.010                    | 29 | 0.96   |
| Long Beach GM                           | B                   | 0.13  | 0.010                    | 29 | 0.96   |
| Long Beach GM                           | C                   | 0.14  | 0.010                    | 29 | 0.96   |
| Long Beach GM                           | E                   | 0.06  | 0.004                    | 29 | 0.95   |

<sup>(a)</sup>SC indicates SCAQS network nephelometer; GM – General Motors Research Laboratories nephelometer; UI – University of Illinois nephelometer.

<sup>(b)</sup>Cases A, B, and C are from the Mie scattering model as described in the text and in Table 2.2; Case E is from an empirical model and is provided for comparison to the theoretical model as described in the text.

<sup>(c)</sup>The bias is defined as the mean residual (predicted - observed) value; the variance of the residuals is in units of  $\text{km}^{-2}$ .

<sup>(d)</sup>Pearson correlation coefficient

order to explore the likely level of light scattering by the aerosol under ambient conditions. The refractive index of the wet aerosol was estimated by the volume-averaged method with water included as estimated by Sloane's (1984b) method. Calculated light scattering by the humidified aerosol (Case D) is compared to the time series of dry aerosol scattering (Case C) in Figure 2.8. It is seen that the effect of humidifying the aerosol is particularly important for certain time periods at Rubidoux, and at Long Beach during the fall period.

Finally, light absorption by  $\text{NO}_2$ , light absorption by black carbon particles, and light scattering by air molecules were added to the light scattering by particles previously calculated in Case D in order to compute the total extinction coefficient according to equation 2.1. Results indicate that light scattering by fine particles dominates the visibility problem at each monitoring site. The contribution of the light scattering by particles to the total extinction coefficient ranges from 68 to 88 percent at the sites studied. Light absorption by black carbon particles makes an increasingly important contribution to the extinction coefficient in the fall months at Long Beach and Central Los Angeles, contributing 14 and 17 percent of the total extinction coefficient respectively, compared to 9.0, 5.3, and 5.7 percent of the total extinction coefficient at Claremont, Long Beach, and Rubidoux, respectively, in the summer.

### 2.9.1 Visual Range Results

The extinction coefficient values calculated in Case D next were translated into estimated visual range values using Koschmieder's formula (Middleton, 1952) with threshold contrast values of 0.02 and 0.05. The threshold constant

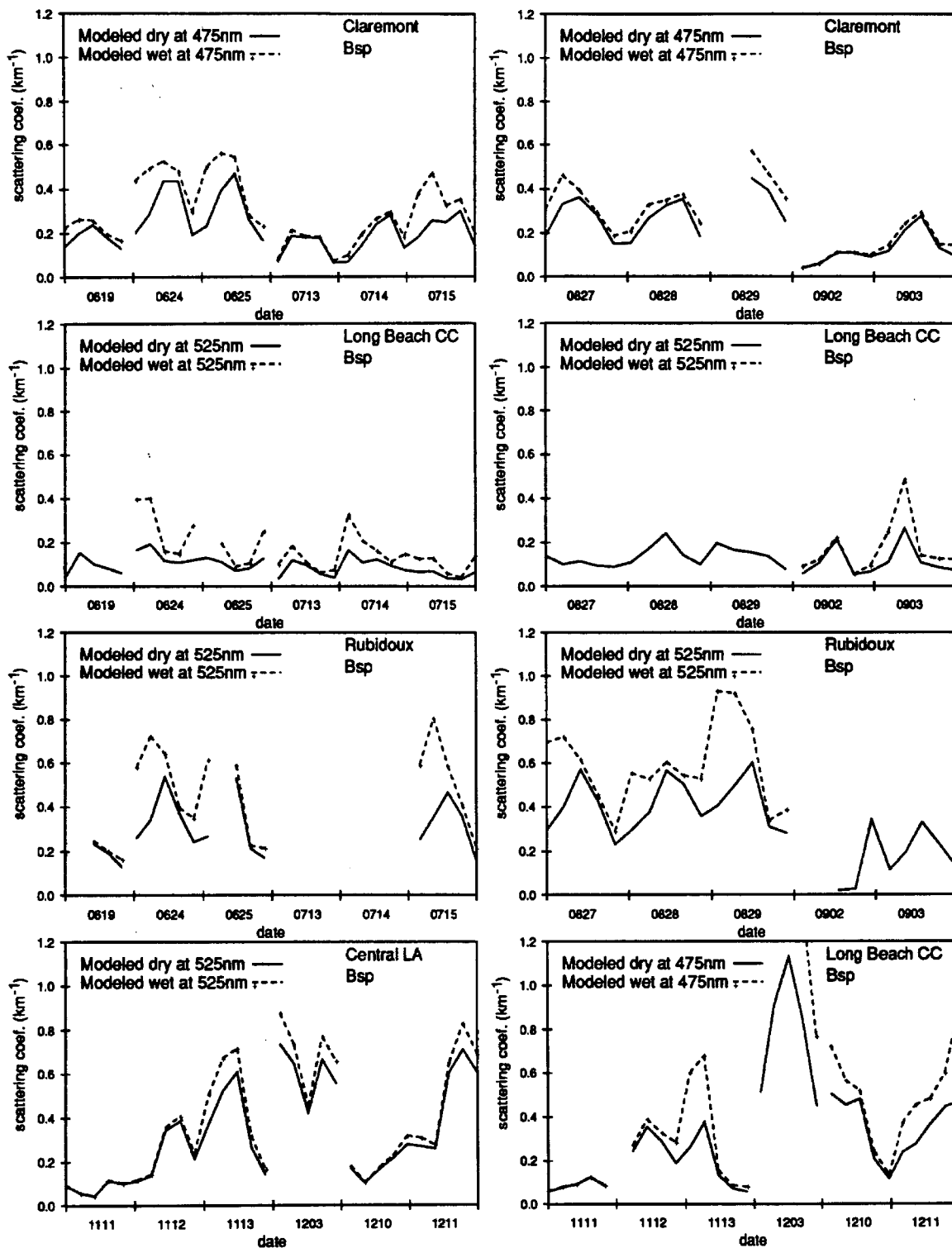


Figure 2.8: Comparison of light scattering computed for a dry aerosol (solid line, Case C) to light scattering by a wetted aerosol (dashed line, Case D).

of 0.02 was originally employed by Koschmieder for visual range calculations, although a value of 0.05 produces better agreement with reported visual range observations (Gordon, 1984). These visual range values then were compared with visual range values recorded by human observers at nearby airports during SCAQS as shown in Figure 2.9. The Claremont air monitoring site was paired with visual range data from Ontario International Airport which is located at a distance of 10 kilometers southeast of the Claremont site. Model predictions at the Rubidoux air monitoring site were compared to visual range observations at Riverside Municipal Airport (located 8.2 kilometers southwest of Rubidoux) and at Riverside - March Air Force Base (located 16 kilometers southeast of Rubidoux). The Long Beach air monitoring site was matched with observations at Dougherty Field located 1.7 kilometers to the southwest of the Long Beach air monitoring site. Figure 2.9 shows quite good agreement between observations and model predictions of visual range in the Rubidoux/Riverside area that is confirmed by simultaneous independent observations at two airports. The agreement at Long Beach and in the Claremont/Ontario area is better when a contrast threshold of 0.05 is used than with the lower contrast threshold. It is interesting to note that model predictions are in close agreement with nephelometer values (see Figure 2.7) at the two times when visibility model results depart from airport reports of visual range by human observers (September 2 at Claremont, July 15 at Long Beach). This indicates that local misestimation of light scattering at the location of the air monitoring sites is not the most likely cause of a misestimation of human observer visual range. Instead, differences in predicted versus observed visual range in those cases might be due to the 10 kilometer spatial separation between Claremont and Ontario airport and

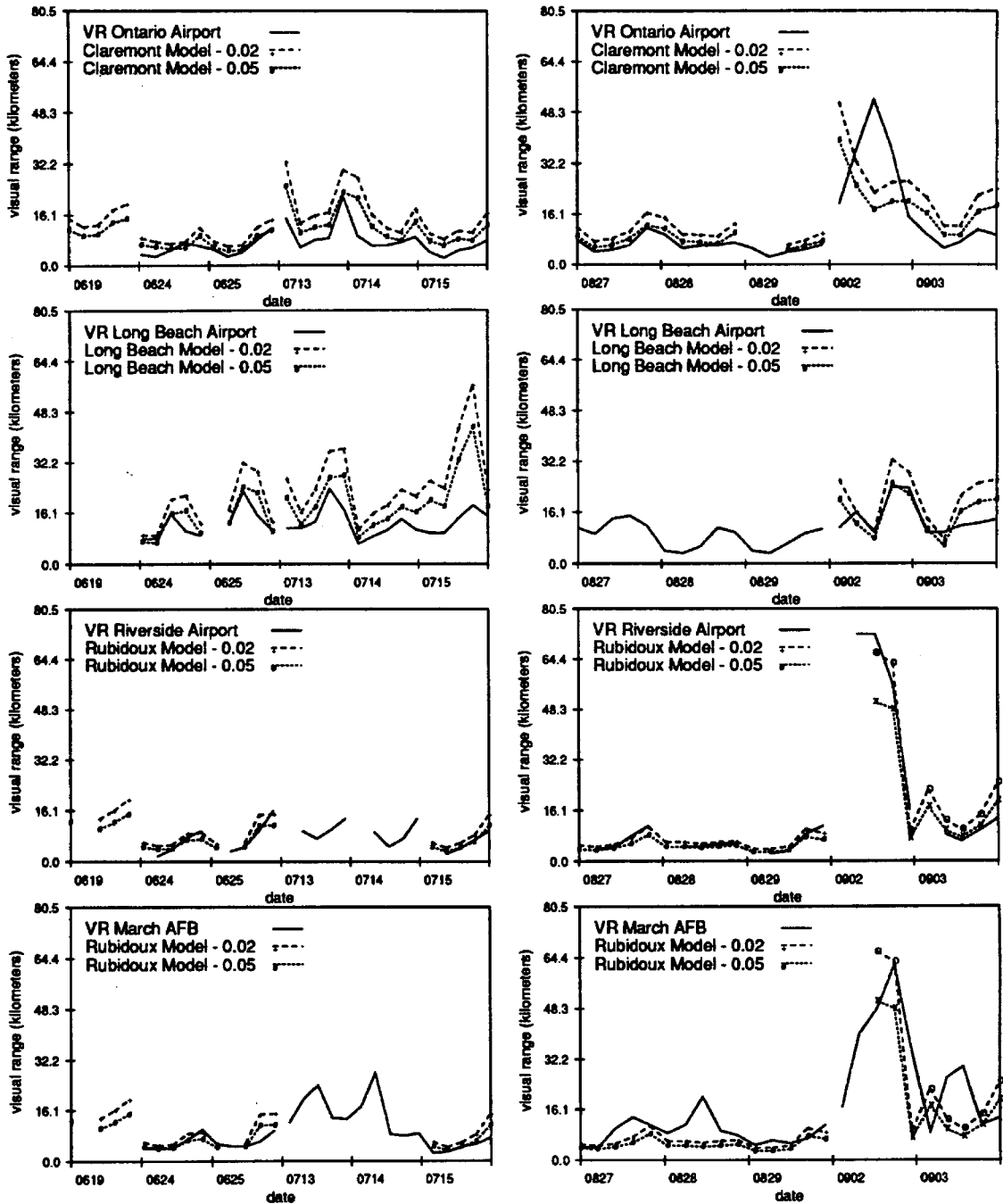


Figure 2.9: Comparison of visual range (VR) calculated via Koschmieder's formula using contrast thresholds of 0.02 and 0.05 and model predictions of the extinction coefficient to visual range observations made by Federal Aviation Administration human observers at the closest airports to the monitoring sites. Case D extinction coefficient values are used with the exception of 0902 and 0903 at Rubidoux, where Case C is used due to lack of relative humidity data.

to possible spatial inhomogeneities in the aerosol cloud that are visible to human observers but are not noted by the nephelometer.

### 2.9.2 Comparison to Empirical Models for Light Scattering

Empirical visibility models are widely used for translating data on aerosol chemical composition into estimates of light scattering or visual range (Trijonis *et al.*, 1990; NRC, 1993). In these models, the extinction or scattering coefficient is related to the sum of the products of the light extinction efficiency of each major aerosol chemical species multiplied by the ambient concentration of that species at a particular time. Such models can be divided into two categories: (1) those that are fit using statistical methods to the time series of concurrent local measurements of aerosol composition and light extinction or scattering and (2) those models that are used to make estimates of light scattering or extinction given data only on aerosol chemical composition plus consensus values of the light scattering or extinction coefficient per unit mass for various aerosol chemical species as documented in the prior scientific literature. In essence, empirical models of type (2) above represent an aggregation of the results observed over many modeling studies of type (1).

The Mie scattering model used in the present study can be compared to the consensus empirical models of type (2) just defined. Both the present Mie scattering model and a consensus empirical model are capable of making light scattering, light extinction, or visual range predictions for a single aerosol sample and also work independently of any concurrent light scattering or extinction observations. The most widely applied consensus empirical model in current use is that employed by the U. S. National Acid Precipitation

Assessment Program's visibility assessment study (Trijonis *et al.*, 1990) and also by a recent visibility study conducted for the National Research Council (NRC, 1993). One equation used is typically

$$b_{sp} = 4.25SO_4 + 4.25NO_3 + 3.25OC + 1.5EC + 1.25SOIL \quad (2.2)$$

where  $b_{sp}$  is the fine particle light scattering coefficient ( $10^{-6}m^{-1}$ ),  $SO_4$  is 1.4 times the measured fine sulfate ion concentration ( $\mu g m^{-3}$ ), assuming that the sulfate is found as ammonium sulfate,  $NO_3$  is 1.3 times the measured fine nitrate ion concentration ( $\mu g m^{-3}$ ), assuming that the nitrate is found as ammonium nitrate,  $OC$  is 1.5 times the measured organic carbon concentration ( $\mu g m^{-3}$ ),  $EC$  is the fine elemental carbon concentration ( $\mu g m^{-3}$ ),  $SOIL$  is the remaining fine particle material ( $\mu g m^{-3}$ ), and the numerical coefficients are consensus scattering coefficients per unit mass for those pollutant species. The model of equation 2.2 was applied to each aerosol data set at each SCAQS site during each time period of interest and the results are displayed as Case E in Table 2.3. It is seen that the bias, variance of residuals, and correlation coefficient of the empirical model compared to nephelometer data are similar to the comparison of the theoretical model and nephelometer data.

## 2.10 Conclusions

Aerosol size distribution data and filter based measurements of aerosol chemical composition were collected during the summer and fall of 1987 by the SCAQS air monitoring network. A visibility model has been constructed that connects these data to explain aerosol light scattering coefficient values and visual range values in time series at four air monitoring sites via Mie theory.

A set of consistency checks were performed on the aerosol data base. The measured aerosol anions and cations were found to be in close agreement. The gravimetrically determined aerosol mass concentrations were compared to the sums of the mass concentrations of identified chemical species, and again reasonable agreement was found between these two data sets. A high correlation also was found between the aerosol volume measured by the aerosol size distribution instruments and the aerosol volume inferred from the filter samples. Hence, it is concluded that the SCAQS aerosol data base displays sufficient internal consistency to be used for the purpose of model evaluation studies requiring size distributed aerosol data, including the present visibility modeling study. The light scattering coefficient values measured during SCAQS by different monitoring agencies were not always in agreement and discussions with the owners of the instruments used have pinpointed some of the reasons for their disagreement. No visibility model can be expected to produce exact agreement with all of the light scattering values measured during SCAQS because the light scattering data are in conflict to some degree. Based on our investigations, the GM and UI nephelometer data sets raise the fewest questions and hence are probably the most reliable; the SCAQS network SC nephelometer measurements at Long Beach in the summer and at Central Los Angeles in the fall periods are of doubtful accuracy.

The light scattering coefficient values calculated from the visibility model were found to reproduce the time series of measured light scattering coefficient values well in those cases where redundant nephelometer measurements were available at a particular air monitoring site to confirm that the measured light scattering values were correct. Total light extinction coefficient values, which can be converted easily to estimates of standard visual range

via Koschmieder's formula, also were computed at each monitoring station and compare favorably to visual range observations at nearby airports.

Based on this study, it appears feasible to maintain a network of monitoring sites that can be used to track the changes in aerosol size distributions and chemical composition in time and space over a large regional airshed. Such data can be used to account for the relationship between pollutant properties and visual range via modeling calculations based on Mie theory. Such data can later be used to test the performance of forthcoming airshed models that seek to predict the size distribution and chemical composition of the atmospheric aerosol. Obviously, this opens the possibility of testing the predictions of combined models that compute visual range predictions directly from data on source emissions.

## **3 A Source – Oriented Model for Air Pollutant Effects on Visibility**

### **3.1 Introduction**

Severe visibility problems exist that need to be understood at a level where emission controls applied at air pollutant sources can be studied to determine the resulting changes in visual range. Several approaches are available that could be used to link source emissions to visual air quality. The simplest of these is the use of speciated rollback air quality models linked to empirical visibility models (NRC, 1993) in which changes in light scattering and absorption in the atmosphere by major chemically-identified particulate matter species such as sulfates, nitrates and carbon particles are taken to be directly proportional to the changes in source emissions of chemically similar precursors. In such models, aerosol sulfate concentrations would be assumed to change in proportion to gas-phase SO<sub>2</sub> emissions, and the effect of sulfate particles on light scattering would be estimated from statistical analysis of historical data sets on atmospheric light scattering in relation to day to day changes in aerosol sulfate concentrations, for example. Alternatively, mechanistic models can be envisioned that rely on a description of the size distribution and chemical composition of particulate matter emissions at their source plus the emissions of gaseous aerosol precursors. These emissions

are tracked as they undergo atmospheric transport, chemical transformations leading to gas-to-particle conversion in the atmosphere, and dry deposition, resulting in predictions of the size distribution and chemical composition of the atmospheric particles and gases at downwind receptor sites. This information on particle size distribution and chemical composition then could be used to support light extinction calculations based on Mie theory. The empirically-based rollback models for visibility impairment exist and have been demonstrated, while mechanistic models of the second type could be assembled from available component parts (NRC, 1993).

The purpose of the present work is to formulate a mechanistic model for the prediction of particle light scattering levels and visual range that is driven directly by data on source emissions and meteorological observations. Model predictions will be tested against observations taken during the 1987 Southern California Air Quality Study (SCAQS).

### **3.1.1 Conceptual Formulation of the Problem**

Consider an air parcel containing particulate matter corresponding to remote background concentrations. It contains low concentrations of ionic material such as sea salt and sulfates, dilute combustion aerosols at low background concentrations, and possibly some soil dust if the air parcel has been over land recently. The air parcel then encounters an urban area where primary aerosol from fuel combustion and other human activities is inserted. The combined background plus primary particulate matter emissions become the "seed aerosol" on which condensation and heterogenous reaction processes take place. To model these processes, the size distribution and chemical composition of primary aerosol sources must be accurately described, and the

background aerosol must be characterized by both chemical composition and size distribution. Reactive gas emissions into the air parcel, including sulfur dioxide, nitrogen oxides, ammonia, and volatile organics that can later lead to formation of new particulate matter by atmospheric chemical reaction, also must be known.

Urban aerosols are sufficiently dilute that coagulation is not of major practical importance. In particle sizes larger than about  $0.1 \mu\text{m}$  particle diameter, particle number counts arising from background and new primary emissions are nearly conserved unless removal occurs by wet or dry deposition. Therefore, a model that hypothetically follows single particles as they evolve in the presence of condensation, heterogeneous reaction, and deposition is possible.

A chemically- and size-resolved seed particle is inserted into an air parcel in which the gas-phase chemistry of potential secondary aerosol precursors can be tracked. Over time material is transferred from the gas-phase to the particle phase (or vice versa), limited by either kinetic considerations of mass transfer rates or, alternatively, limited by having reached thermodynamic equilibrium between the gas and particle phase. Species transferred in this manner include water vapor, ammonia, nitric acid vapor, hydrochloric acid vapor, sulfuric acid, and condensible organic vapors. In general, in a polluted environment, secondary sulfates, nitrates, and organics accumulate on the primary seed particles, while HCl derived from sea salt chloride may be liberated from some particles (Eldering *et al.*, 1991).

If the seed particles, with their accumulation of secondary material, enter a condition where fog would form, particles larger than a critical size determined by particle composition and the ambient water vapor supersaturation

are activated. Those particles grow rapidly, and enough water accumulates to permit an aqueous phase reaction system in which  $\text{SO}_2$  dissolved in droplets can be oxidized by species such as  $\text{H}_2\text{O}_2$  and  $\text{O}_3$  scavenged from the photochemical smog contained in the surrounding gas-phase. Dissolved  $\text{SO}_2$  also could be oxidized by oxygen in the presence of metal catalysts. If the fog evaporates, the fog droplets attempt to dry out, leaving in their place a smaller nucleus of the non-volatile materials that were once contained in the fog drops.

Meanwhile, sedimentation and other dry deposition processes remove particles from the system. For the air parcel as a whole, particles grow in size and new particles accumulate as long as fresh emissions exceed the rate of removal processes. Should the air parcel leave the source region and travel into the countryside, it is possible that dilution and removal processes would act to reduce particle concentrations over time.

If enough particles of the right size and refractive index accumulate in the air parcel, the extinction coefficient increases to the point where a visibility problem becomes pronounced. By tracking the background and primary seed particles and pollutant gases as they evolve in the air parcel, a model can be constructed for predicting the number concentration, size distribution, and chemical composition of the aerosol that results with sufficient detail that light scattering and absorption calculations can be performed via Mie theory. A model that connects source emissions to light scattering and absorption by particles, when added to light scattering by air molecules and light absorption by  $\text{NO}_2$ , results in a model for the effect of source emissions on the atmospheric extinction coefficient as a function of wavelength. That model for the extinction coefficient can be used to predict the effect

of emissions changes on visual range via Koschmieder's formula (Middleton, 1952) and can be used to generate full color photographs of the effect of emissions changes based on the visual character of a scene using image-processing based visibility models like those of Eldering *et al.* (1993).

Since we describe a process that starts with single primary particles and follows their evolution within an air parcel, it is logical to begin with a Lagrangian trajectory model for the air parcel, especially in cases where a serious visibility reduction problem is to be studied having a distance to extinction of only a few kilometers, consistent with the dimensions of the air parcels tracked by such a trajectory model. Within that trajectory model, we seek to embed a model for the background aerosol, a model for the primary aerosol source emissions, a photochemical gas-phase mechanism and emissions model that will propagate aerosol precursor formation (e.g.,  $\text{HNO}_3$  production) and oxidant production (e.g.,  $\text{O}_3$ ,  $\text{H}_2\text{O}_2$  production), a model for the diffusion of gases to and from the particle phase, a fog chemistry model, a dry deposition module, and a light scattering code. Such components are available from a number of prior studies or from experimental work performed in support of the present model construction effort. The remainder of this chapter describes the assembly of the above pieces of the visibility modeling system into an integrated whole. The model then will be tested by application to source emissions data and atmospheric data taken in Southern California.

### 3.1.2 Mathematical Modeling of Air Pollutant Effects on Visibility

The mathematical model discussed in this chapter simulates atmospheric gas-phase chemistry, vertical diffusion of gases and aerosols, horizontal advection of gases and aerosols, ground-level deposition of gases and aerosols, the movement of condensible organic and inorganic gases between the gas and aerosol phase, heterogeneous sulfate formation, and light scattering and absorption. A Lagrangian formulation of the atmospheric diffusion equation is employed in this work, as described by Russell *et al.* (1983) with the changes described below.

The general form of the atmospheric diffusion equation employed by Lagrangian trajectory models is

$$\frac{\partial c_{ik}}{\partial t} = \frac{\partial}{\partial z} \left( K_{zz} \frac{\partial c_{ik}}{\partial z} \right) + M_{ik}(c_{1k}, c_{2k}, \dots, c_{nk}, T, RH); \quad i = 1, 2, \dots, n, k = 1, 2, \dots, m \quad (3.1)$$

where  $c_{ik}$  represents the concentration of species  $i$  of size  $k$  (if applicable),  $K_{zz}$  is the turbulent eddy diffusivity in the vertical direction,  $z$ ,  $M_{ik}$  represents the net rate of gain of each species due to chemical reaction or possibly condensation, which is generally a function of the species concentrations, temperature,  $T$ , and relative humidity,  $RH$ .

Specifically, in the absence of heterogeneous atmospheric chemistry that will occur if a fog exists, the equation for aerosol species  $i$  of size  $k$  takes the following form.

$$\frac{\partial c_{ik}}{\partial t} = \frac{\partial}{\partial z} \left( K_{zz} \frac{\partial c_{ik}}{\partial z} \right) + L_{ik}(C, T, RH); \quad i = 1, 2, \dots, n, k = 1, 2, \dots, m \quad (3.2)$$

with initial conditions

$$c_{ik}(z, 0) = c_{ik}^o(z), \quad t = 0 \quad (3.3)$$

and boundary conditions

$$(K_{zz} \frac{\partial c_{ik}}{\partial z}) = 0, \quad z = H \quad (3.4)$$

$$[v_p^k c_{ik} - K_{zz} \frac{\partial c_{ik}}{\partial z}] = E_{ik}, \quad z = 0 \quad (3.5)$$

In this equation,  $L_{ik}(C, T, RH)$  is the rate of gain or loss of aerosol material due to the movement between the gas and aerosol phase by diffusion, which is a function of the aerosol species concentrations and gas-phase concentrations, denoted by  $C$ . Initial species concentrations are denoted by  $c_{ik}^o(z)$ , and  $H$  is the height of the air column. The particle deposition velocity,  $v_p^k$ , is dependent on meteorology, surface roughness, and particle size, and the  $E_{ik}$  are size- and chemically-specified direct emissions from primary particle sources. Coagulation of particles is neglected for the case of the relatively dilute atmospheric systems of interest to regional air pollution problems.

For gas-phase species  $i$ , equation (3.1) takes the form

$$\frac{\partial c_i}{\partial t} = \frac{\partial}{\partial z} (K_{zz} \frac{\partial c_i}{\partial z}) + R_i(c_1, c_2, \dots, c_n, T) - \sum_k L_{ik}(C, T, RH); \quad i = 1, 2, \dots, n \quad (3.6)$$

with initial conditions in addition to equation (3.3)

$$c_i(z, 0) = c_i^o(z), \quad t = 0 \quad (3.7)$$

and boundary conditions in addition to equations (3.4) and (3.5).

$$(K_{zz} \frac{\partial c_i}{\partial z}) = 0, \quad z = H \quad (3.8)$$

$$[v_g^i c_i - K_{zz} \frac{\partial c_i}{\partial z}] = E_i, \quad z = 0 \quad (3.9)$$

$R_i(c_1, c_2, \dots, c_n, T)$  in equation (3.6) represents the rate of production or loss of species  $i$  at temperature  $T$  due to gas-phase chemical reactions.

$L_{ik}(C, T, RH)$  represents the movement of material between the gas and aerosol phase, as defined previously. Initial gas-phase species concentrations are denoted by  $c_i^o(z)$ ,  $H$  is the height of the air column,  $v_g^i$  is the deposition velocity for gaseous species  $i$ , and  $E_i$  represents direct emissions of species  $i$ .

A light scattering module is applied to calculate the light extinction coefficient. The atmospheric light extinction coefficient can be expressed as the sum of four contributions.

$$b_{ext} = b_{sp} + b_{ap} + b_{sg} + b_{ag} \quad (3.10)$$

The extinction coefficient is the sum of the components due to light scattering by particles,  $b_{sp}$ , light absorption by particles,  $b_{ap}$ , scattering of light by gases,  $b_{sg}$ , also known as Rayleigh scattering when the gas is air, and light absorption by gases  $b_{ag}$ . Light scattering and absorption by particles is calculated from Mie theory (van de Hulst, 1957).

$$b_{sp,sp+ap} = \int \frac{\pi d_p^2}{4} Q(m, \lambda, d_p) n(d_p) dd_p \quad (3.11)$$

The light scattering (+ absorption) coefficient is a function of the scattering (+ absorption) efficiency of a particle,  $Q$ , with refractive index  $m$ , particle diameter  $d_p$ , as a function of the wavelength of light  $\lambda$  and the particle number distribution,  $n(d_p)$ . The scattering (+ absorption) efficiency is calculated from Mie theory for each diameter interval of the aerosol particle size distribution. Then  $b_{sp}$  (and  $b_{sp+ap}$ ) are calculated by integrating the product of the scattering (+ absorption) efficiency factors for particles of each size, particle cross sectional area, and the number of such particles per unit air volume over the diameter range represented by the aerosol size distribution. Light absorption by  $\text{NO}_2$  gas is calculated according to the wavelength-dependent

absorption coefficients reported by Hodkinson (1966). Scattering by gases is calculated as Rayleigh scattering, with  $b_{sg} = 1.5 \times 10^{-5} m^{-1}$  at a wavelength of 550 nm, and  $b_{sg}$  varying with wavelength as  $\lambda^{-4}$  (Penndorf, 1957). These calculation procedures are described in detail by Larson *et al.* (1988). The result provides values of the atmospheric light extinction coefficient as a function of wavelength that can be used to estimate visual range via Koschmieder's formula. The extinction coefficient values also can be used to drive a model that generates synthetic photographs of the appearance of the location occupied by the air parcel (Eldering *et al.*, 1993).

### 3.1.3 Emissions Model

Emissions information is required for gas-phase and particle-phase species. The emissions model developed for use with this modeling system assumes that external input data are supplied on the spatial and temporal distribution of the emissions of total suspended particulate matter mass (but not size or chemical composition) along with emissions of SO<sub>2</sub>, NO, NO<sub>2</sub>, NH<sub>3</sub>, CO, and total non-methane organic gases.

The primary particulate matter mass emissions supplied to the modeling system are subdivided to create a specific number of primary seed particles of specified size and chemical composition released per unit time from each source. This primary particle generation system is based largely on source tests conducted by our research group for use in building this emissions model (Hildemann *et al.*, 1989; 1991ab). A portable dilution source sampling system was designed by Hildemann *et al.* (1989) in which direct emissions from high-temperature (e.g., combustion) sources are cooled by dilution with purified air before sampling. Organic and inorganic compounds that are in

the vapor phase at high stack temperatures are allowed to condense onto the pre-existing solid particles within the sampler before sampling as they would within the plume immediately downwind of the source. The submicron size distribution of the particulate matter emissions from the source are measured using a TSI model 3030 electrical aerosol analyzer (EAA). The mass emission rate of fine particulate matter (particle diameter less than  $2\ \mu\text{m}$ ) is measured by filtration onto Teflon filters located downstream of cyclone separators. The chemical composition of the fine particle emissions is measured from several samples collected in parallel on quartz fiber and Teflon membrane filters. The particulate matter collected is analyzed to determine a material balance in its chemical composition including sulfate, nitrate, chloride, sodium, and ammonium ions, organic carbon, elemental carbon, and the concentration of 32 other elements, including possibly important catalytic metals such as iron (Fe), manganese (Mn), and vanadium (V). Using this system, the mass emission rate, size distribution, and chemical composition of fine aerosol emissions have been measured from catalyst-equipped automobiles, non-catalyst automobiles, diesel engines, distillate oil-fired boilers, fireplace combustion of wood, meat charbroiling, and meat frying. In the case of natural gas appliances, the mass emission rate and chemical composition were measured using the dilution sampling system, while high resolution size distribution data for this source are taken from the work of Li and Hopke (1993). The major fugitive dust source in cities is paved-road dust kicked up by passing traffic. Its chemical composition was determined by grab sampling, followed by resuspension and collection on filters located downstream of cyclone separators, followed by chemical analysis as before (Hildemann *et al.*, 1991a). Soil dust chemical composition (e.g., from unpaved roads) is as

reported by Houck *et al.* (1989). The relative proportions of road dust and soil dust in sizes smaller than 10  $\mu\text{m}$ , smaller than 2.5  $\mu\text{m}$ , and smaller than 1.0  $\mu\text{m}$  are taken from measurements by Houck *et al.* (1989). The detailed size distribution of the paved-road dust as well as all other crustal source emissions in sizes below 2.5  $\mu\text{m}$  is taken as having a shape proportional to the impactor measurements of fine atmospheric soil dust reported for Claremont, California by Zhang *et al.* (1993). The size distribution of the emissions of the larger road dust and soil dust particles in the range from 2.5  $\mu\text{m}$  to 10  $\mu\text{m}$  is taken as having the same shape as the coarse airborne particle size distributions measured in central Los Angeles by Christoforou (1993).

Examples of these source-specific primary particle size distributions are plotted in Figure 3.1. That figure presents the data at a resolution of 5 particle size intervals per decade in the particle size range from 0.01  $\mu\text{m}$  to 10.0  $\mu\text{m}$  particle diameter. Higher size resolution is easily attained if desired because the underlying inverted size distributions have been published previously in all cases except for the soil dust distribution in sizes larger than 2.5  $\mu\text{m}$ . The chemical composition of all particles from the same source is taken to be identical within the size range represented by a single filter-based determination of chemical composition, but chemical composition varies from one source to another. The sources shown in Figure 3.1, plus those very similar sources that can be represented by the same profiles, account for 90% of the primary seed particle mass inserted into the Southern California atmosphere, for example, and probably a similar fraction of the emissions in other urbanized regions. For the remaining minor sources that lack high resolution submicron size distribution data, gross approximations to their size distribution can be obtained from source profile libraries that give mass fractions in

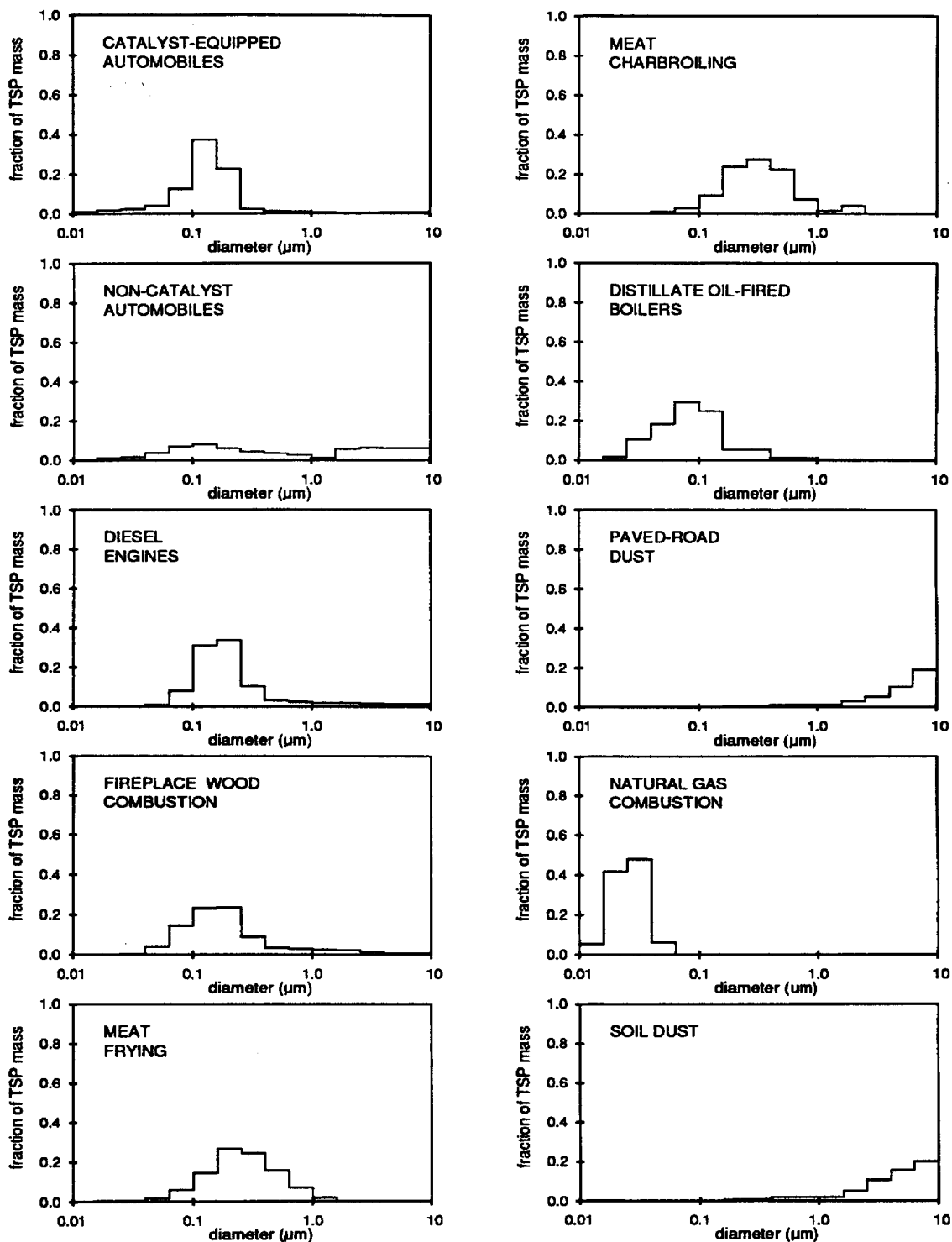


Figure 3.1: Source-specific primary particle size distributions. The particle diameter range between 0.01 and 10  $\mu\text{m}$  is divided into 15 equally spaced intervals on a logarithmic scale, and the fraction of total particulate mass emissions (TSP) falling into each of these size bins is shown. For material, such as soil dust, that is emitted in part in particles greater than 10  $\mu\text{m}$  in diameter, the fraction emitted in particles less than 10  $\mu\text{m}$  in diameter will not sum to 1.0.

size intervals less than 1  $\mu\text{m}$ , 2.5  $\mu\text{m}$ , and 10  $\mu\text{m}$  particle diameter (Cooper *et al.*, 1989; Houck *et al.*, 1989; Taback *et al.*, 1979; Allen, 1992).

The emissions of all major ionic species ( $\text{NH}_4^+$ ,  $\text{Na}^+$ ,  $\text{SO}_4^-$ ,  $\text{NO}_3^-$ ,  $\text{Cl}^-$ ) plus organic compounds, elemental carbon, and crustal (i.e., soil-like) material are tracked separately in the emissions that enter the model. Trace metals-rich industrial process materials are tracked as a single lumped chemical class but individual trace metals are not tracked separately as they compose only a small fraction of the total mass. The air quality model uses a number of discrete particle sizes,  $k$ , with diameters  $d_k$ , that initially are specified by the user but that grow as the aerosol evolves over time. The particulate matter emissions information is input as an increment to the particle number count and chemical composition for each particle size at each time step by sampling from the underlying size distribution of the emissions from each source at the then current size of the particles of class  $k$ . In the model application that follows, the aerosol will be represented as if it is an internal mixture (all ambient particles of the same size have the same chemical composition), but the model is clearly capable of separately tracking particles from different sources with different compositions and ages since release; it is a matter of more computer time and memory.

Organic vapor profiles that specify the detailed chemical composition of the effluent from major emissions source types, including catalyst and non-catalyst equipped gasoline-powered motor vehicles, diesel vehicles, solvent evaporation and surface coating applications, among others, have been assembled recently by our research group (Harley *et al.*, 1992). These vapor-phase organics species profiles are used to map the total organics emissions into the emissions of over 400 specific organic compounds. This improved

chemical resolution for the vapor-phase organics is important for two reasons. First, secondary organic aerosol formation is driven by some organic vapor-phase species but not others; a detailed knowledge of precursor composition and concentrations is required. Second, the composition of the organics influences the production of oxidants (e.g.,  $O_3$ ,  $H_2O_2$ ) that are important to heterogeneous sulfate formation in clouds and in fogs.

#### 3.1.4 Advection

Primary particles and gaseous pollutants specified by the emissions model just described are injected into a vertical stack of five computational cells that represent an air parcel that is advected across the air basin by the observed winds. The horizontal motion of the air parcel is described by trajectories calculated from windfields that are generated by interpolation of meteorological observations by the method of Goodin *et al.* (1979). Vertical transport and diffusion within the stack of computational cells that constitutes the air parcel is described by Russell *et al.* (1983) and Russell and Cass (1986).

#### 3.1.5 Gas Phase Chemical Kinetics

The chemical mechanism used to model the gas-phase chemical reactions is based on the formulation of Carter (1990) with extensions to track condensible organic gases that may form secondary organic aerosols (Pandis *et al.*, 1992a). The extended mechanism includes 100 chemical species and 195 reactions.

Of particular interest are the reactions which lead to the precursors for inorganic aerosol formation. Nitric acid is produced by reaction of the hydroxyl radical and  $NO_2$ , reaction of  $N_2O_5$  with  $H_2O$ , the reaction of the

hydroperoxyl radical with  $\text{NO}_3$ , and a series of  $\text{NO}_3$ -organics reactions.  $\text{SO}_2$  conversion to sulfuric acid in the gas phase occurs by reaction with OH, and by reaction of  $\text{SO}_2$  with the stabilized Criegee biradicals formed due to ozone-alkene reactions. The numerical solver for the gas-phase chemistry uses the approach of Young and Boris (1977) as implemented by previous versions of the CIT airshed model (McRae *et al.*, 1982).

### 3.1.6 Solar Radiation Fields

Earlier versions of the present trajectory model computed photolysis rate constants from an actinic flux model for clear sky conditions based on solar position and time of day (McRae *et al.*, 1982; Russell *et al.*, 1983; Russell and Cass, 1986). As discussed by Harley (1993), photolysis rates may differ from those predicted from actinic flux models due to pollutant concentrations and cloud cover. The present trajectory model accepts a temporally varying ground-level photolysis scaling factor field and a regionwide insolation correction factor applied at the upper boundary of the model that can be set based on field measurements of the ultraviolet solar flux. The vertical variation of photolysis rate constants is estimated by linear interpolation between ground level photolysis rates and the photolysis rates at the top of the air parcel. The model also accepts a total solar radiation scaling factor field which can be used to attenuate to clear sky photolysis rates computed by the model's internal solar simulator according to the reported spatial distribution of the fraction of the sky that is covered by clouds.

### 3.1.7 Dry Deposition

The dry deposition of gases is computed using the approach described by McRae *et al.* (1982) and Russell *et al.* (1984). For particles, the dry deposition

velocity is calculated according to the formulation of Slinn and Slinn (1980) for dry particles and Seinfeld (1986). The deposition velocity for particles,  $v_p^k$ , is defined as

$$v_p^k = \frac{1}{r_C^k + r_D^k + r_C^k r_D^k v_s^k(a_d^k)} + v_s^k(a_d^k) \quad (3.12)$$

with

$$(r_C^k)^{-1} = \frac{u_*^2}{\bar{u}} \quad (3.13)$$

and

$$(r_D^k)^{-1} = u_* [(Sc^k)^{-2/3} + 10^{-3/St^k}] \quad (3.14)$$

where  $r_C^k$  is the resistance in the constant flux layer or the aerodynamic resistance, and  $r_D^k$  is the resistance in the deposition layer immediately adjacent to the ground, also called the surface layer resistance.  $Sc^k$  is the Schmidt number for particles of size  $k$  (kinematic viscosity of the air divided by the Brownian diffusivity of particles in air),  $St^k$  is the Stokes number for particles of size  $k$ , and  $v_s^k$  is the gravitational settling velocity of particles with aerodynamic diameter  $a_d^k$ . The mean wind velocity is  $\bar{u}$ , and  $u_*$  is the friction velocity. The particle deposition velocity for particles greater than about 1  $\mu\text{m}$  in diameter is dominated by gravitational settling and inertial impaction. For smaller particles, Brownian diffusion is the dominant process leading to particle deposition. The particle deposition velocity is smallest for particles in the 0.1 to 1  $\mu\text{m}$  diameter range.

### 3.1.8 Diffusion of Gases to and from Particles

To account for the movement of inorganic gases to and from particles, the AIM computer code of Wexler and Seinfeld (1991) is employed. In this calculation scheme the movement of mass is determined by the physical properties (diffusivity), temperature, number of particles present, the ambient

gas-phase concentrations of species and the equilibrium gas-phase species concentrations at the particle surface. To calculate the surface equilibrium concentrations, the aerosol phase state and composition is estimated by assuming that more than one phase is present in the aerosol and that the phases are in thermodynamic equilibrium with the Gibbs free energy at a global minimum. The following equation is then solved for each chemical species present in particles of size  $k$ .

$$\frac{dP_{ik}}{dt} = \frac{4\pi N_k D_i r_k}{\beta + 1} (c_i^\infty - c_i^e) \quad (3.15)$$

In this equation  $P_{ik}$  is the concentration of the  $i$ th chemical species present in particles of size  $k$ ,  $N_k$  represents the number concentration of particles of size  $k$ ,  $D_i$  is the gas-phase molecular diffusivity of species  $i$ , and  $r_k$  is the particle radius.  $\beta$  accounts for imperfect accommodation;  $\beta = D_i/\alpha_i s_i r_k$ , where  $\alpha_i$  is the accommodation coefficient of species  $i$  and  $s_i$  is the molecular velocity of species  $i$ . The ambient gas-phase concentration and the equilibrium gas-phase concentration of species  $i$  at the particle surface are represented by  $c_i^\infty$  and  $c_i^e$ , respectively. Equation (3.15) is written for each condensible chemical species in each of the  $k$  particle sizes, and the equations are solved simultaneously. The species fluxes resulting from this solution step then are used to represent  $L_{ik}$  in expressions (3.2) and (3.6). After solving this set of equations, the diameter of each particle of size  $k$  is recalculated to account for the material added or lost, and the gas-phase species concentrations are updated to reflect material gained or lost by the particles.

For condensible organic gases, a parallel formulation is used. The diffusional growth equation is solved for a number of condensible organic aerosol species. Because the exact saturation vapor pressure of each of the many low

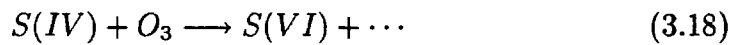
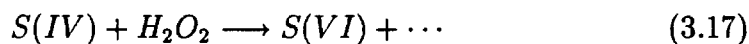
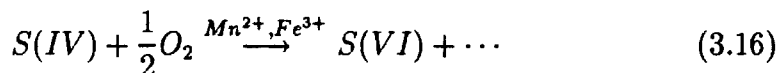
vapor pressure secondary organic reaction products is not known, the secondary organic aerosol material computed from the gas-phase kinetic mechanism is assumed to be transferred entirely to the particle phase. Thus, an upper limit on the secondary organic aerosol concentration is calculated.

The work of Heisler and Friedlander (1977) discusses experiments performed to determine the aerosol growth laws governing secondary aerosols in photochemical smog. In this work, Heisler and Friedlander estimated a critical size or Kelvin cutoff diameter, below which growth did not occur due to the vapor pressure-raising effect of particle surface curvature. From experiments conducted in a Teflon bag smog chamber, they found cutoff diameters of 0.1 to 0.3  $\mu\text{m}$  for secondary organic aerosols produced by reaction from cyclohexene and 1,7-octadiene. When fitting their growth law to observed ambient data, they used a model with two condensible species, the components having critical diameters of 0.055 and 0.24  $\mu\text{m}$ . For the present work, a critical diameter of 0.1  $\mu\text{m}$  will be used, below which no growth by condensation will be allowed to occur.

### 3.1.9 Fog Calculations

Previous investigators have explained elevated sulfate concentrations in urban aerosols with models that simulate the aqueous phase chemistry in fogs, allowing for heterogeneous sulfate formation (Pandis *et al.*, 1992b). More recent work (Meng and Seinfeld, 1994) has shown that droplet-size particles in a size-distributed aerosol can be accounted for by the activation of fine aerosol particles to form fog or cloud drops, followed by aqueous-phase chemistry, and fog evaporation. In the present study, an approximate model of fog processes that takes into account size-specific aerosol chemistry and

gas-phase pollutant concentrations is used. When a trajectory enters a fog, particles are activated according to the predictions of the Köhler equation (Pruppacher and Klett, 1978). Particles that are activated at the assumed supersaturation achieve the diameter of a fog droplet by water addition from the vapor phase. Gases move into the aqueous phase according to Henry's law, subject to mass conservation constraints. Oxidation of dissolved S(IV) species to form sulfate (S(VI)) occurs within the fog droplets by aqueous reactions involving  $H_2O_2$  and  $O_3$ , and oxidation catalyzed by  $Fe^{3+}$  and  $Mn^{2+}$ . The chemical reactions considered are



These three reactions are thought to be the most significant  $SO_2$  oxidation reactions in the pH range of 2–8 (see Pandis and Seinfeld, 1989). The reactions shown in Table 3.1 are propagated by dissolved S(IV) species and by oxidant concentrations determined from the gas-phase photochemical trajectory model, with fog pH values and catalyst levels determined by field experimental observations. The particles that have not been activated continue to interact with the gas-phase as described in Section 3.1.8. When the air parcel trajectory moves out of the fog, the water dissipates and the particles achieve new diameters determined by the drier, non-volatile remaining components now contained in the former fog droplet (e.g., sulfates, sodium compounds, carbonaceous material, and crustal materials) plus any nitrate, chloride, and ammonium that would remain in equilibrium with the new gas-phase conditions.

Table 3.1: Sulfur Species Aqueous Oxidation Rate Expressions

| Oxidant                       | Rate Expression <sup>a</sup>  | Rate Constants   |
|-------------------------------|---|--|
| H <sub>2</sub> O <sub>2</sub> | $R = k[\text{H}^+][\text{HSO}_3^-][\text{H}_2\text{O}_{2(aq)}]/(1+K[\text{H}^+])$                                 | $k = 7.5 \cdot 10^7 \text{ M}^{-1} \text{ sec}^{-1}$<br>$K = 13 \text{ M}^{-1}$  |
| O <sub>2</sub>                | $R = k[\text{Fe(III)}][\text{SO}_3^{2-}]$   | $k = 1.2 \cdot 10^6 \text{ M}^{-1} \text{ sec}^{-1}$ ,<br>pH ≤ 5   |
| O <sub>2</sub>                | $R = k_1[\text{Mn(II)}][\text{HSO}_3^-]$  | $k_1 = 3.4 \cdot 10^3 \text{ M}^{-1} \text{ sec}^{-1}$   |
| O <sub>3</sub>                | $R = (k_0[\text{SO}_2 \cdot \text{H}_2\text{O}] + k_1[\text{HSO}_3^-] + k_2[\text{SO}_3^{2-}])[\text{O}_{3(aq)}]$ | $k_0 = 2.4 \cdot 10^4 \text{ M}^{-1} \text{ sec}^{-1}$<br>$k_1 = 3.7 \cdot 10^5 \text{ M}^{-1} \text{ sec}^{-1}$<br>$k_2 = 1.5 \cdot 10^9 \text{ M}^{-1} \text{ sec}^{-1}$ |

<sup>a</sup>all reaction rates from Hoffmann and Calvert (1985), at 298 K

### 3.1.10 Solution Technique

To create a tractable model, operator splitting was employed in these calculations, with the vertical transport and chemical reactions of the gas-phase species remaining linked in the first calculation step. Vertical diffusion of aerosol species is calculated next, and then the transport between the vapor and particle phase, followed by fog chemistry when applicable.

### 3.1.11 Light Scattering

The next step in this visibility model is the calculation of light scattering and absorption by aerosol particles and gases. Additional skylight properties, such as sky color, skylight intensity, and scene appearance also can be calculated. To perform these calculations, it is necessary to estimate the refractive indices of the particles, and to know the particle size distribution. The number of particles of each size is known from the aerosol model results, and the refractive index is estimated from the predicted aerosol chemical composition (Stelson, 1990; Sloane, 1984b). The particle light scattering coefficient,  $b_{sp}$ , and particle light absorption coefficient,  $b_{ap}$ , next are calculated by integrating over the size distribution of the aerosol as in equation (3.11). Light scattering by air molecules is computed according to the data of Penndorf (1957). The  $\text{NO}_2$  concentration predicted by the model is used to compute light absorption by gases (Hodkinson, 1966). The computed light scattering and absorption by particles and gases is then summed in order to arrive at the total light extinction coefficient as a function of wavelength.

The particle light extinction coefficient is calculated from Mie theory, and sky color and skylight intensity can be calculated from the solution of the radiative transfer equation, as described by Sloane (1988) and as tested by

Eldering *et al.* (1993). An estimate of visual range can be calculated by applying Koschmieder's formula (Middleton, 1952) to the computed total extinction coefficient. This information also can be used to drive previously described image processing-based visibility models (Eldering *et al.*, 1993) that can produce synthetic color photographs of the appearance of the surrounding landscape as it would be seen from inside the air parcel in those cases where the visual range,  $L_v$ , is comparable to the dimensions of the air parcels tracked by a trajectory model (i.e., when  $L_v$  is less than or equal to several kilometers).

### 3.2 Model Application

As part of the Southern California Air Quality Study (SCAQS), a large cooperative air quality measurement program was carried out in the South Coast Air Basin of California to gather information to be used in the design and evaluation of air quality models (Lawson, 1990). Detailed measurements of gas- and particle-phase pollutant concentrations were made continuously over short averaging times during 11 intensive sampling days in the summer and six days in the fall of 1987. The gas-phase measurements included  $O_3$ ,  $NO$ ,  $NO_x$ ,  $SO_2$ ,  $NH_3$ ,  $HNO_3$  and detailed speciation of the volatile organic compounds present. Particulate matter was collected at nine sampling sites in two particle size ranges, those particles having diameters less than  $2.5 \mu m$  (PM<sub>2.5</sub>) and particles with diameters less than  $10 \mu m$  (PM<sub>10</sub>) using the SCAQS sampler designed by Fitz *et al.* (1989). Filter samples were collected over consecutive four to seven hour sampling periods and were analyzed for sulfate, nitrate, ammonium ion, chloride, sodium, organic carbon, elemental carbon, and 29 other elements including Fe, Mn, and V. In addition, ambient

aerosol size distribution and particle light scattering coefficient measurements were made using electrical aerosol analyzers (TSI model 3030) and optical particle counters (Particle Measuring Systems LAS-X) at 5 intensive monitoring sites (Eldering *et al.*, 1994). Continuous light scattering measurements were made at these sites using integrating nephelometers. Of the days represented by the SCAQS data base, the episode that occurred on August 27–28, 1987, was selected for the present visibility model evaluation effort. August 28 is the most polluted of the summer intensive sampling days and also experienced visibility that was among the lowest measured during the SCAQS sampling days. The August 27–28 SCAQS data base also contains detailed measurements of the size distribution of the sulfates, nitrates, organic carbon, elemental carbon and soil dust taken at Claremont, California, using cascade impactors by John *et al.* (1989) and by Zhang *et al.* (1993). Prior analysis of the chemical composition of filter samples and particle size distribution measurements made at Claremont on these days by electrical aerosol analyzers and optical particle counters have shown that data are available for model verification that are in reasonable agreement with the observed level of light scattering (Eldering *et al.*, 1994). For these reasons, air parcel trajectories terminating at Claremont will be studied here.

The meteorological data necessary to exercise the trajectory model for the August 27–28 SCAQS period were assembled by Harley *et al.* (1993), as part of an earlier study of photochemical smog formation. The input data required include hourly temperature, humidity, surface winds, mixing depths, total solar radiation, and ultraviolet radiation scaling factor fields. With the exception of mixing depths, these data were assembled from ground-based measurements followed by spatial interpolation using the objective analysis

techniques of Goodin *et al.* (1979). Mixing depths were determined from potential temperature analysis of SCAQS upper air soundings.

Air parcels were tracked over a period of two days, starting over the ocean and terminating at Claremont. Trajectories were computed using gridded hourly wind field data prepared by the methods of Goodin *et al.* (1979) by specifying the trajectory endpoint at Claremont and time of arrival and integrating backward in time. For this modeling work, 24 trajectories were used, one arriving at Claremont each hour of August 28. An example of one such trajectory is shown in Figure 3.2.

As noted by Wexler and Seinfeld (1991), aerosol  $\text{NH}_4\text{NO}_3$  predictions from the AIM gas/aerosol transport module vary depending on the choice of thermodynamic data for solid ammonium nitrate from among the values reported in the literature. In the present application, the thermodynamic data for  $\text{NH}_4\text{NO}_3$  reported by Parker *et al.*, (1976) are employed. That dataset has been used successfully in many applications to model aerosol  $\text{NH}_4\text{NO}_3$  concentrations in the Southern California atmosphere (Stelson and Seinfeld, 1982; Russell *et al.*, 1983; Hildemann *et al.*, 1984; Russell and Cass, 1986; Russell *et al.*, 1988).

### 3.2.1 Particulate Emissions Inventory

Day-specific emission inventories for August 27 and 28, 1987, provided by the California Air Resources Board (ARB) (Wagner and Allen, 1990) provide the starting point for our emissions processing procedures. This inventory includes spatially resolved total particle mass emissions rates for 455 separate source types present in Southern California. The largest contributors to these mass emissions, including motor vehicle exhaust and paved-road dust, were

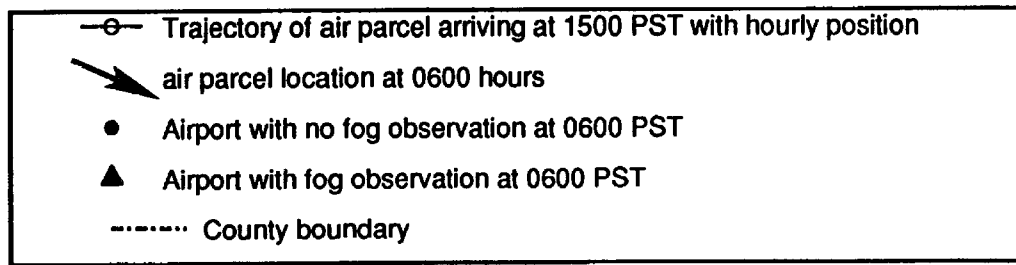
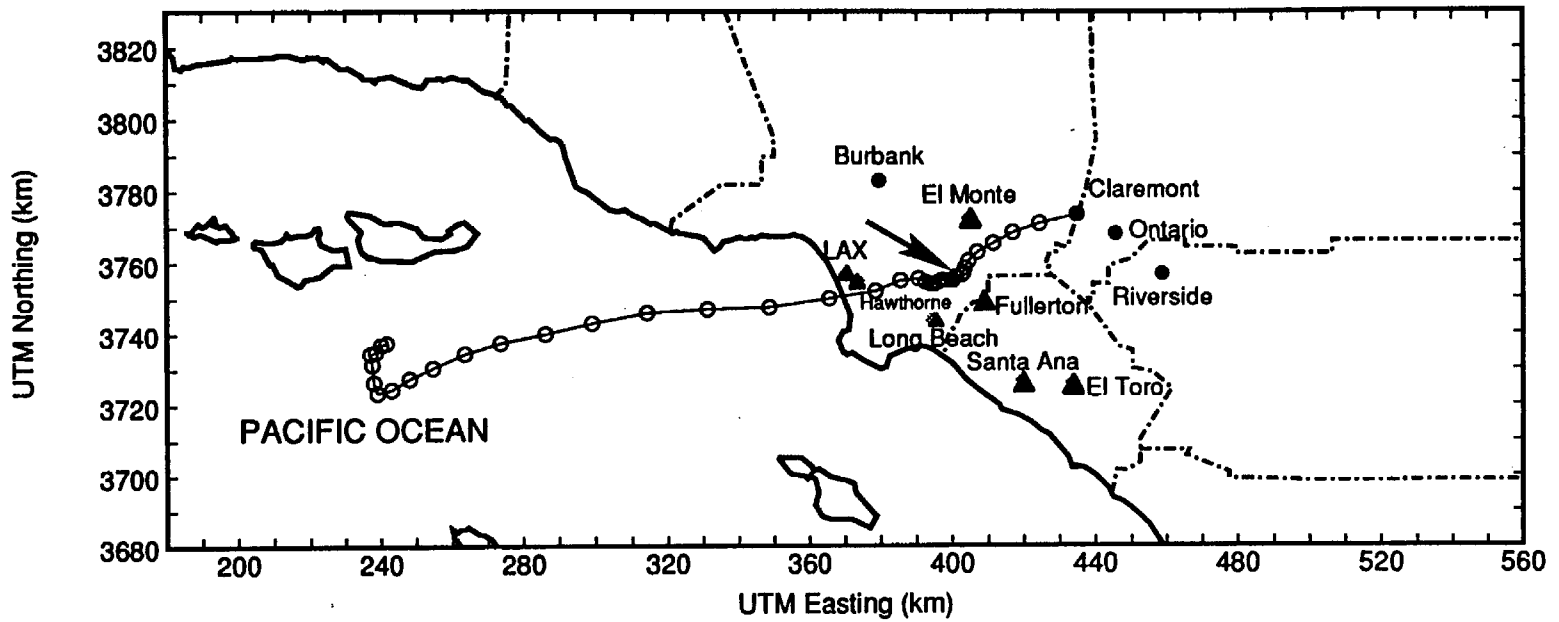


Figure 3.2: Path followed by the air parcel arriving at Claremont at 1500 PST on August 28, 1987. The circles along the trajectory path mark the location at each hour. The position of the air parcel at 0600 PST is shown by an arrow and the air parcel is seen to be surrounded by airports reporting fog at that time.

examined carefully and revised.

In the ARB inventory, on-road vehicle emissions, including catalyst-equipped autos and trucks, non-catalyst gasoline-powered vehicles, and diesel vehicles, are grouped together. To permit the use of more specific information on mass emission rates, particle chemical composition and particle size, these categories were separated for the current work. Estimates of the total mass emissions from on-road motor vehicles were constructed based on the approach of Gray (1986) and the source sampling experiments of Hildemann *et al.* (1991ab). The number of vehicle kilometers travelled within the South Coast Air Basin each day by vehicles of each type for an average day in 1987 were obtained from the 1991 revision of the South Coast Air Quality Management District's (SCAQMD) air quality management plan (Chang *et al.*, 1991). Particulate matter emission rates in grams per kilometer travelled were taken from those reported by Hildemann *et al.* (1991ab) and Gray (1986). Mass emission estimates were computed for catalyst-equipped light-duty autos, catalyst-equipped light-duty trucks, catalyst-equipped medium-duty trucks, catalyst-equipped heavy-duty trucks, motorcycles, non-catalyst light-duty autos, non-catalyst light-duty trucks, non-catalyst medium-duty trucks, non-catalyst heavy-duty trucks, diesel light-duty automobiles, diesel light-duty trucks, diesel heavy-duty trucks, diesel urban buses, and tire wear. The ARB motor vehicle emissions inventory was used only to provide the relative spatial and temporal distribution of the new estimates for total mass emission rates from on-road vehicles.

The ARB estimates for total mass emissions of paved-road dust and dust from construction and demolition activities were scaled to match more recent information from the South Coast Air Quality Management District and the

Midwest Research Institute (Englehart and Muleski, 1991). This resulted in a decrease in total mass emissions from both of these sources. Particulate mass emission rates from the remaining sources are as specified by the ARB.

The primary particle mass emission rate data next were passed to the emissions processing model created for use in the present study. The detailed size distribution data of Figure 3.1 and the corresponding chemical composition data of Hildemann *et al.* (1991a) were used to cast the emissions from the major sources that can be represented by those profiles into equivalent particle number counts and chemical composition in 15 discrete particle sizes from 0.01  $\mu\text{m}$  to 10  $\mu\text{m}$  particle diameter. The particle sizes are equally spaced on a log diameter scale with the initial diameters at the log center of each division. Of the particulate matter mass emissions, 90% are represented by the size-composition profiles of Figure 3.1.

For industrial sources not represented in Figure 3.1, specific chemical speciation information was sought from the South Coast Air Quality Management District's PM10 Source Composition Library (Cooper *et al.*, 1989) which represents source tests within the study area. Nineteen additional source chemical composition profiles were used to replace the ARB inventory's chemical composition information for a number of industrial sources. The data of Cooper *et al.* (1989) do not provide size distribution data, so the low resolution particle size data (i.e., particles  $\leq 1 \mu\text{m}$ , 1 - 2.5  $\mu\text{m}$ , 2.5 - 10  $\mu\text{m}$  particle diameter) assigned to similar sources in the ARB inventory were applied to these sources.

For the remaining sources, particle size and chemical composition data furnished by the ARB were used. The original ARB particulate matter emission inventory includes source chemical and size-specific information for four

particle size groups: diameters of less than 1  $\mu\text{m}$ , diameters from 1 to 2.5  $\mu\text{m}$ , diameters from 2.5 to 10  $\mu\text{m}$ , and diameters greater than 10  $\mu\text{m}$ . The ARB provided 67 particulate matter source profile codes, which use 50 different source chemical composition profiles. Many of the ARB source size and chemical composition descriptions originate from Taback *et al.* (1979). Some of the values coded into these profiles by the ARB can be improved with more recent information, or by correcting the coding of the original information. In Taback *et al.*'s report, the total carbon weight fraction reported represented both volatile organic carbon plus non-volatile elemental (black) carbon. In many instances in the ARB emission inventory, Taback *et al.*'s emissions information on the element carbon (i.e., total carbon) was coded as if it were elemental (black) carbon. In most cases, the elemental carbon mass emissions rates and size distribution data used in our present study come from Hildemann *et al.* (1991a) or Gray (1986). But in those cases where an ARB source composition profile is used, a check was made to correct the above mentioned coding error in the ARB data base.

Tables 3.2 and 3.3 highlight the large differences between the ARB emissions inventory and our revised primary particle emission inventory. The overall PM<sub>10</sub> mass emissions are reduced to 38% of the rate estimated by the ARB, and fine particle emissions within the revised inventory are 32% of the ARB-reported mass emissions. Analysis of the difference in PM<sub>10</sub> mass emissions for each chemical substance, by source category, between the ARB inventory and the revised inventory highlights the source categories that are responsible for most of the inventory differences. PM<sub>10</sub> primary sulfate emissions decrease by 89% due to a  $42 \times 10^3 \text{ kg day}^{-1}$  decrease in primary sulfate emissions from on-road motor vehicles plus a  $5 \times 10^3 \text{ kg day}^{-1}$  decrease in

Table 3.2: PM10 Emissions in the South Coast Air Basin  
 Day-Specific Inventory for August 27-28, 1987 <sup>a</sup>

| Species                      | ARB Inventory<br>(10 <sup>3</sup> kg/day) | Revised Inventory<br>(10 <sup>3</sup> kg/day) |
|------------------------------|---|---|
| Na <sup>+</sup>              | 2.7                                       | 1   |
| Cl <sup>-</sup>              | 15  | 1.6   |
| NH <sub>4</sub> <sup>+</sup> | 0.8                                       | 0.2   |
| NO <sub>3</sub> <sup>-</sup> | 2.3                                       | 2   |
| SO <sub>4</sub> <sup>=</sup> | 53  | 6   |
| Organic material             | 120                                       | 81  |
| Elemental Carbon (EC)        | 40  | 15  |
| Crustal material             |   | 331   |
| Metals-rich industrial       |   | 17  |
| Other identified             | 620                                       |   |
| Other unidentified           | 455                                       | 46  |
| Total                        | 1309                                      | 501   |

<sup>a</sup>For a discussion of these differences, see the text on pages 73, 76 and 77.

Table 3.3: PM<sub>2.5</sub> Emissions in the South Coast Air Basin  
Day-Specific Inventory for August 27-28, 1987

| Species                      | ARB Inventory<br>(10 <sup>3</sup> kg/day) | Revised Inventory<br>(10 <sup>3</sup> kg/day) |
|------------------------------|---|---|
| Na <sup>+</sup>              | 0.7                                       | 0.5   |
| Cl <sup>-</sup>              | 11  | 1.1   |
| NH <sub>4</sub> <sup>+</sup> | 0.7                                       | 0.2   |
| NO <sub>3</sub> <sup>-</sup> | 1.4                                       | 1.1   |
| SO <sub>4</sub> <sup>=</sup> | 49  | 4   |
| Organic material             | 40  | 48  |
| Elemental Carbon (EC)        | 33  | 13  |
| Crustal material             |   | 68  |
| Metals-rich industrial       |   | 16  |
| Other identified             | 250                                       |   |
| Other unidentified           | 134                                       | 15  |
| Total                        | 520                                       | 167   |

the mass of PM10 primary sulfate emissions from other sources. This is a very important change because the excess primary sulfate emissions in the ARB inventory could have masked an underprediction of secondary sulfate production by the air quality model. (The ARB primary sulfate emissions were incorrect in part because they assigned Taback *et al.*'s source test of an internal combustion engine burning sewage-treatment plant digester gas to represent the emissions from gasoline-fueled internal combustion engines and engines burning landfill or process gas.) PM10 elemental carbon (EC) emissions decrease by 62% through a combination of a  $12 \times 10^3$  kg day<sup>-1</sup> decrease in the emissions from on-road vehicles relative to the ARB inventory, a  $6.6 \times 10^3$  kg day<sup>-1</sup> decrease in PM10 EC emissions from paved-road dust, and smaller decreases in PM10 EC emissions from a number of other sources. The excessive elemental carbon emissions present in the original ARB emissions inventory would be particularly damaging to a visibility modeling study due to the high light absorption efficiency of black elemental carbon. Primary organic carbon particle emissions decreased overall by 32% relative to the ARB inventory, through a combination of increases in some source categories and decreases in others. PM10 organic carbon emitted from the paved-road dust category was reduced by  $66 \times 10^3$  kg day<sup>-1</sup> in the revised inventory when compared to the ARB inventory, while organic compounds emitted from on-road vehicles increased by  $14 \times 10^3$  kg day<sup>-1</sup>. A change in the chemical composition of emissions from commercial charbroiling and frying increased organics emissions from those sources by  $15 \times 10^3$  kg day<sup>-1</sup> relative to the ARB inventory. The soil-like material in the revised inventory can be compared to the "other identified species" of the ARB inventory; the reduction in the emissions of these materials is primarily a result of the decrease in total mass

emissions from the paved-road dust and construction and demolition dust source categories. A highly aggregated summary of the emission inventory for August 28 is presented in Table 3.4.

A comparison of the size distribution and chemical composition of the revised inventory versus the ARB inventory is presented in Figure 3.3. The ARB inventory does not actually specify a lower limit for their particle size distribution in the submicron range. Here we graph the ARB emissions as if the submicron particles are principally in the size range from 0.1 to 1.0  $\mu\text{m}$  particle diameter.

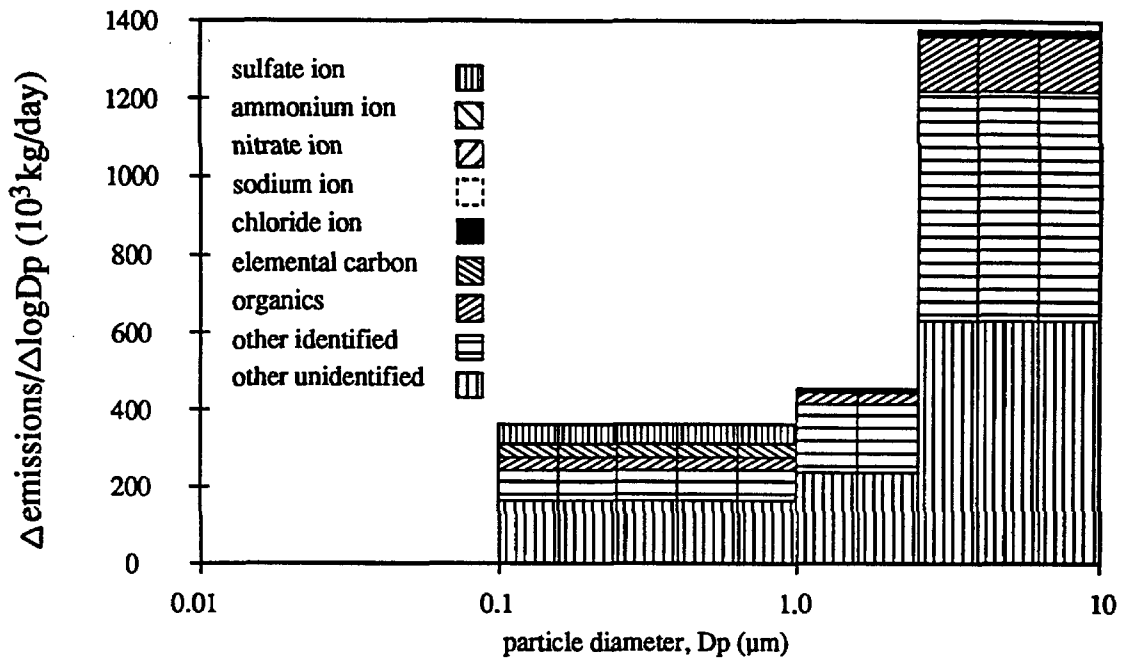
### 3.2.2 Gas-phase Emission Inventory

Preparation of the gas-phase emission inventory for NO, NO<sub>2</sub>, CO, and volatile organic compounds (VOC) begins with the SCAQS day-specific emissions files for August 27–28 prepared by the California Air Resources Board (Wagner and Allen, 1990). Motor vehicle exhaust measurements made in a highway tunnel during the SCAQS field study (Ingalls, 1989) have shown that the emissions of organic gases and carbon monoxide from motor vehicles in Los Angeles are significantly higher than suggested by the EMFAC7E motor vehicle emissions model used by the ARB to prepare the SCAQS inventory (Pierson *et al.*, 1990; Ingalls, 1989). Through analysis of the tunnel study data, Harley *et al.* (1993) report that the carbon monoxide and organic gas hot exhaust emissions from on-road vehicles should be increased to three times the official inventory levels, and this correction has been made in the present study as it has been in previous photochemical modeling studies of the SCAQS smog episodes by Harley *et al.* (1993). The revised VOC mass emission inventory next was divided between 414 individual organic species

Table 3.4: Source-Specific PM10 Emissions for the South Coast Air Basin

| Day-Specific Revised Inventory for August 27-28, 1987 |                                  |                                   |                                 |
|---|----------------------------------|-----------------------------------|---------------------------------|
| source type   | PM10<br>(10 <sup>3</sup> kg/day) | PM2.5<br>(10 <sup>3</sup> kg/day) | PM1<br>(10 <sup>3</sup> kg/day) |
| fuel combustion                                       | 8.61                             | 8.56                              | 8.50                            |
| waste burning   | 0.04                             | 0.04                              | 0.03                            |
| solvent use   | 1.78                             | 1.51                              | 1.34                            |
| petroleum processing, storage                         | 2.08                             | 1.77                              | 1.41                            |
| industrial processes                                  |                                  |                                   |                                 |
| chemical  | 0.11                             | 0.10                              | 0.10                            |
| food and agriculture                                  | 24.24                            | 24.15                             | 23.24                           |
| mineral processing                                    | 0.61                             | 0.41                              | 0.22                            |
| metal processing                                      | 0.88                             | 0.84                              | 0.80                            |
| wood and paper  | 4.57                             | 2.12                              | 1.07                            |
| other   | 0.15                             | 0.12                              | 0.11                            |
| miscellaneous processes                               |                                  |                                   |                                 |
| farming operations                                    | 35.74                            | 4.77                              | 3.59                            |
| construction and demolition                           | 121.68                           | 26.63                             | 12.29                           |
| paved-road dust                                       | 147.13                           | 27.47                             | 12.67                           |
| unpaved-road dust                                     | 47.39                            | 10.35                             | 4.77                            |
| waste disposal  | 0.39                             | 0.37                              | 0.36                            |
| natural sources                                       | 65.98                            | 19.91                             | 9.19                            |
| mobile sources  |                                  |                                   |                                 |
| catalyst-equipped vehicles                            | 3.38                             | 3.30                              | 3.27                            |
| non-catalyst vehicles                                 | 7.86                             | 5.64                              | 4.77                            |
| diesel vehicles                                       | 14.07                            | 13.37                             | 12.80                           |
| off road vehicles                                     | 0.75                             | 0.70                              | 0.67                            |
| trains  | 0.61                             | 0.58                              | 0.55                            |
| ships   | 2.03                             | 1.94                              | 1.86                            |
| aircraft  | 3.09                             | 3.07                              | 3.05                            |
| mobile and utility equipment                          | 7.65                             | 7.13                              | 6.79                            |
| <b>Total</b>  | <b>500.82</b>                    | <b>164.85</b>                     | <b>113.45</b>                   |

## ARB Emissions Inventory, August 27-28, 1987



## Revised Emissions, August 27-28, 1987

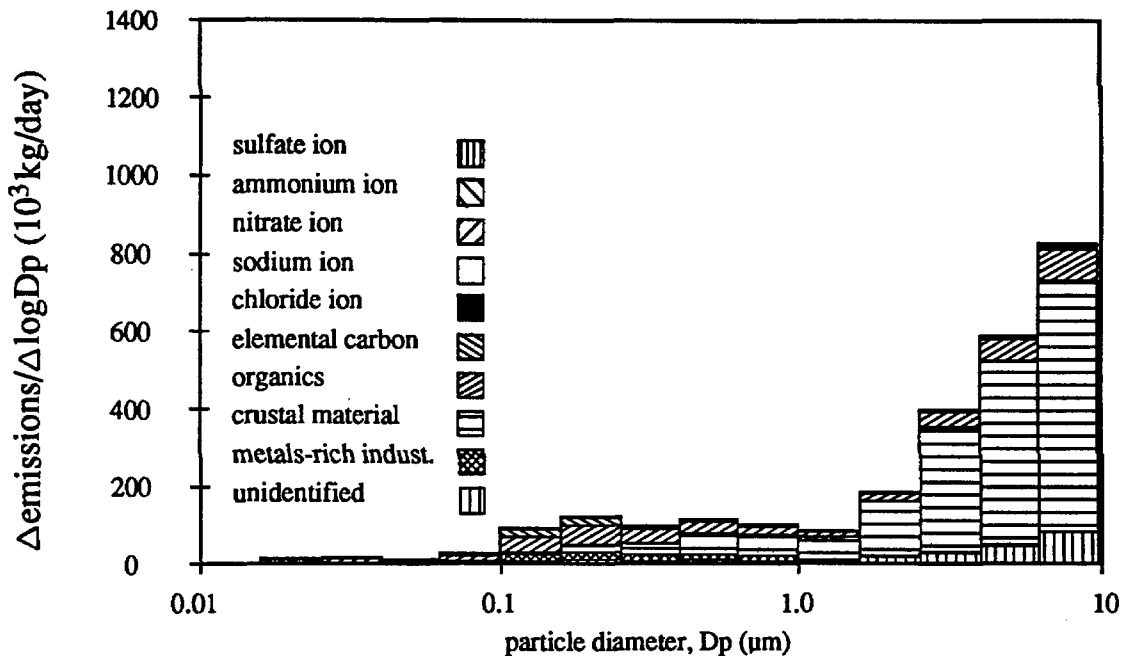


Figure 3.3: The size distribution and chemical composition of particulate matter emissions within the Southern California area mapped in Figure 3.2: (a) official State of California Air Resources Board (ARB) emission inventory, compared to (b) emissions estimated in the present study.

according to the source-specific VOC speciation procedures of Harley *et al.* (1992) that are built into our emissions model. These VOC species then were lumped into the 28 organic classes required for secondary organic aerosol formation calculations by the procedure of Pandis *et al.* (1992a) (3 lumped alkanes, ethene, 3 lumped alkenes, lumped alcohol, toluene, acetylene, 3 lumped aromatics, formaldehyde, isoprene, acetone, lumped ketone, benzene,  $\alpha$ -pinene, acetaldehyde, lumped aldehyde,  $\beta$ -pinene, heptene, octene, nonene, and benzaldehyde).

The 1982 spatially and temporally resolved ammonia emission inventory for the South Coast Air Basin prepared by Gharib and Cass (1984) was used to represent  $\text{NH}_3$  emissions within the present study. That inventory, including the contributions of the various sources and the resultant spatial distribution of  $\text{NH}_3$  emissions, has been published previously by Russell and Cass (1986). Russell and Cass (1986) presented aerosol nitrate formation calculations showing good agreement between measured and predicted ammonia and ammonium nitrate levels obtained using an earlier version of the present photochemical trajectory model combined with the 1982  $\text{NH}_3$  emission inventory. A revised ammonia inventory which is being prepared as part of the SCAQS study has not yet been released by its sponsor for inclusion in the present work.

### 3.2.3 Initial Conditions

Initial conditions for particulate matter were specified according to filter-based measurements of aerosol chemistry made using the SCAQS sampler at San Nicolas Island during SCAQS plus impactor-based, chemically-specific size distribution measurements made near the coast by John *et al.* (1989)

at Long Beach, California, during SCAQS. The filter-based measurements at San Nicolas Island were used to specify the initial concentration of major ionic species in the aerosol, while the shape of the initial size distribution was estimated from the impactor-based measurements. Initial concentrations of the various aerosol chemical species are given in Table 3.5, and the size distribution of the chemical composition of the initial aerosol inserted into each air parcel over the ocean upwind of the air basin is shown in Figure 3.4.

Initial conditions for gaseous air pollutants also are given in Table 3.5 based on air quality measurements made at San Nicolas Island and by aircraft flights over the ocean during SCAQS. Gaseous pollutant initial conditions are substantially the same as the upwind boundary conditions used previously for modeling the SCAQS August episode by Harley *et al.* (1993) and by Pandis *et al.* (1992a).

### 3.2.4 Mapping the Occurrence of Fog

Surveys of meteorological conditions that accompany high sulfate episodes in the Los Angeles area show that virtually all days of record with sulfate concentrations exceeding  $25 \mu\text{g m}^{-3}$  are days where fog is reported at coastal airports (Cass, 1976; 1979). Examination of the size distribution of the aerosol measured at Claremont during SCAQS using electrical aerosol analyzers (TSI model 3030) and optical particle counters (Eldering *et al.*, 1994) shows a very pronounced peak in the size distribution on August 27 and 28 at a particle diameter of approximately  $0.7 \mu\text{m}$ , a phenomenon generally associated with heterogeneous sulfate formation within liquid water drops (Hering and Friedlander, 1982; McMurry and Wilson, 1983; Meng and Se-

Table 3.5: Initial Conditions

| Gas-phase<br>species | Concentration<br>(ppb) | Aerosol<br>species           | Concentration<br>( $\mu\text{g m}^{-3}$ ) |
|----------------------|------------------------|------------------------------|---|
| CO                   | 113                    | Cl <sup>-</sup>              | 3   |
| NO                   | 5                      | Na <sup>+</sup>              | 2   |
| NO <sub>2</sub>      | 5                      | NO <sub>3</sub> <sup>-</sup> | 1   |
| O <sub>3</sub>       | 40                     | NH <sub>4</sub> <sup>+</sup> | 1.4                                       |
| methyl ethyl ketone  | 11                     | SO <sub>4</sub> <sup>-</sup> | 3   |
| formaldehyde         | 3.8                    | EC                           | 0.3                                       |
| acetaldehyde         | 3.5                    | OC                           | 1   |

## INITIAL CONDITIONS

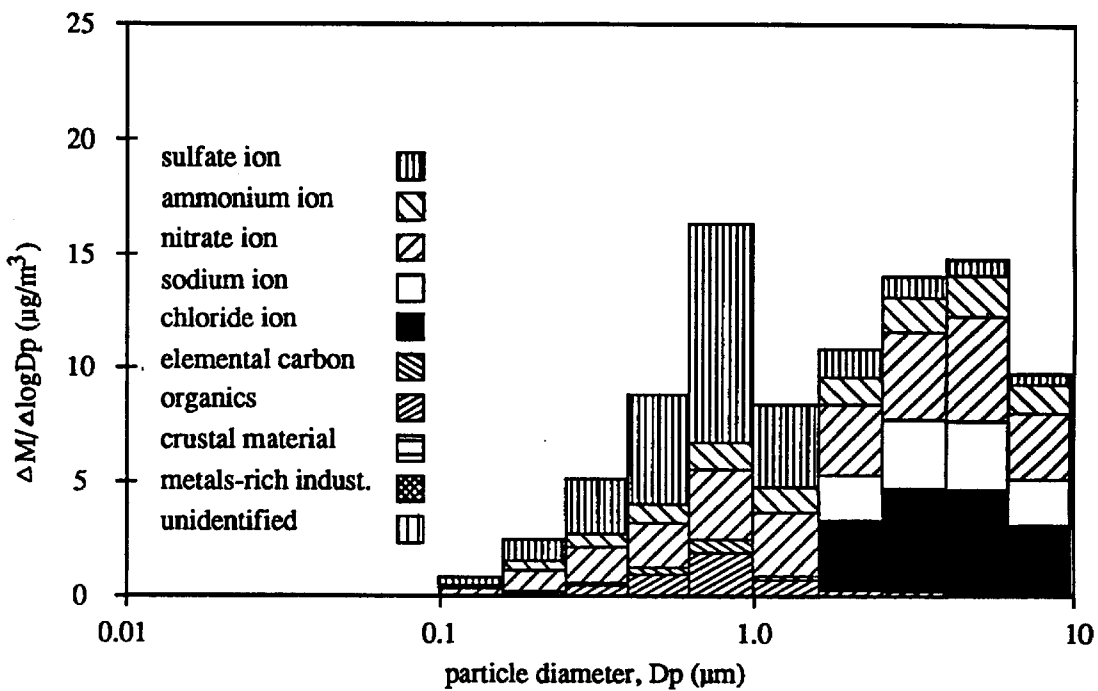


Figure 3.4: Aerosol mass distribution,  $\Delta M / \Delta \log D_p$ , describing initial conditions for particulate matter as a function of particle diameter,  $D_p$ , and chemical composition.

infeld, 1994). Therefore, a careful check was made of the Federal Aviation Administration (FAA) fog observations taken at airports located between Claremont and the coast on August 27 and 28 to see whether or not fog was reported along the path followed by the air parcel trajectories.

This survey revealed at least three fog events of possible importance on the night of August 27–28. Trajectories arriving at Claremont between 0400–1100 hours PST on August 28 stagnated overnight very near Claremont. The nearest airport to Claremont is at Ontario, 10 kilometers to the southeast; fog was reported at Ontario International Airport both at 0250 hours and 0355 hours PST that night. A second, widely reported fog event occurred throughout the Central Los Angeles basin. This fog was first reported at Los Angeles International Airport at 0000 hours and eventually grew until it was reported at seven airports simultaneously by 0600 hours on August 28, as shown in Figure 3.2. That fog later dissipated with its last report at Hawthorne at 1000 hours that day. Trajectories arriving at Claremont between 1200 and 1700 hours PST on August 28 clearly spent several hours over land within that fog. An example of one trajectory's location relative to that fog at 0600 hours on August 28 is shown in Figure 3.2. Finally, trajectories arriving at Claremont between 1800 and 2400 hours PST on August 28 stagnated overnight over the ocean but near the coast within Santa Monica Bay at a time when fog was reported at coastal airports. SO<sub>2</sub> emissions occur in that region and within our model due to ships in the offshore shipping lanes. Whether or not these parcels that stagnated over Santa Monica Bay were engulfed in fog overnight is not known for sure, but it seems likely.

An objective procedure was adopted for determining when an air parcel

enters or exits one of these fogs within our air quality model. The FAA fog reports from all airports located upwind of Claremont were gathered for August 27 and 28. A separate map was prepared for each hour of those two days on which each airport was coded as reporting fog, reporting no fog, or not reporting data at all (i.e., closed to operations). A mark was made on each map at half the distance between those airports reporting fog and adjacent airports reporting no fog. Contour lines then were drawn to enclose the airports reporting fog by connecting the marks made at half the distance to sites reporting no fog. An air parcel then was determined to encounter the fog when it crossed into the boundary of one of these fog zones, and the fog was assumed to dissipate within that air parcel when the parcel later exited the fog zone boundary, either because the fog zone has been reduced in size at a later hour or because the air parcel has been advected out of the fog zone.

One inconsistency in the SCAQS data base merits attention at this point. The relative humidity (RH) values obtained by interpolation to the location of the air parcel trajectories typically are well below 100% RH at the time that fogs were reported. Nevertheless, the FAA observers distinguish between haze and smoke (i.e., smog) and a true fog, and fogs were so widely reported by independent observers that the fog occurrence cannot be dismissed. RH data supplied by inexpensive or older sensors are notoriously inaccurate, so perhaps the RH data are incorrect. Alternatively, the interpolation procedures used here to create RH fields do not distinguish locations reporting fogs from drier locations so that RH data from non-fog drier locations are combined during spatial interpolation with data from sites where fog was observed, possibly masking the highest relative humidities encountered. To

explore the possible effect of variations in the extent of the fogs, two test cases will be examined using the visibility model: (1) fog is considered to occur at all times when an air parcel is within a reported fog (basecase assumption), and (2) fog is only considered to occur when fog is reported and the relative humidity interpolated to the interior of the air parcel is above 70%.

### 3.2.5 Fog Calculations

The fog chemical model employed here requires that pH values and Fe(III) and Mn(II) metals concentrations be known. The atmospheric total iron and manganese concentrations were measured during the SCAQS experiment, but the valence state of these metals is not known. However, fog water samples in the Los Angeles area have been examined on other occasions by Erel *et al.*, (1993). Their data show that on average 49% of the atmospheric iron in fog water typically is present as Fe(III) in unfiltered fogs and cloudwater samples collected in the Los Angeles basin. Therefore, the Fe(III) and Mn(II) concentrations in the fog were set by first consulting the filter-based measurements of total Fe and total Mn in fine particles in the SCAQS network filter samples closest in time and space to the place where each trajectory enters a fog zone, and then assuming that 49% of the Fe was present as Fe(III) and that 49% of the Mn was present as Mn(II). Likewise, fog pH cannot be calculated reliably from the SCAQS database as we do not know precisely how much alkaline material may have been present in the particle-phase that would affect pH upon its dissolution. The pH of fogs in the Los Angeles area also has been examined extensively by Erel *et al.* (1993), Jacob *et al.* (1985), Munger *et al.* (1983), and Waldman (1985). Their data show that fog pH falls in the

range of 2.22 to 5.25. A central value of pH 4.0 is adopted for use in our basecase calculations, and the sensitivity of model calculations to variations in pH will be explored. Aerosol particles are activated in accordance with an assumed water vapor supersaturation of 0.08% and grow to an assumed 20  $\mu\text{m}$  diameter while in the fog. When the fog dissipates, the water content of each droplet is reduced to that of an aerosol particle containing small amounts of water, then the AIM inorganic species transport code is used to redistribute volatile pollutant species and water vapor between the gas and particle phases at the relative humidity observed after the fog has dissipated.

### **3.3 Model Results**

The emissions and meteorological data were assembled for use in the trajectory-based visibility model. Aerosol concentration, size distribution, chemical composition, and light scattering by particles then were computed for each of 24 trajectories of 48 hour duration arriving hourly at Claremont on August 28, 1987. The basecase calculations presented first represent results obtained for the case with fog calculations invoked at all hours when fog was reported by human observers at area airports. Results are presented for important gas-phase species, aerosol mass concentrations and the concentration of individual aerosol components, as well as the size distribution of important aerosol chemical species, overall aerosol size distributions, particle light scattering calculations, and visual range predictions.

#### **3.3.1 Gas-phase Species**

Figure 3.5 shows time series plots of predicted and measured ozone, as a measure of the level of the gas-phase photochemistry, and  $\text{NO}_2$ , an important

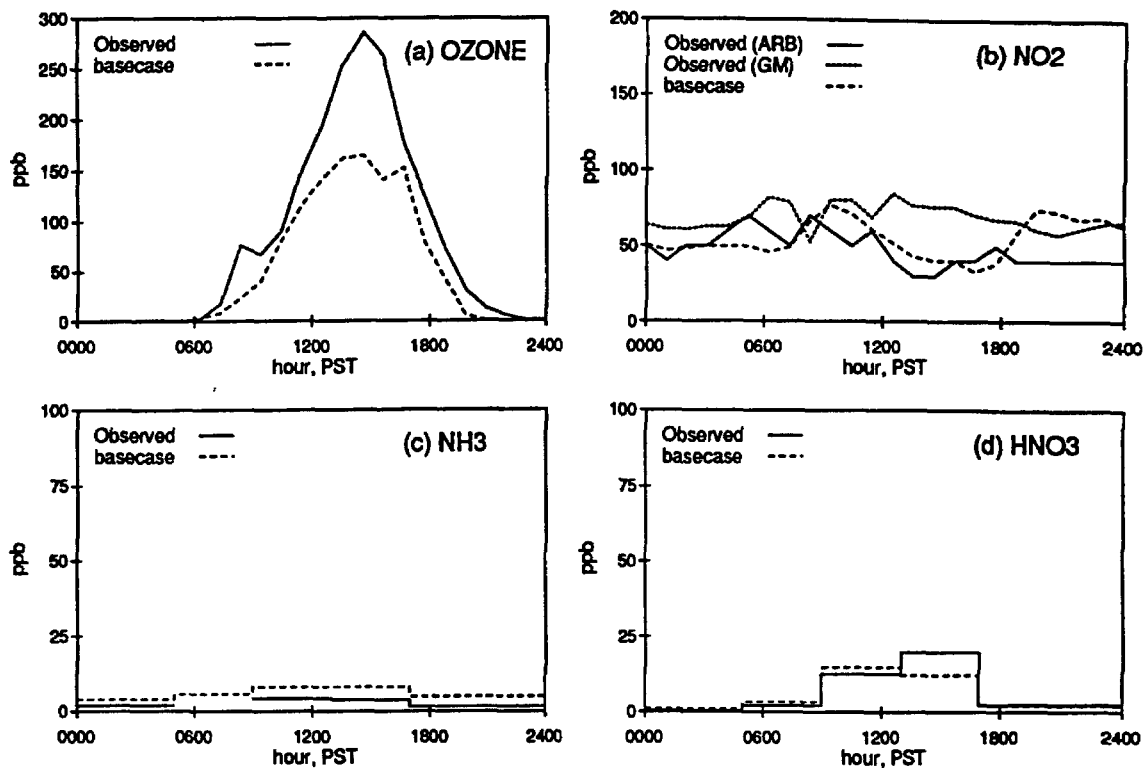


Figure 3.5: Time series plots of observed and predicted gas-phase pollutant concentrations on August 28, 1987, at Claremont, California: (a) O<sub>3</sub>, (b) NO<sub>2</sub>, (c) NH<sub>3</sub>, and (d) HNO<sub>3</sub>.

ozone precursor and light absorbing gas. Time series plots of ammonia and nitric acid are also presented, as they play an important role in secondary inorganic aerosol formation. The ozone predictions fall below the observed values at Claremont, a result that is substantially identical to previous model results obtained for ozone at Claremont during the SCAQS August 27–28 episode (Harley *et al.*, 1993) even when modeled ozone concentrations at other sites in the air basin generally are in quite close agreement with observed values. The role of ozone and other photochemical oxidants in the present visibility model is to assist the heterogeneous oxidation of  $\text{SO}_2$  to form sulfates in fog droplets. It will be seen shortly that in spite of the underprediction of ozone levels, oxidant concentrations are still high enough to convert virtually all of the available  $\text{SO}_2$  to form sulfates when a fog occurs in the higher pH sensitivity tests. Therefore, the underprediction of the ozone concentrations does not greatly affect the present visibility model. The model predictions for  $\text{NO}_2$  fall in the middle of the range of values reported by two co-located  $\text{NO}_2$  monitors at Claremont with some overprediction during nighttime periods. Gaseous nitric acid predictions are in good agreement with measurements made over consecutive 4 to 7 hour sampling periods using the denuder difference system for  $\text{HNO}_3$  built into the SCAQS sampler (Fitz *et al.*, 1989; Hering *et al.*, 1988; Solomon *et al.*, 1988). Both observed and predicted gaseous ammonia concentrations are on the order of a few ppb.

### 3.3.2 Aerosol Mass Concentration

Time series plots of the observed and predicted  $\text{PM}_{2.5}$  and  $\text{PM}_{10}$  aerosol mass concentration for the base case are shown in Figure 3.6 (a) and (b). These measurements of aerosol mass concentration were made by filtration

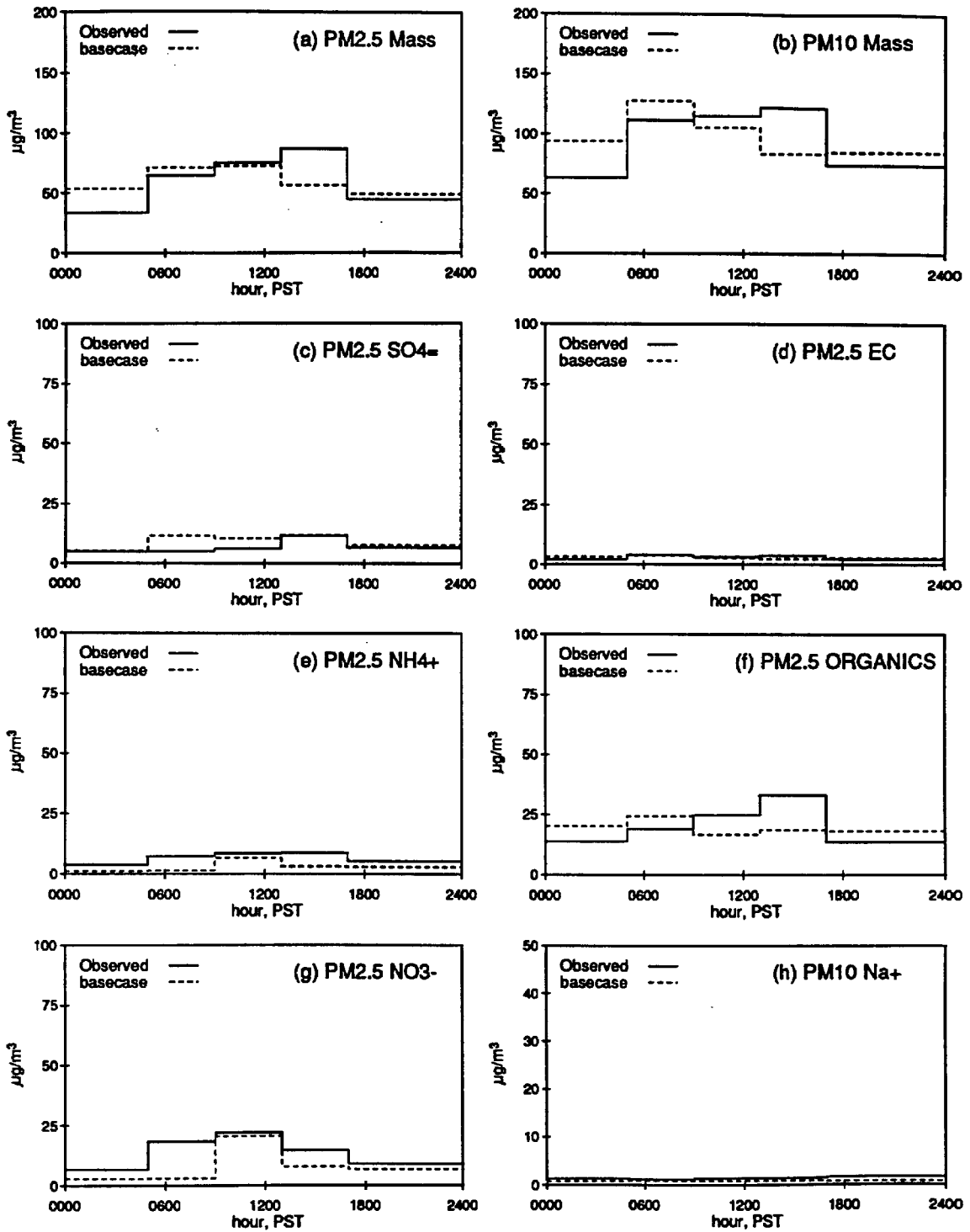


Figure 3.6: Time series plots of observed and predicted particle-phase concentrations on August 28, 1987, at Claremont, California: (a) PM<sub>2.5</sub> mass, (b) PM<sub>10</sub> mass, (c) PM<sub>2.5</sub> SO<sub>4</sub><sup>=</sup>, (d) PM<sub>2.5</sub> elemental carbon (EC) (e) PM<sub>2.5</sub> NH<sub>4</sub><sup>+</sup>, (f) PM<sub>2.5</sub> organics, (g) PM<sub>2.5</sub> NO<sub>3</sub><sup>-</sup>, (h) PM<sub>10</sub> Na<sup>+</sup>.

using the SCAQs sampler over 4 to 7 hour periods. Model results are averaged over the same 4 to 7 hour time periods while grouping all particles in the model having diameters less than  $2.5 \mu\text{m}$  and less than  $10 \mu\text{m}$ . The mean of the five measured PM<sub>2.5</sub> concentrations shown in Figure 3.6(a) is  $61 \mu\text{g m}^{-3}$  while the corresponding predicted PM<sub>2.5</sub> concentration from the model is  $59 \mu\text{g m}^{-3}$ . The mean of the five measured PM<sub>10</sub> concentrations is  $97 \mu\text{g m}^{-3}$  while the corresponding predicted PM<sub>10</sub> concentration from the model is  $97 \mu\text{g m}^{-3}$ . The mass present in the PM<sub>10</sub> and PM<sub>2.5</sub> size fractions oscillates about the observed values with modeled values greater than or equal to observations in 3 time periods and model predictions lower than observations in 2 time periods. A statistical summary of the comparison between model predictions and observations for the basecase simulation is given in the first rows of Table 3.6.

### 3.3.3 Individual Aerosol Species

Figures 3.6(c) through (h) show time series plots of observations and model predictions of the PM<sub>2.5</sub> or PM<sub>10</sub> aerosol mass concentration of important individual chemical species. Again, the measured values are from the SCAQS filter-based sampler located at Claremont. The fine particle  $\text{NO}_3^-$  data are taken by the denuder difference method in order to avoid sampling artifacts, and the  $\text{NH}_4^+$  data have been corrected to the same basis as the nitrate data (see Eldering *et al.*, 1994). The time series for elemental carbon is shown in Figure 3.6d. Elemental carbon is not produced by any secondary atmospheric chemical reactions and it is not removed from the atmosphere easily by dry deposition due to the size of the particles. There is excellent agreement between the observations and predictions for elemental carbon suggesting that

Table 3.6: Analysis of Model Performance

| case              | PM2.5 Mass<br>[mean] <sup>a</sup><br>bias <sup>b</sup><br>(std dev) <sup>c</sup> | PM10 Mass                     | EC<br>(PM2.5)               | organics<br>(PM2.5)          | SO <sub>4</sub> <sup>=</sup><br>(PM2.5) | NH <sub>4</sub> <sup>+</sup><br>(PM2.5) | NO <sub>3</sub> <sup>-</sup><br>(PM2.5) | Na <sup>+</sup><br>(PM10)   |
|-------------------|--|-------------------------------|-----------------------------|------------------------------|---|---|---|-----------------------------|
| observed<br>mean  | [ 60.90]   | [ 97.04]                      | [ 3.19]                     | [ 20.99]                     | [ 7.16]                                 | [ 6.79]                                 | [ 14.22]                                | [ 1.46]                     |
| basecase<br>model | [ 59.08]<br>-1.82<br>( 16.43)  | [ 96.66]<br>-0.38<br>( 23.05) | [ 3.09]<br>-0.10<br>( 0.96) | [ 20.14]<br>-0.85<br>( 7.93) | [ 10.12]<br>2.96<br>( 2.89)             | [ 2.64]<br>-4.14<br>( 1.74)             | [ 6.22]<br>-8.00<br>( 4.64)             | [ 0.87]<br>-0.59<br>( 0.28) |
| lower pH          | [ 55.24]<br>-5.66<br>( 18.95)  | [ 92.82]<br>-4.22<br>( 25.35) | [ 3.09]<br>-0.10<br>( 0.96) | [ 20.14]<br>-0.85<br>( 7.93) | [ 6.21]<br>-0.95<br>( 1.49)             | [ 2.66]<br>-4.12<br>( 1.75)             | [ 6.22]<br>-8.00<br>( 4.66)             | [ 0.87]<br>-0.59<br>( 0.28) |
| higher pH         | [ 63.72]<br>2.82<br>( 13.26)   | [101.32]<br>4.28<br>( 20.04)  | [ 3.09]<br>-0.10<br>( 0.96) | [ 20.16]<br>-0.83<br>( 7.94) | [ 14.76]<br>7.60<br>( 6.77)             | [ 2.61]<br>-4.17<br>( 1.74)             | [ 6.28]<br>-7.94<br>( 4.59)             | [ 0.87]<br>-0.59<br>( 0.28) |
| less fog          | [ 57.06]<br>-3.84<br>( 16.16)  | [ 95.34]<br>-1.70<br>( 22.84) | [ 3.10]<br>-0.09<br>( 0.96) | [ 20.22]<br>-0.77<br>( 8.02) | [ 7.68]<br>0.52<br>( 2.42)              | [ 2.61]<br>-4.18<br>( 1.73)             | [ 6.38]<br>-7.84<br>( 4.87)             | [ 0.88]<br>-0.58<br>( 0.28) |

<sup>a</sup>unweighted mean of 5 pairs of predictions and observations corresponding to the 5 sampling intervals shown in Figures 6 and 7; all values in  $\mu\text{g m}^{-3}$

<sup>b</sup>predicted - observed,  $\mu\text{g m}^{-3}$

<sup>c</sup>standard error of residuals,  $\mu\text{g m}^{-3}$

transport calculations for fine particles are working well. Organic material is a combination of primary material and secondary organic aerosols. The model predictions of PM<sub>2.5</sub> organic material concentrations (Figure 3.6f) are in close agreement with observations with mean daily predicted concentrations for the basecase of  $20 \mu\text{g m}^{-3}$  versus a measured concentration of  $21 \mu\text{g m}^{-3}$ , as shown in Table 3.6. Overprediction occurs in three sampling periods and underprediction in two sampling periods.

Aerosol sulfate is both emitted as a primary aerosol constituent and is produced through the oxidation of  $\text{SO}_2$  in the atmosphere. There is excellent agreement between observations and basecase model predictions for aerosol sulfate during three sampling periods, with small overprediction of sulfate concentrations during two sampling periods.

Sensitivity analysis using the model show that predicted sulfate ion mass concentrations are most strongly affected by the number of hours that a trajectory is within a fog and the pH of the fog droplet. Figure 3.7 shows predicted PM<sub>2.5</sub> sulfate concentrations for three sensitivity tests. In Figure 3.7(a) the observed PM<sub>2.5</sub> sulfate concentrations are compared to model results at higher and at lower pH values (pH 4.5 and pH 3.5, respectively). Also presented in Figure 3.7(b) are results for pH 4 with fog invoked only when both fog was reported by FAA observers and the RH interpolated to the interior of the trajectory cell was greater than 70% ("less fog"). Model predictions of daily average sulfate concentrations vary by  $\pm 4$  to  $4.6 \mu\text{g m}^{-3}$  as the pH is varied, decreasing with decreasing pH. The simulation using less extensive fogs ("less fog") results in a noticeable decrease in predicted PM<sub>2.5</sub> sulfate concentrations during the second sampling period of the day (0500–0900), a slight decrease in predictions during the third sampling period

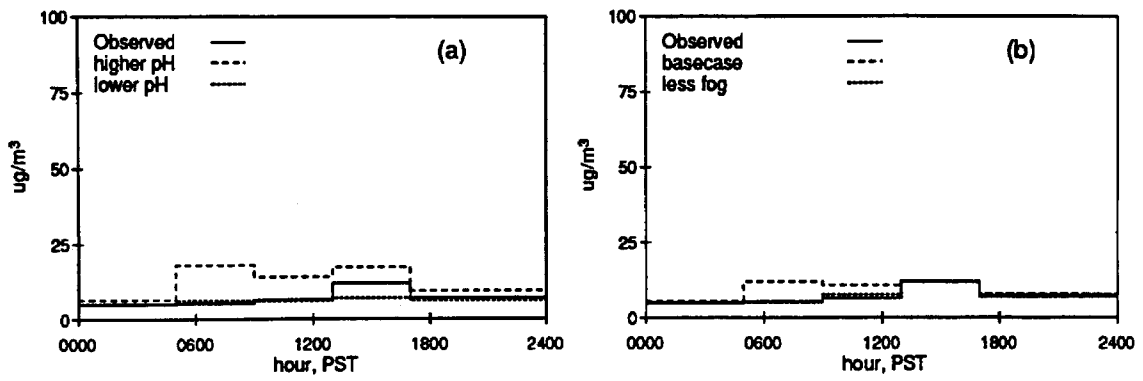


Figure 3.7: Time series plots of observed and predicted PM<sub>2.5</sub> SO<sub>4</sub><sup>2-</sup> concentrations: basecase model compared to all sensitivity tests.

(0900–1300), and no change in the predictions for the other sampling periods and yields excellent agreement between predicted and observed sulfate concentrations. A statistical summary of model performance for the case of each sensitivity test also is given in Table 3.6.

Model predictions of PM<sub>2.5</sub> NO<sub>3</sub><sup>-</sup> concentrations are controlled by the total amount of inorganic nitrate ever produced within the air parcel, by the gas-phase concentrations of ammonia, and by the amount of Na<sup>+</sup> from sea salt available to form coarse particle nitrates. Figure 3.6(h) and Table 3.6 show that the PM<sub>10</sub> Na<sup>+</sup> concentration is reproduced to within about 0.5 μg m<sup>-3</sup>. Figure 3.5 shows that gas-phase NH<sub>3</sub> concentrations predicted by the model are a little higher than observed values. Model predictions for aerosol nitrate shown in Figure 3.6(e) fall substantially below observed values during the second sampling period and somewhat below observations at other times. This underprediction of aerosol nitrate is due in part to the slight underprediction of Na<sup>+</sup> levels and in part to a shortage of total inorganic nitrate (i.e., HNO<sub>3</sub> ever produced by the model).

### 3.3.4 Comparison with Impactor Measurements

Figures 3.8 and 3.9 show comparisons of size-distributed aerosol species concentrations and model predictions. Impactor measurements of the size-distributed aerosol concentrations of sodium, nitrate, ammonium, and sulfate ion were made by John *et al.* (1989) with nine-stage Berner impactors at Claremont during SCAQS. Zhang *et al.* (1993) used microorifice uniform deposit impactors (MOUDIs) to measure organic and elemental carbon particle size distributions at Claremont during SCAQS. Both sets of impactor measurements were made over the same sampling periods as the SCAQS fil-

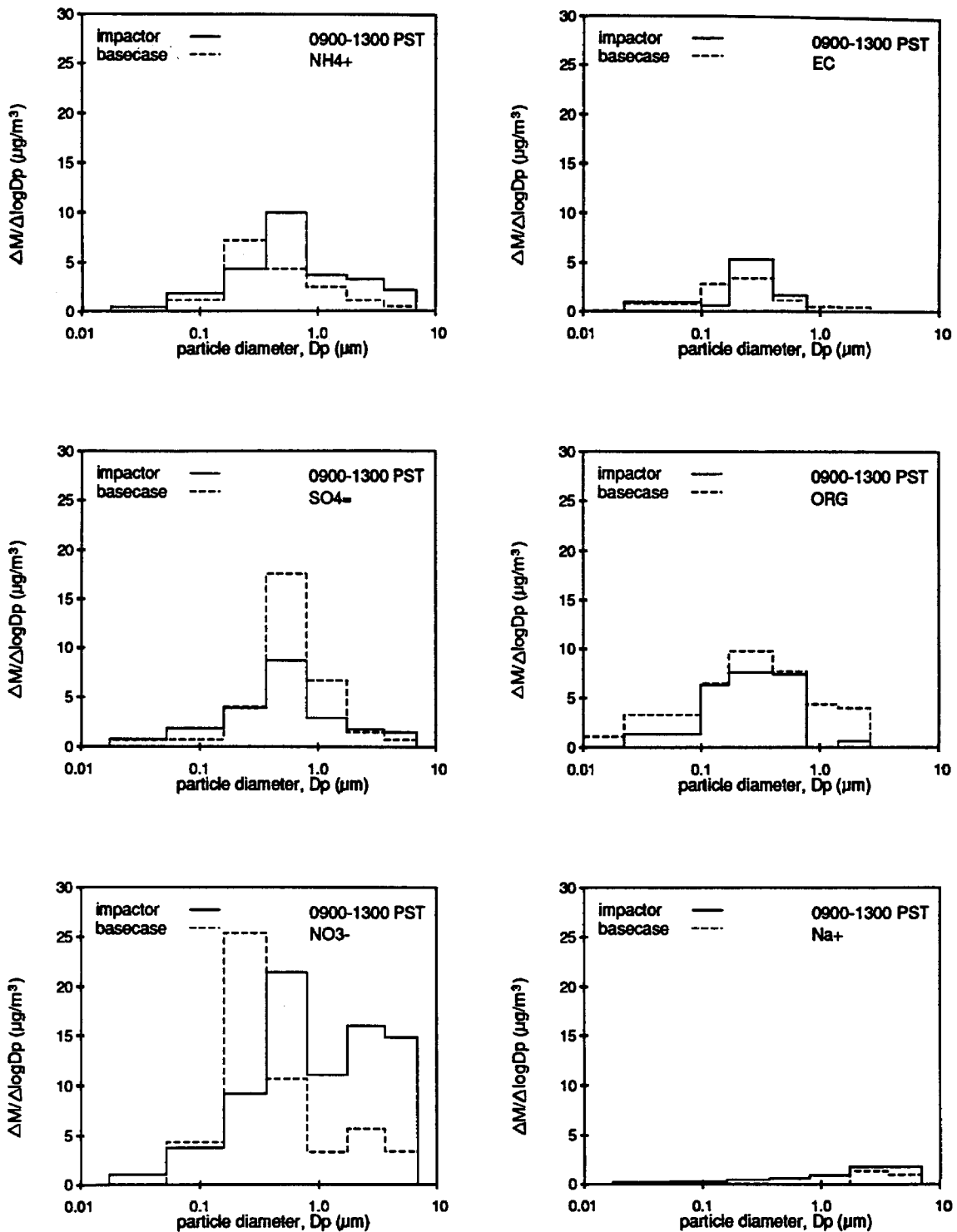


Figure 3.8: Basecase model predictions of the mass distribution,  $\Delta M/\Delta \log D_p$ , for individual chemical species compared to impactor measurements during the sampling period 0900-1300 PST of August 28, 1987, at Claremont, California.

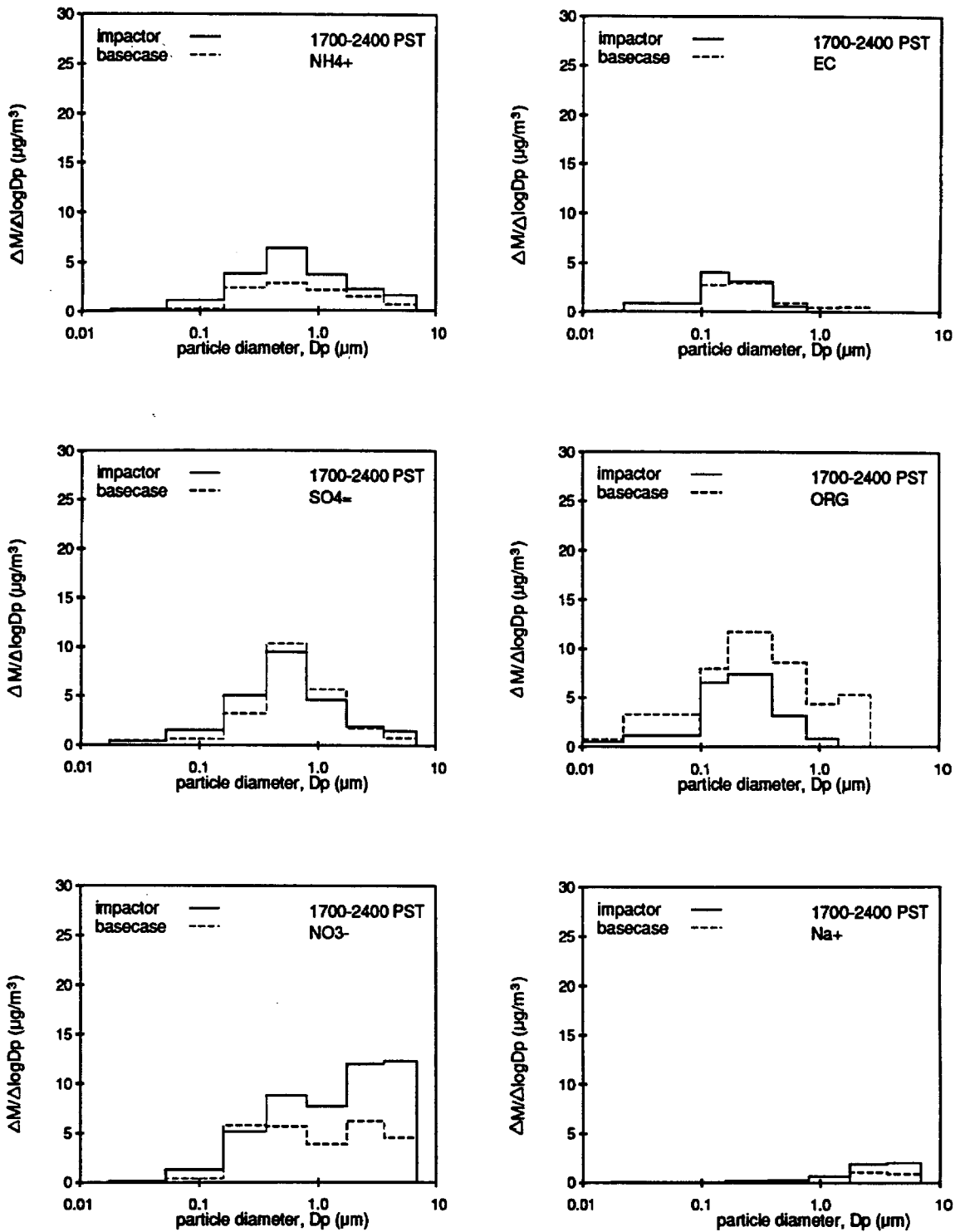


Figure 3.9: Basecase model predictions of the mass distribution,  $\Delta M/\Delta \log D_p$ , for individual chemical species compared to impactor measurements during the sampling period 1700-2400 PST of August 28, 1987, at Claremont, California.

ter samples with the exception of the first sampling period of the day, during which no impactor measurements were made.

Figures 3.8 and 3.9 show the impactor data for six individual species compared to model predictions. The model predictions which arise from particles in 15 different diameter intervals are cast into the same format as the impactor data by first graphing the model results as a step function volume diagram of  $\Delta V/\Delta \log d_p$ , then slicing that diagram at the cutpoints between the various impactor stages, followed by summing like species in each impactor size interval. Figure 3.8 shows a sampling period in the middle of the day (0900–1300 PST), while Figure 3.9 shows a nighttime sample (1700–2400 PST).

The impactor measurements and model predictions for elemental carbon agree well for both sampling periods. Most of the elemental carbon is present in particles less than  $1 \mu\text{m}$  in diameter, consistent with the domination of emissions of elemental carbon by sources such as diesel engines. The observations and model predictions for the size distribution of organic material are also in relatively good agreement, with most of the material present in particles between  $0.1$  and  $1.0 \mu\text{m}$  in diameter.

The impactor measurements of sodium ion show a progressive increase with increasing particle diameter with the majority of material in particles larger than  $1 \mu\text{m}$  in diameter. The model predictions place most of the material in particles larger than one micron for both sampling periods.

The impactor measurements for  $\text{NH}_4^+$  and  $\text{SO}_4^-$  show size distributions that peak just below  $1 \mu\text{m}$  in diameter, reflecting the droplet mode formed by the fogwater chemical reactions. Model predictions for  $\text{SO}_4^-$  during the midday sampling period capture the droplet peak seen in the impactor mea-

surements but with more sulfate present in particles near  $1\ \mu\text{m}$  in diameter than was observed by the impactor. In the nighttime sampling period, the sulfate peak is reproduced very well by the model. The model predictions for  $\text{NH}_4^+$  in the base case show a similar shape for both sampling periods, capturing most of the features of the impactor measurements, although the predicted  $\text{NH}_4^+$  distribution does not reach the peak concentrations seen in the impactor measurements because aerosol ammonium is underpredicted.

Impactor measurements of  $\text{NO}_3^-$  during the midday sampling period show a fine particle peak just below  $1\ \mu\text{m}$  and a smaller coarse particle peak located between about 2 and  $10\ \mu\text{m}$  in diameter. The model predictions also show two peaks, although their height and location do not exactly match the impactor measurements. The nighttime nitrate size distribution measured by the impactor is flatter, as is the shape of the size distribution predicted by the model. The shortfall in predicted coarse particle nitrates mirrors the relative underprediction of  $\text{Na}^+$  at that time.  $\text{Na}^+$  concentrations are almost impossible to predict with greater accuracy because upwind sea salt initial conditions are not known with tremendous accuracy.

To describe the differences and similarities between the impactor measurements and model predictions, the frequency distribution of residual values was calculated over all impactor stages and all hours of simulation for the basecase model calculations, altered pH, and altered fog duration sensitivity tests. A single residual is defined as the model prediction minus the observed value for a single impactor stage. Figure 3.10 shows these frequency distribution plots for elemental carbon, organic material,  $\text{Na}^+$ ,  $\text{NH}_4^+$ , and  $\text{NO}_3^-$ . Residual plots for  $\text{SO}_4^{2-}$  are shown for the basecase model with a fog pH of 4, for fog pH at 3.5 and 4.5, and for the sensitivity test with a less extensive fog.

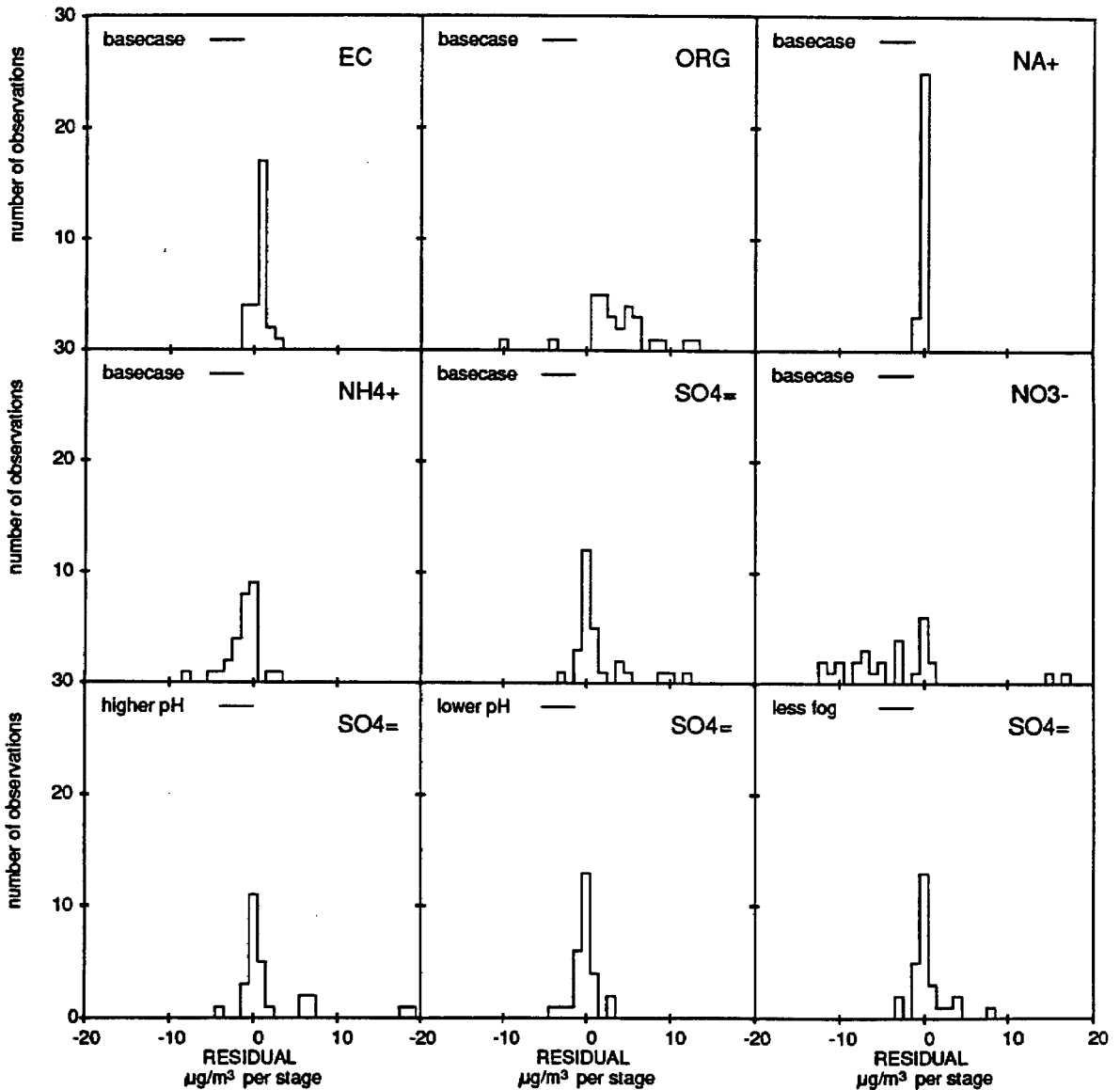


Figure 3.10: Histograms of the frequency of occurrence of concentrations residuals (predicted minus observed) determined for all individual impactor stages and all times during August 28, 1987, at Claremont, California.

The narrow frequency distributions for elemental carbon and sodium reflect the good agreement between impactor measurements and model predictions. The frequency distribution for organic material shows a number of positive residuals, reflecting overprediction by the model relative to some of the impactor measurements. It is important to recall that average predicted PM<sub>2.5</sub> organic material concentrations match those measured by filter sampling very well; there are differences in organics concentrations measured by different methods during SCAQS. The residual values are centered at 0.0 for NH<sub>4</sub><sup>+</sup> and SO<sub>4</sub><sup>-</sup>, indicating that the most frequent difference between model predictions and observations lies in the range  $\pm 0.5 \mu\text{g m}^{-3}$  on each impactor stage. The underprediction of PM<sub>2.5</sub> ammonium ion concentrations is reflected in the higher frequency of negative residuals than positive residuals. The frequency distribution of the residuals for SO<sub>4</sub><sup>-</sup> remains centered on zero in all three fog sensitivity cases studied. The frequency distribution of residual differences between PM<sub>2.5</sub> nitrate impactor measurements and model predictions is distributed over a larger range, reflecting the fact that observed NO<sub>3</sub><sup>-</sup> concentrations are underpredicted by the model and associated emissions data while most other species are matched very closely.

### 3.3.5 Aerosol Size Distribution

In the present application, a trajectory-based model was configured to predict the mass concentrations of the most important aerosol species at 15 discrete particle sizes over the size range from 0.01 to 10  $\mu\text{m}$  particle diameter. An overall aerosol volume distribution can be drawn from this information, by graphing the incremental particle volume,  $\Delta V$ , represented by particles in each size class divided by the width of the logarithmic particle

size interval,  $\Delta \log d_p$ , defined by the log-mean diameter difference between particles of that size and its nearest neighboring particle size classes. Figure 3.11 shows the aerosol volume distribution ( $\Delta V / \Delta \log d_p$ ) predicted for the aerosol arriving at Claremont at six hour intervals on August 28, 1987, and the aerosol volume as measured by electrical aerosol analyzers (EAA) and optical particle counters (OPC) at Claremont. The observed aerosol volume distribution presented over the size range from 0.01  $\mu\text{m}$  to 2.83  $\mu\text{m}$  particle diameter is from the combined data taken with a TSI Model 3030 EAA and a PMS LAS-X OPC as described by Eldering *et al.* (1994). The measured aerosol size distribution shown here has been extended so that the coarse fraction volume in particles from 2.5 to 10  $\mu\text{m}$  diameter matches the volume inferred from simultaneous filter-based measurements of aerosol properties (see Eldering *et al.*, 1994, Case B; there is only one overall measured value of  $\Delta V / \Delta \log d_p$  in the coarse particle size range and that value is a 4 to 7 hour average that is not specific to the arrival time of a single air parcel). The model predictions in Figure 3.11 have been graphed after removing aerosol water from the particles since it has been determined previously that the size distribution instruments at Claremont dried out the aerosol while making their measurements (Eldering *et al.*, 1994). The size distribution measurements have greater size resolution than the model in the fine particle mode while the model has greater size resolution than the measurements in the coarse particle mode, so exact agreement cannot be achieved, but the comparison nevertheless is instructive.

Aerosol size distributions predicted by the model are presented in Figure 3.11 for the basecase for trajectories arriving at Claremont at 6-hour intervals (0500, 1100, 1700, and 2300 PST). All of the measured aerosol size

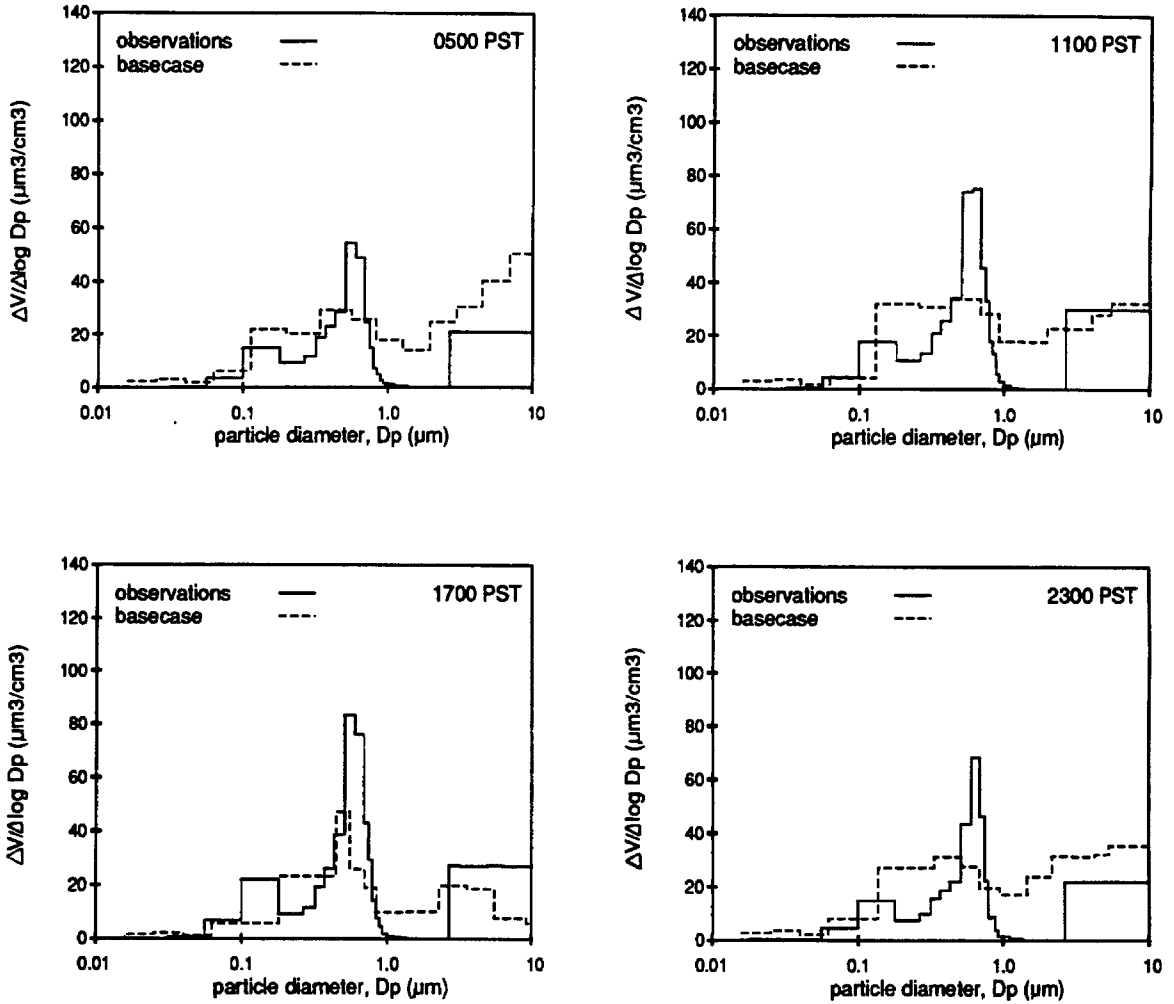


Figure 3.11: The aerosol size distribution as measured by electrical aerosol analyzers and optical particle counters and the aerosol size distribution predicted by the basecase model calculations for air parcels arriving at Claremont at 6-hour intervals on August 28, 1987.

distributions have two distinct submicron modes, one at just above  $0.1 \mu\text{m}$  particle diameter and another at just below  $1.0 \mu\text{m}$  particle diameter. The model predictions, although they contain less size-resolution in the submicron range, do show a similar shape. The aerosol size distributions created by the basecase model predict that there is little aerosol volume below  $0.1 \mu\text{m}$ , a peak just below  $1.0 \mu\text{m}$ , and a substantial volume of material between  $2.5$  and  $10 \mu\text{m}$  particle diameter. The reduction in predicted coarse particle concentrations in the trajectory arriving at 1700 PST compared to those arriving at 0500, 1100 and 2300 PST is in part due to additional deposition during the long residence time for that air parcel within the fog and is in part due to the greater vertical mixing that occurs for primary particles due to the higher mixing depths in the afternoon. The trajectory arriving at 1700 was within a fog for 9 hours compared to 2 hours for the other trajectories shown.

The chemical composition and size distributions for the basecase trajectories arriving at 0500, 1100, 1700, and 2300 PST are presented in Figures 3.12 and 3.13. These figures illustrate how the ionic material, organics, elemental carbon, crustal material, and water fit together to shape the overall aerosol size distribution. Particles with diameters between  $0.1$  and  $1.0 \mu\text{m}$  contain significant amounts of elemental carbon, organic material,  $\text{SO}_4^{=}$ ,  $\text{NH}_4^+$ ,  $\text{NO}_3^-$ , secondary organic aerosol, metal-rich industrial primary particles, and unidentified material. The larger particles (greater than  $1 \mu\text{m}$  in diameter) are dominated by crustal material, with some coarse particle  $\text{NO}_3^-$  and organic material.

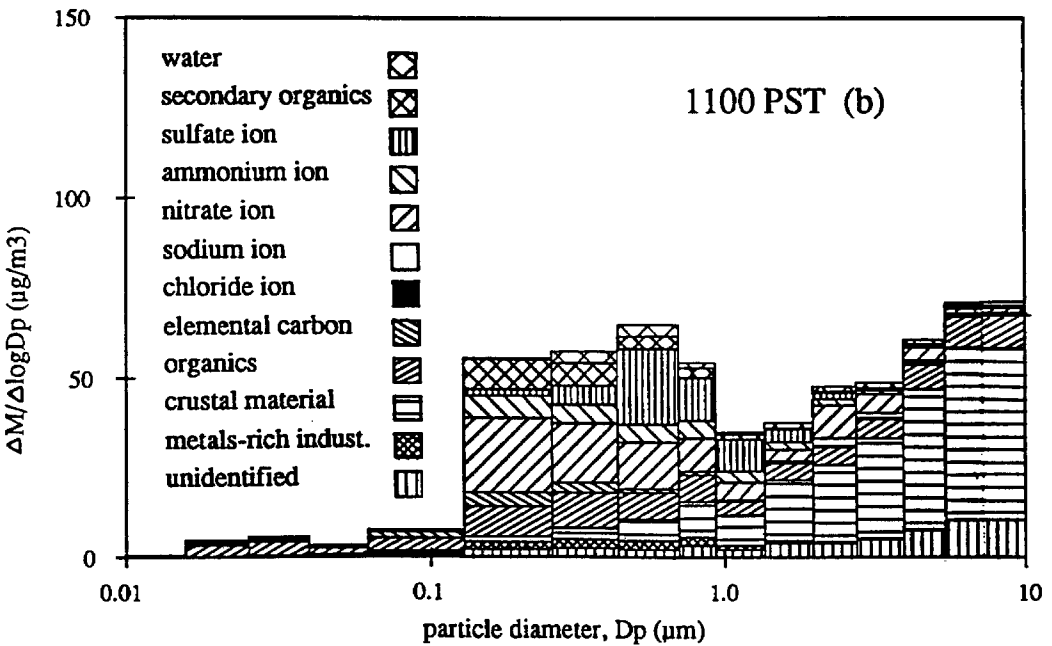
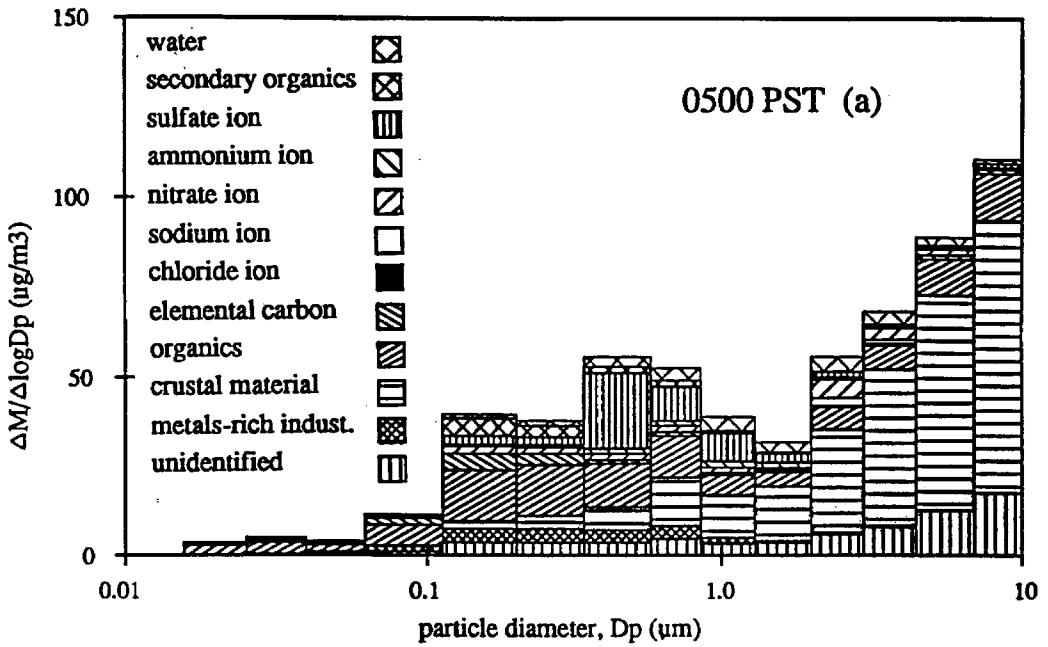


Figure 3.12: The size distribution of aerosol chemical composition as predicted by the basecase model at Claremont, California, on August 28, 1987: (a) 0500 PST; (b) 1100 PST.

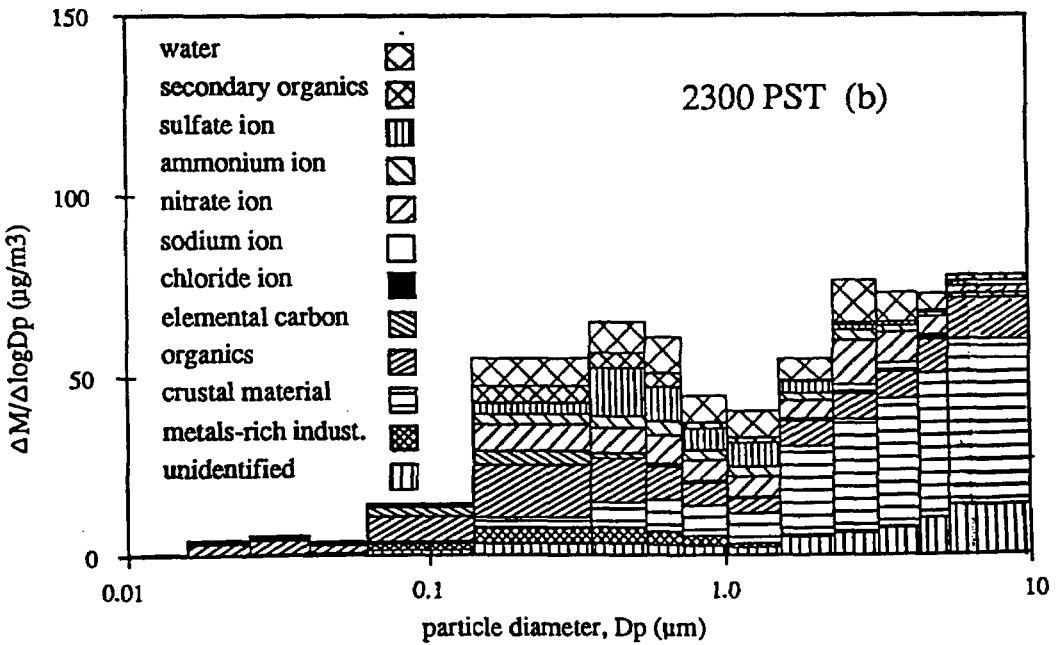
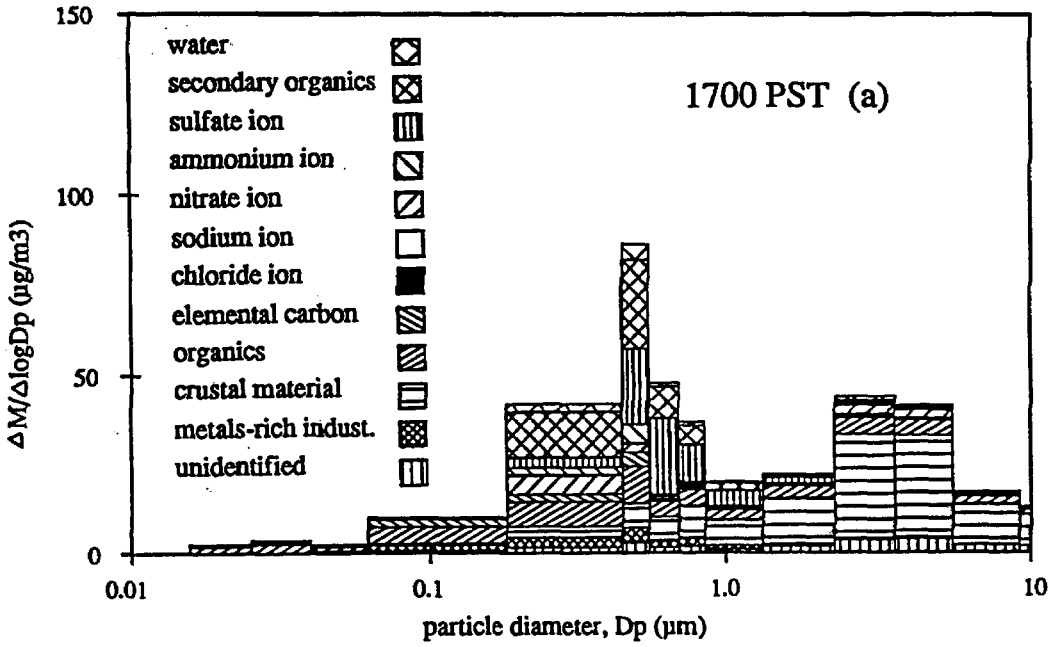


Figure 3.13: The size distribution of aerosol chemical composition as predicted by the basecase model at Claremont, California, on August 28, 1987: (a) 1700 PST; (b) 2300 PST.

### 3.3.6 Light Scattering Coefficient

Particle light scattering coefficient values were measured during the SCAQS study using nephelometers by a number of investigators, including scientists from General Motors Research Laboratory (GM) and the University of Illinois (UI). These data sets are discussed in detail by Eldering *et al.* (1994). A comparison of measured and modeled particle light scattering coefficient values at Claremont for the basecase model calculations are presented in Figure 3.14 at two different wavelengths. It is seen that there is good agreement between predictions and observations at all times except possibly at night near the end of August 28.

The total light extinction coefficient next was calculated by summing the light scattering by particles, light absorption by particles, light scattering by air molecules, and light absorption by the  $\text{NO}_2$  concentrations predicted by the model. The contribution of each of these terms to the total light extinction coefficient is illustrated in Figure 3.14(c). This time series of the light extinction coefficient values was translated into estimated visual range values using Koschmieder's formula (Middleton, 1952) with threshold contrast values of 0.02 and 0.05. The threshold constant of 0.02 was originally employed by Koschmieder for visual range calculations, although a value of 0.05 produces better agreement with reported visual range observations (Gordon, 1984). It is seen that the visual range at Claremont was estimated to be in the range of 8 to 21 kilometers over the August 28 period studied.

## 3.4 Conclusions

A source-oriented model for air pollutant effects on visibility has been developed that can compute light scattering, light extinction, and estimated

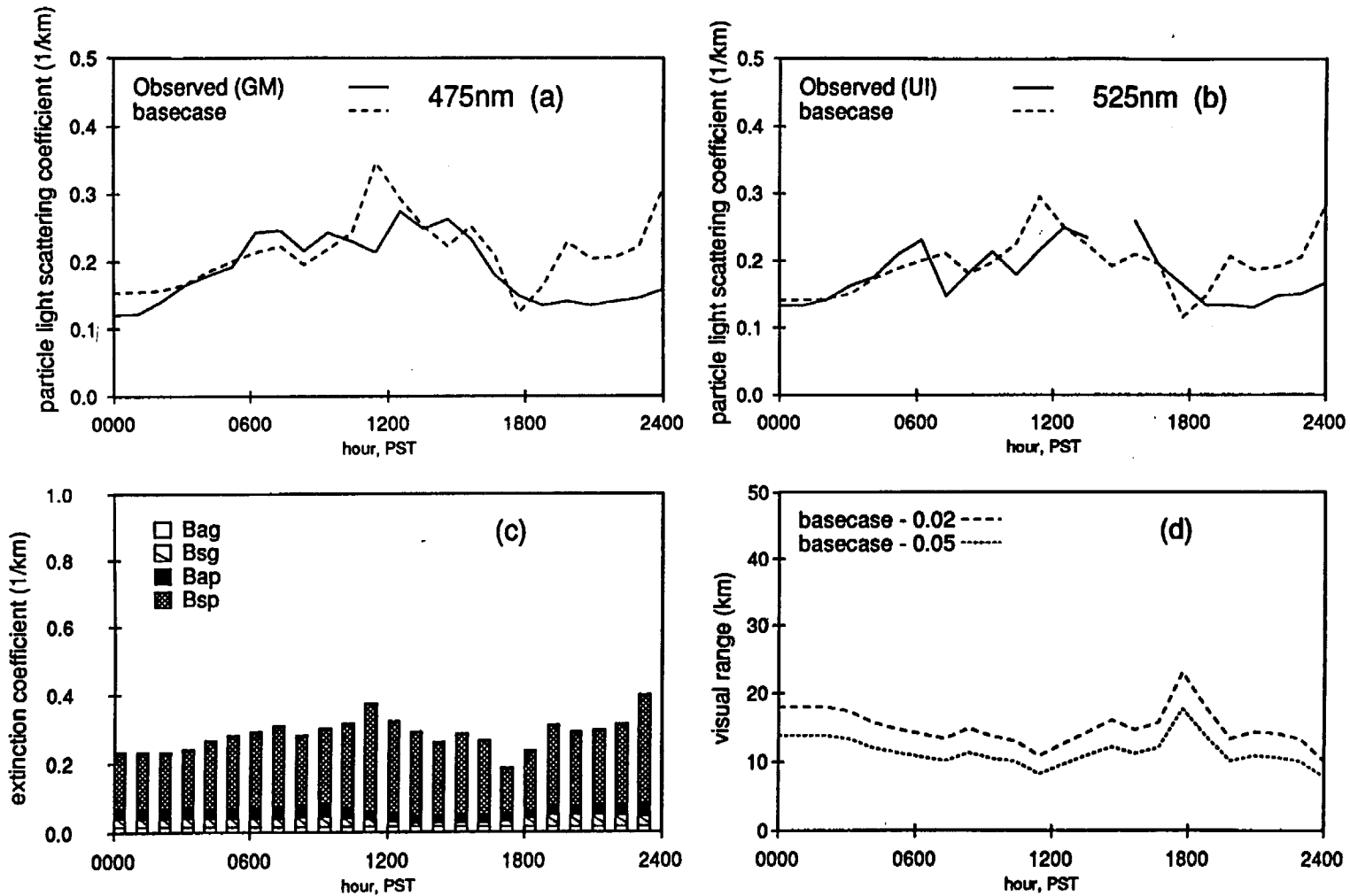


Figure 3.14: Observed and predicted light scattering by particles at (a) 475 nm and at (b) 525 nm. Contributions to the total extinction coefficient (c) are translated into visual range estimated using Koschmieder's formula (d) for two values of the threshold contrast for human observers (0.02 and 0.05).

visual range directly from data on gas-phase and primary particle-phase air pollutant emissions from sources. The importance of such a model is that it can be used to compute the effect of emissions control proposals on visibility related parameters in advance of the adoption of such control programs.

The model has been assembled by embedding several aerosol process modules within the photochemical trajectory model previously developed for aerosol nitrate concentration predictions by Russell *et al.* (1983) and Russell and Cass (1986). These modules describe the size distribution and chemical composition of primary particle emissions, the speciation of organic vapor emissions, atmospheric chemical reactions, transport of condensible material between the gas and particle phases, fog chemistry, dry deposition, and atmospheric light scattering and light absorption. The aerosol size distribution and compositional data for primary emissions from sources are taken from a series of source tests conducted specifically for the purpose of supporting such a modeling effort.

Model predictions have been compared to observed values using 48 hour trajectories arriving at Claremont, California, at each hour of August 28, 1987, during the Southern California Air Quality Study. Concentrations of gas-phase pollutants  $\text{NO}_2$ ,  $\text{HNO}_3$ , and  $\text{NH}_3$  are reproduced closely by the model while  $\text{O}_3$  concentrations are underpredicted, as has been the case for all previous  $\text{O}_3$  simulations at Claremont using the SCAQS emissions data (see Harley *et al.*, 1993). Average  $\text{PM}_{10}$  and  $\text{PM}_{2.5}$  particle mass concentrations and filter-based measurements of elemental carbon and organic material are reproduced well with a bias of less than 10% in each case. The bias between basecase predictions and observed values of  $\text{PM}_{2.5}$   $\text{SO}_4^-$  concentrations is about 30%. Predicted aerosol elemental carbon and  $\text{Na}^+$  concentrations

are each within  $0.6 \mu\text{g m}^{-3}$  of the observed values on average. Aerosol ammonium and nitrate concentrations are underpredicted due to a shortage of total inorganic nitrate production by the model (i.e., less  $\text{HNO}_3$  is produced than it would take to match observed aerosol nitrate values). If vapor phase organics emissions to the model were increased further, as many believe is warranted to account for hydrocarbon sources that have been under-counted by the government, then both  $\text{O}_3$  and inorganic nitrate production may increase, possibly resolving the two discrepancies between observations and predictions.

The predicted size distribution of the aerosol at Claremont is central to accurate predictions of light scattering levels. The predicted aerosol size distribution and chemical composition generally captures the composition, volume, and shape of the measured submicron aerosol, and the correct volume of coarse material is predicted on average.

Light scattering coefficient values depend on the aerosol size distribution and refractive index and good agreement is attained between model predictions and measurements.

In conclusion, the source-oriented model for the effects of air pollutants on visibility has been demonstrated to successfully predict the level of atmospheric light scattering while starting with data on the emissions of primary pollutants at their source, followed by a mechanistic simulation of atmospheric chemistry and aerosol processes.

## 4 An Image Processing Based Visibility Model

### 4.1 Introduction

Communication of the effects of atmospheric aerosols on the visual appearance of a scene is a complicated problem. Physical parameters such as contrast, light scattering and extinction coefficient values, light intensity values, and blue-red luminance ratios have been used to describe scenes and the effects of pollution on their visual appearance. Other recent work has strived to describe scenes in terms of information that relates to human perceptions such as relative color, brightness, and detail. A third approach presents information concerning visibility in the form of synthetic color photographs, simultaneously describing literally millions of points in a scene in a format that is familiar to a wide audience.

Predictive models that describe visual conditions in terms of synthetic photographs are based on image processing technology that is linked to atmospheric radiative transfer calculations. Williams *et al.* (1980) describe the Los Alamos Scientific Laboratory (LASL) visibility modeling system which is applied to plume blight conditions. This system incorporates the power of simulated photographs to display the computed appearance of coherent plumes that are illuminated by a theoretically based description of the atmospheric radiation field. A quantitative comparison of actual and simulated

---

Eldering A.; Larson S. M.; Hall, J. R.; Hussey, K. J.; Cass, G. R. Development of an

photographs was not reported. Malm *et al.* (1983) present techniques for visualizing the effects of uniform haze, which differ from the model of Williams *et al.* (1980) in that the clear day sky radiance field is extracted from photographic slides rather than being calculated from an atmospheric simulation model. Larson *et al.* (1988) describe experiments in which quantitative tests were performed to assess the accuracy of a visibility model for regional haze similar to that of Malm *et al.* (1983). It was found that contrast and visual range were reproduced well but that the sky in the synthetic smog images was too blue.

The present chapter reports the development and verification by field experiment of an improved image processing based visibility model based on the work of Larson *et al.* (1988) and Sloane (1984ab). This model is applied to regional haze conditions and incorporates a theoretically based calculation of sky color and intensity in conjunction with photographic data on objects in the field of view.

## 4.2 Formulation of the Model

Middleton (1952) discusses the derivation of an equation which can describe the apparent radiance of an object that is viewed at a distance through a polluted atmosphere. Middleton allows for altitudinal variation of the scattering and extinction coefficients. For the case of the horizontal line of vision through an atmosphere that is uniformly mixed with an extinction coefficient that is uniform over the viewed area, his derivation simplifies to the following equation:

---

Improved Image Processing Based Visibility Model. *Environ. Sci. Technol.*, **27**, 626–635, 1993.

$$I(x) = I_0 e^{-b_{ext}x} + I_h(1 - e^{-b_{ext}x}) \quad (4.1)$$

where  $I(x)$  refers to the apparent monochromatic intensity of radiance at the location of the observer,  $I_0$  is the inherent radiance of the object, and  $I_h$  is the radiance of the horizon sky. The extinction coefficient is represented by  $b_{ext}$ , and the distance from the viewer to the object is  $x$ . The two terms on the right-hand side of the equation, respectively, account for light from the object diminished by atmospheric extinction, and skylight that is scattered into the line of sight. In the present work, the radiance of the sky near the horizon will be calculated theoretically by a procedure discussed in a later section and it will be referred to as  $I_{sky}$ . The above equation holds true for a particular wavelength of light, and this will be denoted by the subscript  $\lambda$ .

$$I(x)_\lambda = I_{0,\lambda} e^{-b_{ext,\lambda}x} + I_{sky,\lambda}(1 - e^{-b_{ext,\lambda}x}) \quad (4.2)$$

A photograph, or simulated photograph, provides a way to display an array of information such as  $I(x)$  for a large scene. Photographic film can be considered to be an integrating mechanism. Photographic images are made up of three color-sensitive layers, and each color-sensitive layer integrates over a spectrum of wavelengths with varying sensitivity. For the example of Kodachrome 25 color slide film, the blue-sensitive layer has nonzero wavelength dependent sensitivities over the range of 400 to 540 nm. Photographic densitometry then can be used to measure film densities in the red, green, and blue from which the light intensities to which the film was exposed can be estimated. Equation (4.2) can be rewritten to represent the light collected

in the red, green, or blue color plane as follows:

$$I'(x) = I'_0 e^{-\overline{b_{ext}}x} + I'_{sky} (1 - e^{-\overline{b_{ext}}x}) \quad (4.3)$$

where the  $I'$  are weighted average intensity of radiance values over the wavelength band corresponding to one of the three color planes. The  $I'_0$  are determined from the measured film densities and thus include a physical integration over both the film sensitivity curves and the color separation filter curves. The parameter  $\overline{b_{ext}}$  is an effective extinction coefficient calculated for each wavelength band as a weighted average of the true wavelength-dependent extinction coefficient values using film sensitivity curves like those shown by Ferguson (1980) as the weighting factors. Due to the narrowness of the film sensitivity curves, the error introduced by such an approximation in the application considered here is minimal. (The weighted average of the product of the wavelength-dependent intensities,  $I_\lambda$ , times the exponential terms involving  $b_{ext,\lambda}$  at each wavelength differ from the product of the averages as used in equation 4.3 by less than 3% for any viewing angle and color plane examined in the present study. For an extremely clear sky approaching pure Rayleigh scattering, the errors will be larger.)

A synthetic photograph of the way that a scene would appear under smoggy day conditions is created by applying equation (4.3) successively to each point that depicts an object in a gridded digital representation of the scene of interest, while light intensities in the sky are calculated directly from a theoretical skylight model. The grid coordinates are established by scanning a 35mm color photographic slide of the scene over a 1800 by 1200 sample pattern which defines  $2.16 \times 10^6$  picture elements (pixels), each 25  $\mu\text{m}$  on a side. The numerical densities of the film are recorded on a scale

of 0 (dark) to 255 (light) while scanning successively through three color separation filters (Wratten 92, 93, and 94 plus an infrared cutoff filter). This creates digital images in three color planes – red, green, and blue – which when superimposed result in a full color image.

The input data for visibility modeling calculations then are organized according to the grid system defined while scanning the color slide. Digital images are created that describe (1) the distance  $x$  from the observer to each picture element in the scene, (2) the array of sky radiance values,  $I'_{sky}$ , for each pixel in each of the red, green, and blue color planes, and (3) the array of inherent radiance values  $I'_o$  for the picture elements corresponding to the objects in the field of view in each of the three color planes. The distance image can be obtained by mapping techniques, as described by Larson *et al.* (1988). The inherent radiance map that describes the objects is computed from the film densities apparent in a clear day photograph of the scene of interest, as will be described shortly. The sky radiance images require further modeling calculations, as follows.

#### 4.2.1 Sky Radiance Images

The radiative transfer equation given by Chandrasekhar (1960) that governs the radiance field within a plane-parallel atmosphere is

$$\mu \frac{dI_{\lambda}(\tau, \mu, \phi)}{d\tau} = I_{\lambda}(\tau, \mu, \phi) - J_{\lambda}(\tau, \mu, \phi) \quad (4.4)$$

with:

$$J_{\lambda}(\tau, \mu, \phi) = \frac{\omega_0}{4} F_{\lambda} P(\mu, \phi; \mu_0, \phi_0) \exp\left(\frac{-\tau}{\mu_0}\right)$$

$$+ \frac{\omega_0}{4\pi} \int_0^{\pi} \int_{-1}^{+1} P(\mu, \phi; \mu', \phi') I_\lambda(\tau, \mu', \phi') d\mu' d\phi' \quad (4.5)$$

where

$\lambda$  is the wavelength of light considered,

$I_\lambda$  is the wavelength dependent intensity of radiance,

$J_\lambda$  is the source function,

$\pi F_\lambda$  is the incident solar irradiance,

$\omega_0$  is the single scattering albedo (the ratio of the scattering coefficient to the extinction coefficient),

$\tau$  is the optical depth,  $\tau = \int_0^Z b_{ext} dz'$ , where  $Z$  is the distance to the ground from the top of the atmospheric layer,

$\mu$  is the cosine of the zenith angle of the observer's line of sight,

$\mu_0$  is the cosine of the zenith angle of the sun,

$\phi$  is the azimuth angle of the observer's line of sight,

$\phi_0$  is the azimuth angle of the sun, and

$P(\mu, \phi; \mu', \phi')$  is the phase function which describes the probability that light from the direction  $(\mu', \phi')$  will be scattered in the direction  $(\mu, \phi)$ .

The two terms that contribute to the source function,  $J_\lambda$ , represent the singly and multiply scattered radiation. The boundary conditions applicable to equation (4.4) are (1) that the only downward directed radiance at the top of the atmosphere is incident sunlight (no diffused downward flux) and (2) that Lambertian (isotropic) reflection occurs at the ground.

Equation (4.4) can be solved exactly for a few specific cases, but approximate analytical solutions more often are applied in visibility modeling due to the need to treat anisotropic scattering. The methods used include two and four stream approximations (Liou, 1974; Coakley and Chylek, 1975; Meador and Weaver, 1980, the doubling method (Twomey *et al.*, 1966), Monte Carlo methods (Plass and Kattawar, 1968), and solution by spherical harmonics (Dave and Canosa, 1974). Many of these methods are discussed by Hansen and Travis (1974) and by Wiscombe (1983).

Kaufman (1979) developed an extension of the two stream formulation of Coakley and Chylek (1975) which allows for the inclusion of both the azimuth and zenith angle dependence of the sky radiance. In addition, upwelling and downwelling fluxes are differentiated, and flux conservation is not invoked, which provides for a more realistic treatment of absorbing atmospheres. Sloane (1988) notes corrections to Kaufman's derivation and generalizes the solution so that it is valid when the light source is diffuse skylight that has been scattered within the upper atmosphere. This solution has been implemented in a computer code by Sloane (1984b, 1986, 1988). In this algorithm, Legendre polynomials are used in the evaluation of the angular scattering intensities, and Riccati-Bessel functions are used to evaluate the scattering cross sections. Recursion relations are used for the evaluation of the Riccati-Bessel functions, with the use of backward recursion where upward recursion is not stable (Sloane, 1984b). Sloane's implementation of Kaufman's formulation has been incorporated into the skylight module of our visibility model for the purpose of calculating light intensity as a function of position in the sky. Sky radiance values as a function of wavelength then are weighted according to the film sensitivity curves to create the maps of sky radiance for each color plane that are used with equation (4.3).

#### 4.2.2 Object Inherent Radiance Images

When a color slide is scanned through color separation filters, the film density values bear a direct relationship to the amount of light received by the film. The characteristic curve of a film that relates film density to the log of exposure (*lux sec* or *lumen sec m<sup>-2</sup>*) is provided by the film's manufacturer (see Ferguson, 1980). Exposure data read from the film densities and the

product of band radiance and exposure time ( $W m^{-2} ster^{-1} \times sec$ ) are related by a single constant. This constant depends on camera characteristics and can be estimated by the construction of a calibration curve.

The calibration curve can be constructed from a clear day photograph of the scene of interest (base day). The film density, and therefore exposure, at a number of points in the sky area for each color plane can be measured. The skylight model described in section 4.2.1 is exercised for the same sky positions. Spectral radiance values computed theoretically from the skylight model are weighted by the film sensitivity curve and numerically integrated, resulting in clear day band radiance ( $I'_{sky}$ ) values for each point in the sky examined in each color plane. Regression of  $I'_{sky}$  on radiant intensities derived from film exposure data provides the calibration constant which holds for photographs taken with the same film and camera settings which then can be used to convert between film exposure data and quantitative radiance estimates.

The clear day base photograph next is used to determine gridded values of  $I'_o$ , the set of inherent radiance values of the objects in the field of view. The atmospheric extinction coefficient as a function of wavelength at the time that the clear day base photograph was taken can be determined experimentally by the procedures described by Larson *et al.* (1988). Then using the sky radiance map containing  $I'_{sky}$  values, the distance map containing the  $x$ 's, and computed values of  $\overline{b_{ext}}$  for the clear day plus the array of  $I'(x)$  values determined from the clear day film densities, equation (4.3) is solved to create an array of  $I'_o$  values at each point in the scene where an object appears in each of the three color planes.

### 4.2.3 Prediction of the Appearance of Regional Haze Episodes

To create a synthetic image of the scene of interest under altered air pollutant loading conditions,  $\overline{b_{ext}}$  and an array of  $I'_{sky}$  values are calculated for each color plane for the conditions to be modeled. The distances,  $x$ , from the observer to each of the objects in the field of view are known for the scenes to be used. The distance image,  $\overline{b_{ext}}$ , and the arrays that describe  $I'_{sky}$  and  $I'_0$  are inserted into equation (4.3), and an array of  $I'(x)$  values corresponding to the polluted conditions is calculated for each color plane. The calibration chart relating radiance to exposure and the film characteristic curves are used to convert these values into film densities. A film writing device then is used to produce a photographic negative from which prints of the predicted appearance of the scene under polluted conditions can be made. Lower quality images can be displayed on a cathode ray tube monitor or through the use of a color laser printer.

## 4.3 Experimental Program

An experimental program was conducted by Larson *et al.* (1988) to acquire data suitable for the evaluation of image processing based visibility models. During April and August of 1983 photographs were taken of well defined scenes under clear day and under heavy smog conditions in Pasadena, California, in conjunction with atmospheric aerosol size distribution and chemical composition measurements from which the atmospheric aerosol scattering and extinction coefficient can be calculated. Photographs were taken of two vistas at solar noon, one looking northeast, known as the downtown Pasadena view. The other view is to the north, known as the San Gabriel Mountains scene. The clear day, April 7, photographs are shown in Figure 4.1 (a) and

(d) and the actual smoggy day, August 25, photographs are shown in Figure 4.1 (b) and (e). As part of the present study, data collection was resumed in June of 1988 with one modification: the addition of radiometer measurements of actual skylight radiance intensities as a function of position in the sky that will be discussed in section 4.3.3 of this chapter.

Atmospheric aerosol size distribution measurements were made at the time that the photographs were taken using an electrical aerosol analyzer (EAA) and optical particle counters (OPC). In the 1983 sampling period, measurements were made in the size range from 0.0075 to 1.0  $\mu\text{m}$  particle diameter using a TSI model 3030 EAA. In the 1988 study, particle concentrations in the size range 0.09 to 3.00  $\mu\text{m}$  were sampled with a Particle Measurement Systems (PMS) Model ASASP-X-32-CH laser OPC. During both periods, particle size distributions in the range 0.50 to 50  $\mu\text{m}$  were measured with a PMS Model CSASP-100-HV laser OPC. The atmospheric scattering coefficient was measured with an integrating nephelometer (Meterology Research Inc., Model 1550B).

To obtain information on the chemical composition of the atmospheric aerosol, filter samples were collected over a four-hour period surrounding the time that the photographs were taken. Fine particles ( $d_p < 2.1\mu\text{m}$ ) were collected with three parallel filter holders downstream of an AIHL-design cyclone separator (John and Reischl, 1980). Details of the 1983 experiments are discussed by Larson *et al.* (1988). In the 1988 experiment, aerosol mass concentrations were determined from samples collected at a flow rate of 10 L/min on 47 mm diameter Teflon filters (Gelman Sciences, 2 $\mu\text{m}$  pore size) which were weighed repeatedly at low relative humidity before and after use. Information on chemical composition included the concentration of 34

Figure 4.1: Actual photographs and synthetic images: April 7, 1983 clear day photograph of the San Gabriel Mountains scene (a) and Downtown Pasadena scene (d); August 25, 1983 smoggy day photographs for the same scenes (b,e respectively); visibility model synthetic images of smoggy day (c,f respectively).



a



b



c



d



e



f

trace elements determined by X-ray fluorescence analysis of the Teflon filter samples. These elements ranged in atomic weight from aluminum to lead. The concentrations of the water soluble ions  $\text{Na}^+$ ,  $\text{NH}_4^+$ ,  $\text{K}^+$ ,  $\text{F}^-$ ,  $\text{Cl}^-$ ,  $\text{NO}_3^-$ , and  $\text{SO}_4^{2-}$  were determined by ion chromatographic analysis of the extract of a second set of samples collected at 10 L/min on Teflon filters (47mm, Gelman, 2.0  $\mu\text{m}$  pore size). Organic and elemental carbon concentrations were determined from samples collected at 10 L/min on quartz fiber filters (Pallflex 2500 QAO). These filters were pre-fired to 600°C for 2 h prior to use in order to reduce their carbon blank. The carbon analysis was carried out by the method of Johnson *et al.* (1981).

A comparable set of open-faced filters were used to collect total suspended particulate matter and were analyzed in the same manner as the fine aerosol filters. Information on the coarse particle fraction of the atmospheric aerosol was determined from the difference between total and fine particle concentration data. Temperature and relative humidity were measured at the sampling site with a mercury thermometer and sling psychrometer in 1983 and with a hygrothermograph (Cole Parmer Model 8368-60) in 1988.

Atmospheric  $\text{NO}_2$  concentrations were measured at a routine air monitoring station of the South Coast Air Quality Management District, located about three hundred meters from the site at which the photographs were taken.

#### 4.3.1 Aerosol Chemical Characterization

Samples collected on August 25, 1983, April 7, 1983, and June 27, 1988 will be discussed here. April 7 was a particularly clear day, with prevailing winds from the desert. August 25 was a day with heavy smog conditions.

April 7 and August 25 also are almost symmetrically spaced on either side of the summer solstice, resulting in nearly identical illumination conditions and shadow patterns. The day of June 27 was moderately smoggy and was chosen due to the availability of radiometer data.

A material balance on the chemical composition of the aerosol is constructed by first converting measured trace metals to their common oxides. The mass concentration of organic carbonaceous material was taken to be 1.4 times the measured organic carbon mass concentration. The ionic material is distributed as follows:

$\text{Na}^+$  is associated with  $\text{Cl}^-$ ,

$\text{NH}_4^+$  is associated with  $\text{SO}_4^-$ ,

remaining  $\text{NH}_4^+$  is associated with  $\text{NO}_3^-$  to form  $\text{NH}_4\text{NO}_3$ ,

$\text{Na}^+$  remaining, if any, is associated with remaining  $\text{NO}_3^-$ ,

and the following compounds are formed, in order, with the remaining ionic species:  $\text{Na}_2\text{SO}_4$ ,  $\text{NH}_4\text{HSO}_4$ ,  $\text{PbSO}_4$ , and  $\text{H}_2\text{SO}_4$ .

The mass of dry material measured gravimetrically but not accounted for by chemical analysis is referred to as the residue (Sloane, 1984b). Densities are assigned to individual chemical species with the residue being assigned a density of  $2.3 \text{ g/cm}^3$  (Weast, 1985; Sloane 1984b). The dry volume of the aerosol then is calculated from the chemical species densities and masses. One estimate of the volume of water present in the particles is made by taking the difference between the aerosol volume computed from the measured size distribution and the aerosol volume calculated from the chemical composition of the filter samples. The volume of water present also is estimated by the method discussed by Sloane (1984b). This approach uses the ambient relative humidity and aerosol solubility to estimate the amount of water present. For

the fine particulate matter, the two methods of calculating the volume of water present agree fairly well. Sloane's water addition method predicts that  $0.23 \mu\text{g}/\text{m}^3$  water is present in the fine suspended particulate matter for April 7 while the volume difference method predicts that no water is present. For August 25, Sloane's water addition method predicts  $11.0 \mu\text{g}/\text{m}^3$  water and the volume difference method predicts  $10.2 \mu\text{g}/\text{m}^3$  water. For June 27, Sloane's water addition method predicts  $5.91 \mu\text{g}/\text{m}^3$  water and the volume difference method predicts that no water is present.

Agreement is not as good for the coarse particulate matter, but this is not a critical problem since uncertainties in determining the coarse particle volume are relatively unimportant to the outcome of visibility calculations. Particles in the coarse mode are relatively inefficient as light scattering particles and as a result contribute only a small fraction to total light scattering. The coarse dry aerosol mass concentration as measured by filter sampling on June 27 was found to be  $41.5 \mu\text{g}/\text{m}^3$ , and Sloane's method predicts that  $11.0 \mu\text{g}/\text{m}^3$  of water was present in that coarse aerosol. The coarse particle size distribution was scaled down proportionately across all particle sizes so that its volume is equal to the dry aerosol volume measured from the filter samples plus  $11.0 \mu\text{g}/\text{m}^3$  of water. The discrepancy between instrumental coarse aerosol volume distribution measurements and coarse aerosol volumes estimated from filter samples was not large for the April and August 1983 experiments, and the size distribution measurements were not rescaled.

#### 4.3.2 Calculation of the Extinction Coefficient

The extinction coefficient can be expressed as the sum of four contributions.

$$b_{ext} = b_{sp} + b_{ap} + b_{sg} + b_{ag} \quad (4.6)$$

The extinction coefficient is the sum of the components due to light scattering by particles,  $b_{sp}$ , light absorption by particles,  $b_{ap}$ , scattering of light by gases,  $b_{sg}$ , also known as Rayleigh scattering when the gas is air, and light absorption by gases  $b_{ag}$ . In the visibility model, absorption by  $\text{NO}_2$  gas is calculated according to the wavelength dependent absorption coefficients reported by Hodkinson (1966). Scattering by gases is calculated as Rayleigh scattering, with  $b_{sg} = 1.5 * 10^{-5} m^{-1}$  at a wavelength of 550 nm, and  $b_{sg}$  varying with wavelength as  $\lambda^{-4}$  (Penndorf, 1957). Light scattering and absorption by particles is calculated from Mie theory (Sloane, 1984a). The volume average refractive index of the fine aerosol and coarse aerosol is computed from the aerosol chemical composition data of Section 4.3.1 by the method described by Larson *et al.* (1988). The measured size distribution and refractive index values are supplied to the light scattering code. The scattering and absorption efficiencies are calculated for each diameter interval of the aerosol particle size distribution. Then  $b_{sp}$  and  $b_{ap}$  are calculated by integrating the product of the scattering and absorption efficiency factors for particles of each size and the number of such particles per unit air volume over the diameter range represented by the aerosol size distribution. These calculations are described in detail by Larson *et al.* (1988).

### 4.3.3 Verification of Radiative Transfer Module

An experiment was conducted on June 27, 1988, to verify the calculations of the skylight module. In conjunction with the data collection procedures described in Larson *et al.* (1988), skylight radiance intensity measurements were

made with a Photo Research PR-700-PC Spectrascan radiometer at 2 nm intervals from 390 to 730 nm. These measurements were made at three different angles above the horizon along the centerline of the downtown Pasadena (9.1, 12.5, 16.0°) and San Gabriel Mountains views (9.3, 13.3, and 14.9°). From the aerosol size distribution, aerosol chemical composition, NO<sub>2</sub> concentration, and meteorological information, the skylight module of the visibility model (Sloane, 1986) was used to calculate the predicted intensity of the skylight at the same viewing angles, for comparison against the radiometer data.

The skylight module requires the following inputs: sun angle above the horizon, viewer angle from the sun, mixing height, viewer height, ground reflectivity, NO<sub>2</sub> concentration, aerosol size distribution, and refractive index for fine and coarse aerosol fractions.

The module provides the following information as outputs: (1) a table of the wavelength dependent scattering and absorption coefficients for particles and gases, (2) spectral patterns, which include the intensity of light scattered singly and multiply, and (3) upward and downward flux. The module also calculates chromaticity coordinates using CIE 1931 2° weighting functions.

For all days, the angle (counterclockwise) from the sun to the viewer's direction for the center of the image was 170 degrees for the San Gabriel Mountains view and 234.6 degrees for the downtown Pasadena view. For all days the ground reflectivity was assumed to be 0.15. The angle of the sun above the horizon for June 27, 1988, was 79.2 degrees. The aerosol was assumed to form a uniform haze trapped below the midday inversion base height of 853m (Cassmassi, 1986). The refractive index of the aerosol was assumed to be independent of wavelength. The aerosol was assumed to be an

internal mixture and the refractive index was calculated as a volume-weighted average of the refractive indices of the measured chemical substances in the aerosol. Description of the aerosol as an external mixture also was examined, and in this case results in a negligible change in computed skylight intensities. The residue was assigned a refractive index of  $1.53-0.005i$ . For June 27, the refractive index of the fine particle fraction was calculated to be  $1.55-0.027i$ , and  $1.53-0.011i$  for the coarse particle fraction.

Figure 4.2a shows a comparison of the wavelength dependent skylight intensity as measured with the radiometer and as calculated by the model for the downtown Pasadena view at an angle of 12.5 degrees above the horizon. Linear regression of predicted radiance at 10nm wavelength intervals on radiance values measured at the same intervals shows good agreement with a correlation coefficient ( $r$ ) of 0.95, a slope of 1.04, and an intercept of  $-0.005$  ( $\text{W m}^{-2} \text{ nm}^{-1} \text{ ster}^{-1}$ ). Table 4.2 shows the results of such regression analysis for all six viewing angles studied. Comparison of nephelometer measurements to model predictions shows that the scattering coefficient was slightly underpredicted, although the relative match to the measured distribution of skylight intensities as a function of wavelength was good. The total scattering coefficient was predicted to be  $2.5 \times 10^{-4} \text{ m}^{-1}$  at 460 nm and was measured as  $3.6 \times 10^{-4} \text{ m}^{-1}$  with the nephelometer. The nephelometer measurements were made at a fairly low relative humidity of about  $53 \pm 4\%$  such that alteration of the aerosol water content by the nephelometer is not expected to be a major problem. The disagreement is believed to be due to the fact that some aerosol parameters were measured over a four-hour averaging period rather than at the instantaneous time at which the radiometer measurements and photographs were taken that one would ideally select.

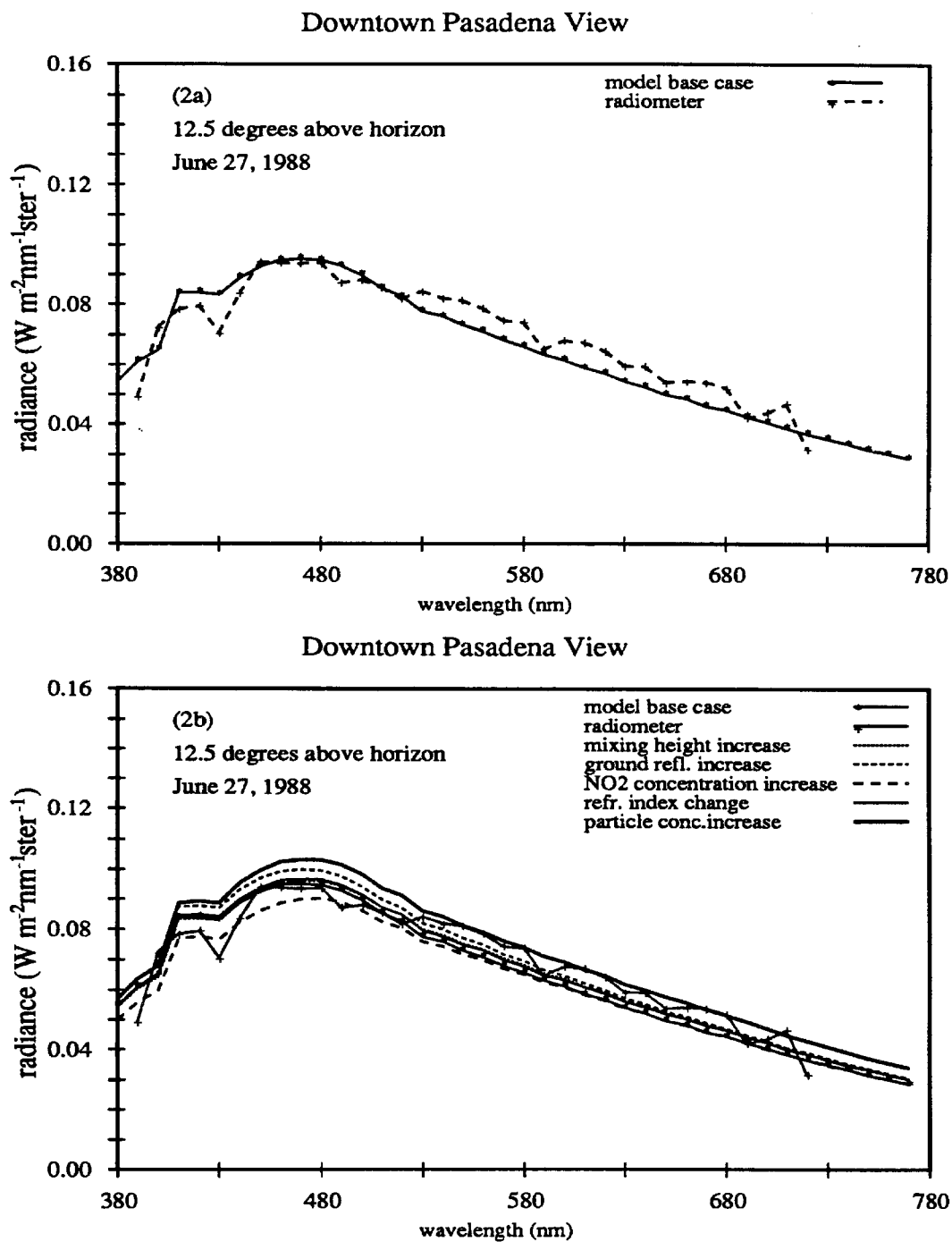


Figure 4.2: Measured and modeled skylight radiance intensity (a) base case calculations; (b) perturbation of input data by the amounts shown in Table 4.1.

Table 4.1: Base Case and Perturbed Inputs to Radiative Transfer Module

| parameter                               | base<br>case          | perturbed             | $b_{scat}$ of<br>perturbed at<br>460 nm ( $m^{-1}$ ) |
|---|-----------------------|-----------------------|--|
| mixing height ( $m$ )                   | 853                   | 950                   | $2.5 \cdot 10^{-4}$                                  |
| ground reflectivity                     | 0.15                  | 0.20                  | $2.5 \cdot 10^{-4}$                                  |
| NO <sub>2</sub> concentration ( $ppm$ ) | 0.06                  | 0.08                  | $2.5 \cdot 10^{-4}$                                  |
| refractive index                        |                       |                       | $2.7 \cdot 10^{-4}$                                  |
| ( <i>fine particles</i> )               | 1.55 - 0.027 <i>i</i> | 1.58 - 0.032 <i>i</i> |  |
| ( <i>coarse particles</i> )             | 1.53 - 0.011 <i>i</i> | 1.36 - 0.002 <i>i</i> |  |
| scale particle concentration            | measured              | 1.4*measured          | $3.4 \cdot 10^{-4}$                                  |

Table 4.2: Comparison of Radiometer Measurements and Model Results <sup>(a)</sup>

$$I_{pred} = \alpha I_{obs} + \beta + \epsilon$$

| view                    | $\alpha$ (std. dev) | $\beta^{(b)}$ (std. dev.) | correlation coefficient |
|-------------------------|---------------------|---------------------------|-------------------------|
| Downtown Pasadena 9.1°  | 1.07 (0.083)        | -0.005 (0.006)            | 0.92                    |
| Downtown Pasadena 12.5° | 1.04 (0.061)        | -0.005 (0.005)            | 0.95                    |
| Downtown Pasadena 16.0° | 1.03 (0.051)        | -0.006 (0.004)            | 0.96                    |
| San Gabriel Moun. 9.3°  | 1.04 (0.078)        | -0.009 (0.006)            | 0.92                    |
| San Gabriel Moun. 13.3° | 1.02 (0.061)        | -0.009 (0.005)            | 0.95                    |
| San Gabriel Moun. 14.9° | 0.98 (0.054)        | -0.003 (0.004)            | 0.95                    |

<sup>(a)</sup> Data are taken at 10 nm intervals over the wavelength range 390nm to 720nm.

<sup>(b)</sup>  $\beta$  has units of  $Wm^{-2}nm^{-1}ster^{-1}$ .

The sensitivity of the visibility model to changes in the inputs also was examined. Each of the input variables was perturbed independently and the response was recorded in the form of wavelength-dependent plots of the predicted skylight intensity, particularly in the wavelength interval from 380 to 710 nm (see Figure 4.2b). It should be noted that in general the difference in predicted intensity between the viewing angles studied is larger than the difference in intensity resulting from parameter perturbation for any one viewing angle. The scattering coefficient was insensitive to the changes made in meteorological parameters and was sensitive to changes in refractive index and number of particles (as expected).

Since we are interested in modeling the visual appearance of a scene, the verification experiment also included the comparison of sky color as measured with the radiometer and as calculated from the computer model. In the CIE (Commission International de l'Eclairage) system, color can be specified by two chromaticity coordinates ( $x, y$ ) and a brightness value ( $Y$ ). This system standardizes the source of illumination and observer, and numerically describes a color viewed under a standard light source by a standard observer. A more detailed description can be found in Billmeyer and Saltzman (1981) or McAdam (1981). Figure 4.3 shows the chromaticity coordinates (1931 CIE) of the sky as measured with the radiometer and as calculated from the aerosol data via the skylight module. In the case where the total aerosol concentration is increased so that the scattering coefficient matches that measured by the nephelometer at the time of the radiometer measurements, and the  $\text{NO}_2$  concentration is increased to the level observed in the first hour of the experiment rather than over the four hour average, the chromaticity coordinates of the skylight model are quite close to those of the radiometer. All

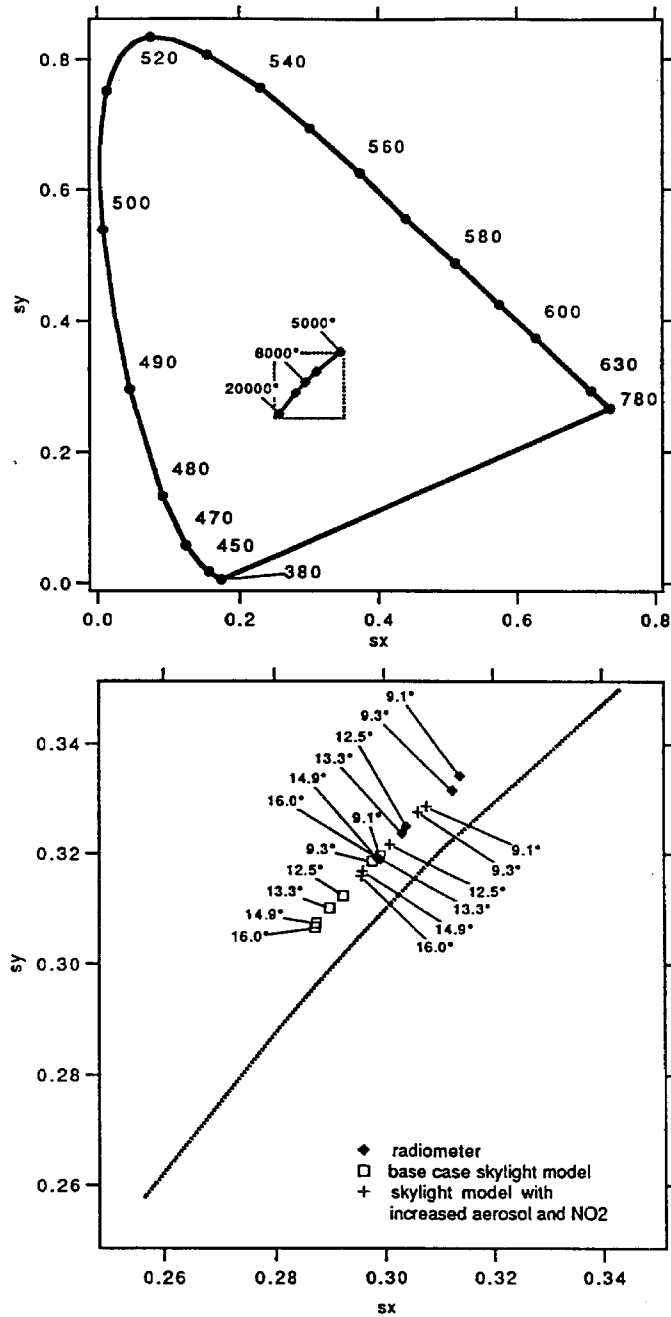


Figure 4.3: (a) 1931 CIE (x,y) – chromaticity diagram with chromaticity coordinates of black body radiators at indicated temperatures (degrees K); (b) chromaticity coordinates of sky at 1200 PST on June 27, 1988; all six viewing angles defined in Table 4.1 are illustrated here.

of the radiometer and skylight model chromaticity coordinates are slightly above the Planckian locus (blackbody radiator curve), and are near to the daylight locus as reported in Wyszecki and Stiles (1982).

#### 4.4 Model Application

The complete image processing based visibility model was employed to transform the clear day April 7, 1983, base photographs into synthetic images of the predicted appearance of the August 25th, 1983, heavy smog event at Pasadena, California.

The skylight module was used to calculate a map of the intensity of radiance of the sky for both clear day and heavy smog conditions based on aerosol,  $\text{NO}_2$  concentrations, relative humidity, and temperature data taken on these days, and that information was transferred to the image processing module. The angle of the sun above the horizon was 62.5 degrees for April 7, 1983, and 67.0 degrees for August 25, 1983. For April 7, the mixing height was 2000 m, and the  $\text{NO}_2$  concentration was 0.04 ppm. The fine particle refractive index was  $1.56 - 0.022i$  and the coarse particle refractive index was  $1.40 - 0.005i$ . The mixing height for August 25 was 1066 m, and the  $\text{NO}_2$  concentration was 0.10 ppm. The refractive index was  $1.53 - 0.042i$  and  $1.42 - 0.001i$  for the fine and coarse particle fractions, respectively. The skylight module calculation was executed with these parameters and with the measured aerosol size distributions.

The skylight module calculations were made for 20 values of the viewing angle above the horizon,  $\theta_v$ , between  $0^\circ$  and  $15^\circ$ , the highest viewer's angle present in the base photographs. These data were then interpolated to form a continuous representation of  $I'_{sky}$  values in the vertical dimension.

Calculations for variations in  $\phi$  (the azimuth angle of the observer's line of sight) showed that the variation calculated from the model was not large enough to result in a significant film density difference from the left edge to the right edge of the image for a constant value of  $\theta_v$ . As a result, the calculations performed at various elevations along the center of the image on the film were used to estimate the light intensities across the image in the horizontal at each viewing elevation. In that manner a predicted skylight intensity map was created for use in the image processing system, and the extinction coefficient was calculated. Distance maps for use with these scenes are described by Larson *et al.* (1988). Then the image processing procedures described earlier were employed to transform the April 7 clear day image into the predicted appearance of the August 25 smog event. Quantitative comparisons now can be made between the predicted appearance and the actual photograph of the August 25 day.

## 4.5 Results

Synthetic photographs of the predicted appearance of the August 25 smog event are shown in Figure 4.1 (c) and (f). The modelled day (August 25, 1983) was sufficiently smoggy that the view of the mountains was obscured. The San Rafael Hills in the downtown Pasadena scene are at a distance of approximately 5 km, and the San Gabriel Mountains in the other scene are at a distance of about 9 km. The predicted appearance of the San Gabriel Mountains scene is quite close to that seen in an actual photograph of the event simulated, with good reproduction of the distance at which objects are first obscured. In the downtown Pasadena scene, the San Rafael Hills are more visible on the left portion of the synthetic photograph than in

the actual photograph, which may be due to the fact that the scattering coefficient modeled from the aerosol properties again is slightly lower than that measured by the nephelometer.

Quantitative comparisons were made between the actual and synthetic images to determine the degree of agreement between predictions and observations. Synthetic images are stored as an array of 2.16 million numerical density (DN) values for each color plane, ranging from 0 (least bright) to 255 (brightest). Histograms of numerical densities for each image were plotted and are presented in Figure 4.4. The effect of the model is clearly evident. Many dark picture elements in the field of view in the clear day photograph are shifted to higher intensities as skylight is added to the line of sight. The expected magnitude of that shift is closely reproduced by the model, as illustrated by the shift in the left edge of the curves shown in Figure 4.4. There is good agreement for all color planes for both views, and the agreement is much better than for the earlier model tested by Larson *et al.* (1988) (see similar figures in that reference). The synthetic image in the blue color plane has slightly higher numerical densities than in the actual smog event photo, but the difference is not large.

In Figure 4.5 contour plots are shown that represent the absolute value of the difference in DN values between the actual and synthetic smog images on a point to point basis after the images have been registered one on top of the other. These figures are useful in examining the performance of the model over the various areas of the image. The largest differences in DN values are found in the near field of view. These differences are explained by the fact that the base day image and the actual image of the day being modeled were taken on different days. Some objects in the near field of view are

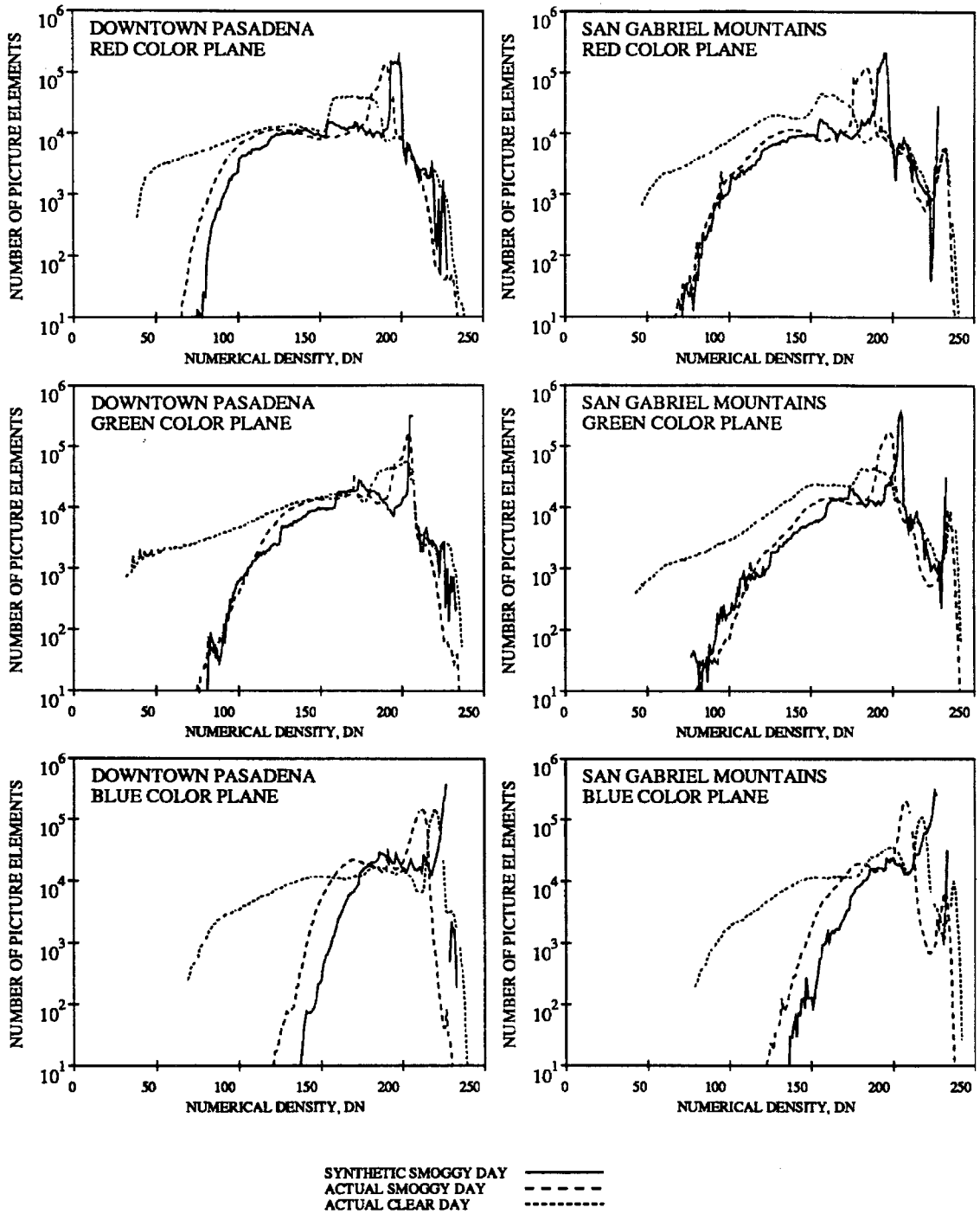


Figure 4.4: Frequency distribution of numerical differences between synthetic and actual images shown in Figure 4.1.

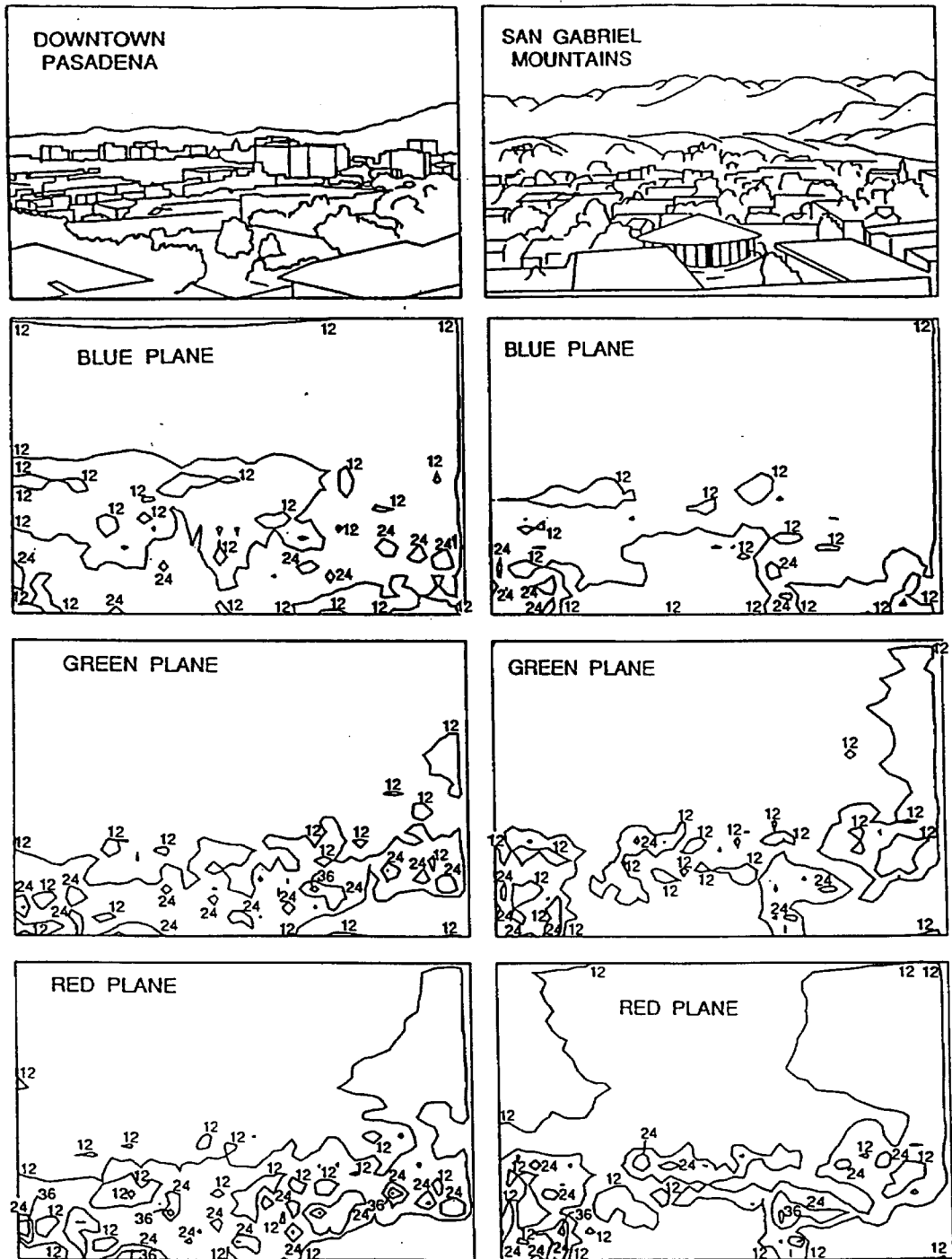


Figure 4.5: Contour diagrams of absolute numerical density differences between synthetic and actual images shown in Figure 4.1.

movable, such as vehicles, or change seasonally, such as individual bushes and trees, and their movement or alteration results in large DN value differences between the two photos in the near field of view. The mid- and far-field DN differences are small. Errors in the sky appear primarily at the edges of the photographs, and are noticeable in Figure 4.5 only because the DN difference values in the red color plane fall almost exactly on the value chosen for the contour interval. No variation with the azimuth angle of the observer was included in the representation of the sky radiance field, as discussed earlier, but test calculations show that this effect is not large enough to produce the observed departure between predicted and photographed sky intensities at the edge of the photograph. The observed error may be due to the known problem of vignetting (fading at the edges) of photographs (Woodleif, 1973).

To examine the photographs in another manner, the average of the absolute value of the differences in DN values between the synthetic and actual smoggy day photos also were calculated as a function of distance from the observer. These graphs are presented in Figure 4.6. For both the San Gabriel Mountains View and the Downtown Pasadena View, the differences between the data sets that describe each color plane follow the same pattern. The blue color plane shows the largest differences, averaging about 16 DN units or 6% of the full dynamic range of 256 DN units. The green color plane shows the smallest differences, generally below 12 DN units. The average differences tend to be the largest at distances of 2 kilometers and 8 to 12 kilometers from the observer.

The improvements offered by this model can be illustrated by comparing the results of this analysis to that of Malm *et al.*'s (1983) model as tested by Larson *et al.* (1988) using the same input data sets, and producing the same

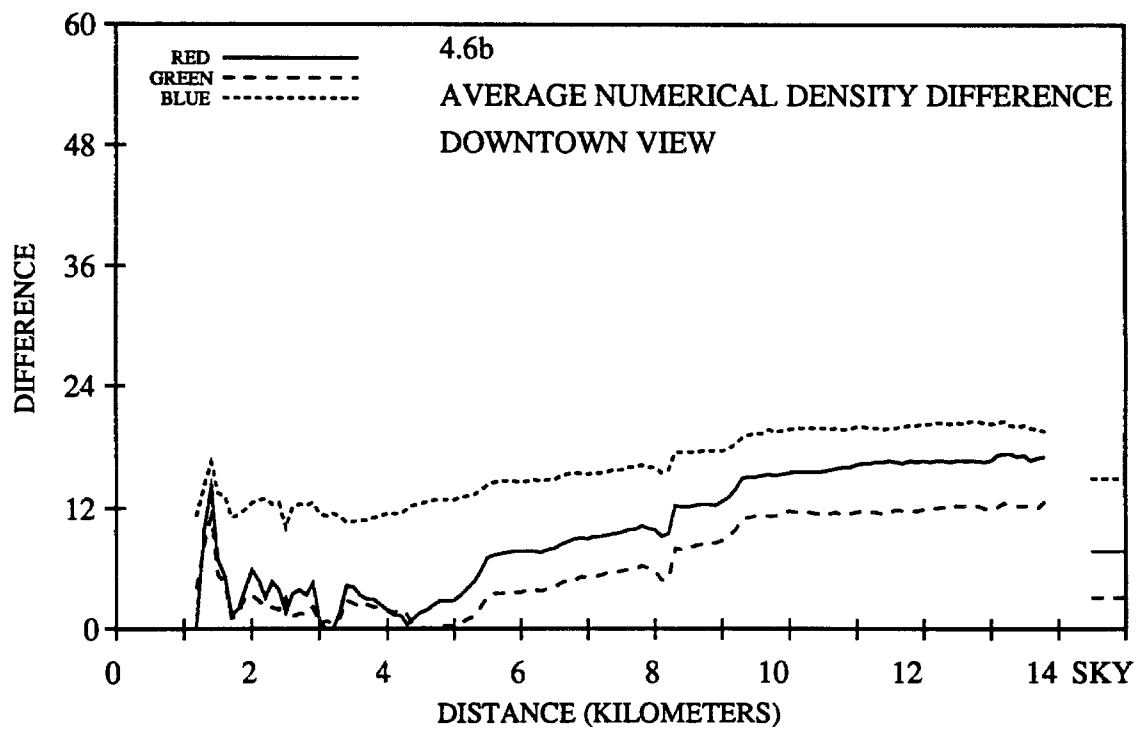
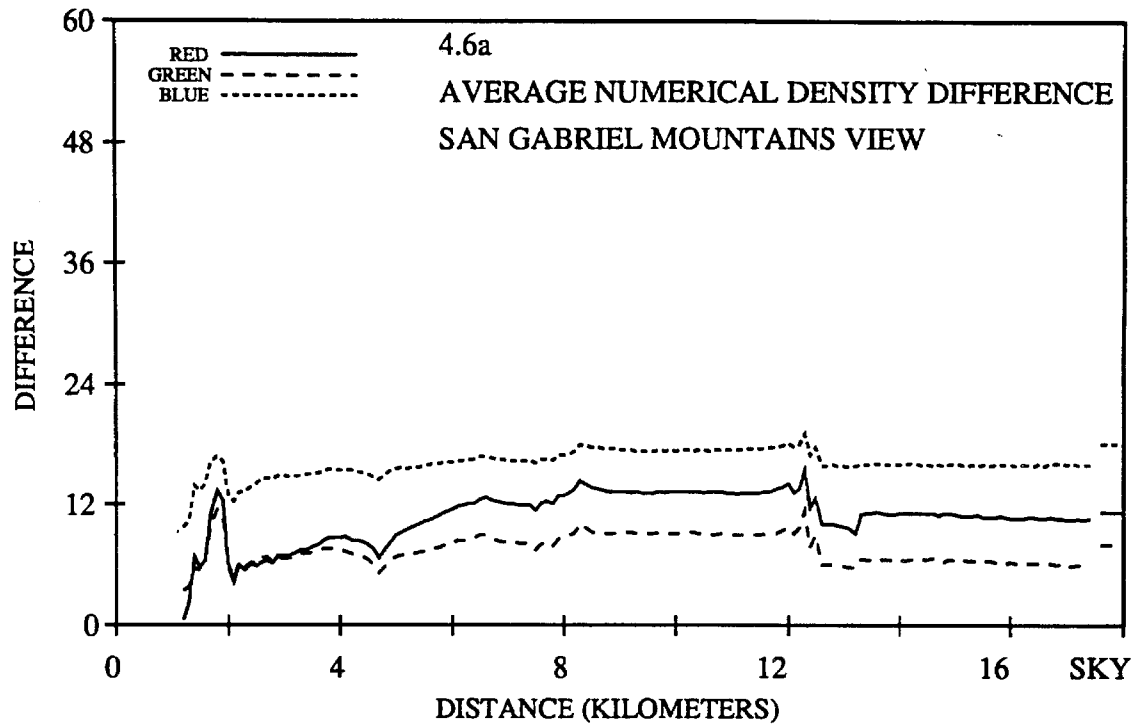


Figure 4.6: Average of the absolute value of the numerical density difference between synthetic and actual images shown in Figure 4.1 as a function of distance from the observer.

histograms, contour plots, and DN difference with distance plots. When comparing the histograms for the blue color plane, we see that the present model represents a significant improvement over the earlier model. In the red and green color planes, the improved model follows the actual image histograms more closely than in the earlier model. When the contour plots of this work are compared to earlier work, the improvement is noticeable. The contours in Figure 4.5 of Larson *et al.* (1988) as well as the contours in the present chapter are drawn at values of 12, 24, 36, 48, and 60 DN units. The contour values showing differences in the sky area of the older model range from 12 to over 36 DN units, while the present model shows DN difference contour values in the sky that are closer to 12 DN units. DN difference contour values for objects in the field of view also are larger for the earlier model because errors in the skylight representation affect the skylight added to the line of sight for objects in the field of view. As can be inferred from the contour plots, the differences in DN values with distance (see Figure 4.6) between the synthetic and actual photographs also are smaller for the improved model. In Larson *et al.*'s (1988) tests of Malm *et al.*'s (1983) model, the difference in DN values between predictions and observations in the blue color plane averages about 36 DN units. In the present model, DN differences between predictions and observations in the blue color plane on average are less than half as large as those produced in the previous model. This improvement in performance in the blue color plane is due entirely to the use of a more accurate theoretical model for skylight color and intensity.

## 4.6 Conclusions

An improved image processing based visibility model has been developed. This model can successfully create synthetic images of the appearance of a scene under heavy smog conditions with a theoretically based light scattering and radiative transfer model used to determine sky color. The model has been validated by comparison against radiometer measurements and against actual photographs of the day being modeled.

This model requires a clear day base photograph and is driven by detailed information concerning the chemical composition and size distribution of the atmospheric aerosol plus data on  $\text{NO}_2$  concentration, relative humidity, temperature, atmospheric mixing depth, and the position of the sun. Detailed mapping of distances between the observer and the objects in the field of view also is required. Because the model provides a direct linkage between pollutant properties and the visual consequences of those pollutant loadings, it could be used in conjunction with models that predict pollutant concentrations to study the effect of alternative pollution control strategies on visibility.

## 5 A Visibility Model Based on Satellite-Generated Landscape Data

### 5.1 Introduction

Light scattering and absorption by airborne particles can lead to pronounced visibility reduction, both in an urban context and in remote wilderness areas. In cities such as Los Angeles and Denver, visibility can be reduced to only a few kilometers by relatively high concentrations of air pollutants (Cass, 1979; Sloane and Groblicki, 1981; Groblicki *et al.*, 1981; Larson and Cass, 1989). In national parks, wilderness areas and other remote parts of the globe, anthropogenic fine aerosols at a concentration of even a fraction of a  $\mu\text{g m}^{-3}$  can shorten visual range by tens of kilometers. Since many of these remote areas are valued for their scenic beauty, even a small level of air pollutant intrusion can lead to noticeable impairment of the scenic resource.

Emission control programs designed to protect or improve regional visibility can be evaluated in a deliberate manner. Mathematical models for atmospheric transport and chemical reaction can be used to calculate the expected changes in aerosol properties that are likely to result from a particular pollution abatement plan (Larson *et al.*, 1989). In order to relate these changes in aerosol properties to effects on visibility, various models for predicting air quality effects on visibility have been developed. These visibility modeling procedures include: (1) statistical models in which the con-

tribution to light extinction by the various pollutant species is inferred by regression analysis based on large sets of observations on fluctuations in the atmospheric extinction coefficient and co-occurring fluctuations in pollutant concentration and chemical composition (White and Roberts, 1977; Cass, 1979; Trijonis, 1979; Groblicki *et al.*, 1981); (2) models based on Mie theory calculations in which the extinction coefficient and standard visual range are calculated from first principles based on the size distribution and refractive index of the atmospheric aerosol, plus data on NO<sub>2</sub> concentrations, temperature, pressure and relative humidity (Ouimette, 1980; Sloane, 1983, 1984b; Larson and Cass, 1989); (3) models in which sky color is calculated theoretically in addition to the extinction coefficient and standard visual range (Sloane, 1988), and (4) models that produce simulated color photographs of the scene of interest in the presence of a specified pollutant concentration and aerosol size/composition distribution (Williams *et al.*, 1980; Malm *et al.*, 1983; Larson *et al.*, 1988; Eldering *et al.*, 1993).

## 5.2 Image Processing-based Visibility Models

Existing models that produce synthetic photographs of the appearance of the scene of interest provide a particularly powerful tool for studying the control of visibility problems. This is because such models permit the visualization of pollutant effects on features in the near-, mid-, and far-field of view, not just the generation of a numerical value for the farthest distance at which a black object can be seen against the horizon sky.

To exercise present models, the size distribution and chemical composition of the atmospheric aerosol, NO<sub>2</sub> concentration, temperature, and relative humidity first are measured on a very clear day. At the same time, a ground-

based photograph of the clear-day appearance of the scene of interest is taken using 35 mm color slide film. Then the base clear day slide is divided into a rectangular array of several million picture elements by scanning the slide through color separation filters using a microdensitometer. A digital representation of the clear day slide is stored on a computer system in the form of arrays of numerical density values ranging from 0 (darkest) to 255 (lightest). Three arrays are stored to provide images in the red, green and blue color planes (see Larson *et al.*, 1988 and Eldering *et al.*, 1993). A distance image giving the distance between the point at which the base photograph was taken and each picture element in the scene also must be created. In the past, this has been done manually by measuring the distance to a few hundred points in the scene, followed by spatial interpolation to estimate distance values to the many points that were not measured.

Next, the numerical density values corresponding to each picture element in the red, green and blue color planes of the base photograph are translated into weighted average light intensity values over the wavelength bands corresponding to each of the three color planes. It is assumed that the objects in the field of view are seen along a near horizontal line of vision through a uniformly mixed atmosphere. The following equation is written separately for each picture element and each color plane to represent the light collected in the red, green, and blue color planes.

$$I(x) = I_0 e^{-\overline{b_{ext}x}} + I_{sky}(1 - e^{-\overline{b_{ext}x}}) \quad (5.1)$$

The  $I(x)$  are weighted average intensity of radiance values averaged over the wavelength band corresponding to one of the three color planes and describe the intensity of light received at the location of the observer from an

object located at distance  $x$  from the observer. The  $I_0$  are weighted average inherent radiance values of the objects in the field of view, averaged over the wavelength band of interest.  $I_{sky}$  is the weighted average radiance of the sky near the horizon over the wavelength band of interest as a function of location in the sky.  $I_{sky}$  is calculated in the model of Eldering *et al.* (1993) using a multiple scattering code for a plane-parallel atmosphere based on the two-stream formulation of Kaufman (1979) and Sloane (1988). The parameter  $\overline{b_{ext}}$  is an effective extinction coefficient for the atmosphere calculated for each wavelength band from the measured airborne particle and gas concentrations.

In previous work with photographs, the array of  $I(x)$  values is measured from the clear day photograph,  $I_{sky}$  and  $\overline{b_{ext}}$  are calculated from the position of the sun and from the air pollutant properties measured on the clear day studied. Given  $I(x)$ ,  $I_{sky}$ ,  $\overline{b_{ext}}$ , and  $x$  for the clear day, equation (5.1) then can be solved for the inherent radiance of the objects,  $I_0$ . Using that array of  $I_0$  values, the light intensities,  $I$ , of the scene at the location of the observer can be recalculated for the case of altered air pollutant concentrations once the new values of  $\overline{b_{ext}}$  have been computed and the radiative transfer model has been solved for the new value of  $I_{sky}$ . The appearance of a photograph of a smog episode can be produced by retranslating the radiance values corresponding to a heavily polluted day into numerical densities and then writing the new image onto photographic film using a film writer.

The accuracy with which this process can be conducted has been studied by Larson *et al.* (1988) and Eldering *et al.* (1993). Synthetic photographs of the predicted appearance of a heavy smog event have been compared to actual photographs of the event being simulated. An example of those results is shown in Figure 5.1c, e, and f where a clear day base photograph of the

San Gabriel Mountains near Pasadena, California (Figure 5.1c) has been used along with air pollutant data to calculate the expected appearance of a particularly heavy smog event at the same location on a different date. The synthetic smog prediction from the image processing-based visibility model is shown in Figure 5.1f and can be compared to an actual photograph of the event being simulated that is reproduced in Figure 5.1e. The appearance of the sky and objects in the scene including buildings, landscape elements and mountains in the distance is reproduced quite accurately by the latest version of such an image processing-based visibility model (Eldering *et al.*, 1993).

Widespread application of image processing-based visibility models at present is retarded by several barriers. First, creation of the necessary distance image by hand is very labor intensive. Months of an analyst's time can be consumed easily while mapping the distance from the camera to the location of hundreds of points in the desired field of view. Any change in the direction of the camera can require a significant effort to re-create the distance image. More subtly, the requirement that a very clear photograph be taken as a base upon which the calculations are performed erects a serious barrier to model use in many of the most important situations. In Los Angeles, for example, very clear days are so rare that a year-long program to measure the aerosol composition and photograph the base scene of interest was needed in order to capture one or two very clear day events during the study of Larson *et al.* (1988).

Figure 5.1: Comparison of alternative visibility models. (a) downward looking Landsat Thematic Mapper (TM) image of the Los Angeles, California area; (b) landscape from TM and elevation data for the San Gabriel Mountains scene; (c) actual clear day photograph taken on April 7, 1983; (d) synthetic clear day image computed on TM landscape; (e) actual smog event photograph taken on August 25, 1983; (f) synthetic smog event image computed by visibility model applied to clear day actual photograph; (g) synthetic smog event image computed on TM landscape.

# Comparison of Alternative Image Processing Based Visibility Models



(a) LANDSAT Thematic Mapper (TM) data



(b) Landscape from TM data



(c) Actual Clear Day Photograph



(d) Synthetic Clear Day



(e) Actual Smoggy Day Photograph



(f) Synthetic Smog on Clear Day Photograph



(g) Synthetic Smog on TM Landscape



### 5.3 A New Model: Conceptual Framework

A very clear representation of distant topographic features can be taken by a horizontally-oriented, ground-based camera only under very clear sky conditions. This is because the scene must be viewed through up to several hundred kilometers of atmosphere containing gases and particles that scatter and/or absorb light. In the absence of cloud cover, a clear-day image is readily obtained by satellites in earth orbit because they view the scene through the equivalent of only a few km of atmospheric gases; the urban anthropogenic haze layer is even thinner (geometrically) when viewed from above, a distance of about 1 km or less in the case of the Los Angeles area atmosphere.

An image processing-based visibility model has been developed to take advantage of this situation. Landsat Thematic Mapper (TM) data are acquired in the form of a downward-looking satellite view of the area of interest. The geographic features recorded by the downward-looking satellite are coordinated with U.S. Geological Survey (USGS) data on ground elevation. The numerical representation of the satellite image is rotated until a perspective view of the terrain of interest is created as it would be seen by a ground-based observer looking horizontally. The distance image needed for visibility model calculations is generated automatically from the digital terrain data set, knowing the chosen location of the observer. Unlike the situation faced by a ground-based photographer, the “observer” can be placed at any desired location. Under clear atmospheric conditions, light scattering by air molecules is used to compute sky color, and the visibility model of Eldering *et al.* (1993) is used to predict the effects of skylight on the appearance of the surrounding topography. The effect of atmospheric smog aerosols on the

visual qualities of the scene next is calculated from the size distribution and refractive index of the airborne particles. Results are displayed as a synthetic photograph of the predicted appearance of the scene of interest in the presence of the specified level of air pollution.

## 5.4 Application

The satellite-based visibility model was tested by application to data taken in the Los Angeles, California, area. Two scenes visible from the campus of the California Institute of Technology (Caltech) in Pasadena, California, will be examined. An actual color photograph of the first scene as originally recorded on Kodachrome 25 color slide film is shown in Figure 5.1c. This vista will be referred to as the San Gabriel Mountains scene. It is a north-looking view from the roof of Caltech's nine story Millikan Library, taken at the beginning of April, 1983, with the San Gabriel Mountains in the background at a distance of about 6 kilometers, and with Caltech's Beckman Auditorium in view in the foreground (large, round, white building). The second scene examined is referred to as the Downtown Pasadena view. Actual photographs of that scene are reproduced by Larson *et al.* (1988) and by Eldering *et al.* (1993). It is a westward looking view with the commercial center of the City of Pasadena in the near and mid-field of view and with the low range of the San Rafael Hills in the background at a distance of 5 kilometers. These scenes are chosen because the results from two prior photograph-based visibility modeling studies of these scenes are available against which the results of the new satellite-based model can be compared quantitatively.

The first step in the modeling process is to create synthetic landscape images from satellite observations that represent these two scenes under clear

day conditions. Towards that goal, Landsat Thematic Mapper (TM) data were acquired as a downward looking image of Southern California collected on July 3, 1985.

Image processing-based visibility models represent light intensities and colors by a triplet of red, green, and blue (RGB) numerical density (DN) values assigned to each picture element. Previous models obtained their RGB DN values by scanning a clear day image of the scene recorded on color photographic slide film using a microdensitometer. The Landsat Thematic Mapper collects information at wavelengths that differ from the wavelength bands that form the light-sensitive emulsion layers of the color slide film upon which previous image processing-based visibility models have been formulated, and the TM data generally are coded in a narrow range of numerical densities. The TM data are dominated by blues, giving the overall scene a purple hue. To transform TM data into false color images, the TM data must be "stretched." A stretch consists of a reassignment of numerical density values within each of the red, green, and blue color planes such that the data span a different range of DN values while maintaining the rank-ordering of the DN values assigned to each picture element in each color plane. Stretches may be simple arithmetic transformations, or more complicated formulas that result in desired distributions of DN values. In the present work a Gaussian stretch has been used that seeks to approximate a histogram of the frequency of occurrence of DN values in each color plane that has a Gaussian distribution with a specified mean and standard deviation. For this work a Gaussian distribution was selected that has a mean equal to the average of the maximum and minimum numerical density values (DNMAX and DNMIN, respectively) of the raw TM data, and a standard

deviation equal to  $(DNMAX - DNMIN + 1)/4.8$ . Many alternative stretch procedures tested result in a loss of detail due to the number of picture elements assigned to very high or very low DN values. The advantage of the Gaussian stretch is that it does not saturate the images in the extremely light or dark areas of the image, and it is a general statistical transformation. No other transformation tested in this work provided a better approximation of the desired characteristics for the raw data.

The transformed downward looking TM image over the Los Angeles basin is shown in Figure 5.1a. These TM data were aligned with USGS topographic data for the same geographical region, and the data were rotated to create the necessary perspective views of the San Gabriel Mountains scene (shown in Figure 5.1b) and the Downtown Pasadena scene. At this stage the landscape appears like that of a planet with no atmosphere: the sky is black and the dry, dirt-covered San Gabriel Mountains are brown (as they indeed appear at very close range). Large buildings in the near field of view, such as Beckman Auditorium, are not resolved because of the coarse spatial resolution of the Landsat data, and because of the lack of building elevation data. Higher resolution data are within the reach of present military technology; so this limitation to the present application is not inherent in the underlying method.

The distance from the hypothetical observer to each picture element in both scenes of interest was computed from the digital terrain elevation data. The resultant distance image needed by the visibility model is of much higher quality than the prior distance images used by Larson *et al.* (1988) and Eldering *et al.* (1993) that were created through interpolation of hand-measured distances to a few hundred points in each scene.

Next the image processing-based visibility model described by Eldering

*et al.* (1993) is used to compute the predicted appearance of the transformed TM landscape of interest under nearly clear sky conditions. The atmospheric particle size distribution and refractive index are known experimentally for the time that the clear-day photograph of Figure 5.1c was taken, along with the atmospheric NO<sub>2</sub> concentration and data sufficient to determine atmospheric density (Larson *et al.*, 1988). These data were supplied to the image processing-based visibility model described by Eldering *et al.* (1993) along with the TM landscape image. A model for multiple scattering in a plane parallel atmosphere was used to compute the intensity and spectral distribution of skylight as a function of position in the sky (Kaufman, 1979; Sloane, 1988), and the visibility model was exercised to compute the effect of skylight addition on the objects in the field of view. The result is shown in Figure 5.1d in the form of a synthetic image of the particular clear day conditions of interest computed from the skyless TM landscape of Figure 5.1b. The sky in Figure 5.1d is now blue and the mountains appear blue-green in the background.

Finally, the modeling procedure was tested under heavy smog conditions. The aerosol size distribution, refractive index, NO<sub>2</sub> concentration and atmospheric density corresponding to the heavy smog episode of August 27, 1983, shown in Figure 5.1e were supplied to the new model. The predicted appearance of the heavy smog episode is shown in Figure 5.1g based on the satellite-generated topographic background, and can be compared to an actual photograph of the event modeled in Figure 5.1e and to the results of the same visibility modeling calculations applied to the clear day base photograph in Figure 5.1f. As long as the differences arising from the inability of the present Landsat data to resolve buildings and trees in the near field

of view is disregarded, all three images are very similar. The mountains are completely obscured and the distance at which objects begin to disappear into the haze layer is nearly the same in all three images. In the actual photograph of the heavy smog event (Figure 5.1e), the only object visible within the generally opaque portion of the haze layer of the San Gabriel Mountains scene is the bright side of a large, white building located about 55% of the distance from the observer to the base of the mountains. That white building shows through the haze in the smoggy day simulation that began with the clear day actual photograph (Figure 5.1f), and it can be seen in the satellite-based model result for the heavy smog event depicted in Figure 5.1g as well.

The calculations based on the TM landscape are better than those previously reported for calculations that begin from an actual clear day ground-based photograph in one respect. The new automated distance image is smoother and more accurate, which eliminates some “scalping” of the haze layer that appeared in earlier work like that of Figure 5.1f due to the zone of influence of the interpolation calculations around sparse distance measurements used in previously available distance images.

## 5.5 Evaluation of Model Performance

A number of quantitative tests of the performance of image processing-based visibility models have been employed in previous work to evaluate the accuracy with which air pollutant effects on the appearance of a photograph can be predicted. These tests include (1) comparisons of predicted and measured skylight radiance intensity, (2) comparison of measured and predicted sky color, (3) comparisons of the frequency distributions of the DN values for

synthetic versus actual images, (4) contour diagrams showing the absolute numerical density difference between synthetic and actual photographs of a scene as a function of position, and (5) graphs of the absolute numerical density differences between synthetic and actual photographs as a function of distance from the observer. The skylight intensity and color calculations in the present model are identical to those evaluated previously by Eldering *et al.* (1993). Therefore, further tests of model performance for the case of the model employing satellite-generated topography will focus on items (3)–(5) above.

The frequency distribution of numerical density values for actual photographs of the clear day and smog event scenes and for clear day and smog event scenes synthesized from the satellite-based model are shown in Figures 5.2 and 5.3 for the San Gabriel Mountains and Downtown Pasadena scenes, respectively. For the case of the heavy smog event, earlier model predictions (Eldering *et al.*, 1993) obtained by starting from the clear day actual photographs also are shown in those figures. Because the actual photographs and satellite images differ in certain technical attributes, two additional processing steps are required to create the comparisons shown in Figures 5.2 and 5.3. First, the number of picture elements appearing in both images must be equalized. The ground-based photographs were scanned as an array of 1200 by 1800 picture elements and the satellite-based images contain an array of 400 by 600 picture elements. The satellite image data thus have been rescaled to approximate a number of picture elements equal to that in the actual photographs, thus making the histograms easier to compare. Second, adjustment must be made for the fact that not all DN values are employed in the satellite-generated base photograph of Figures 5.1a and 5.1b. As pre-

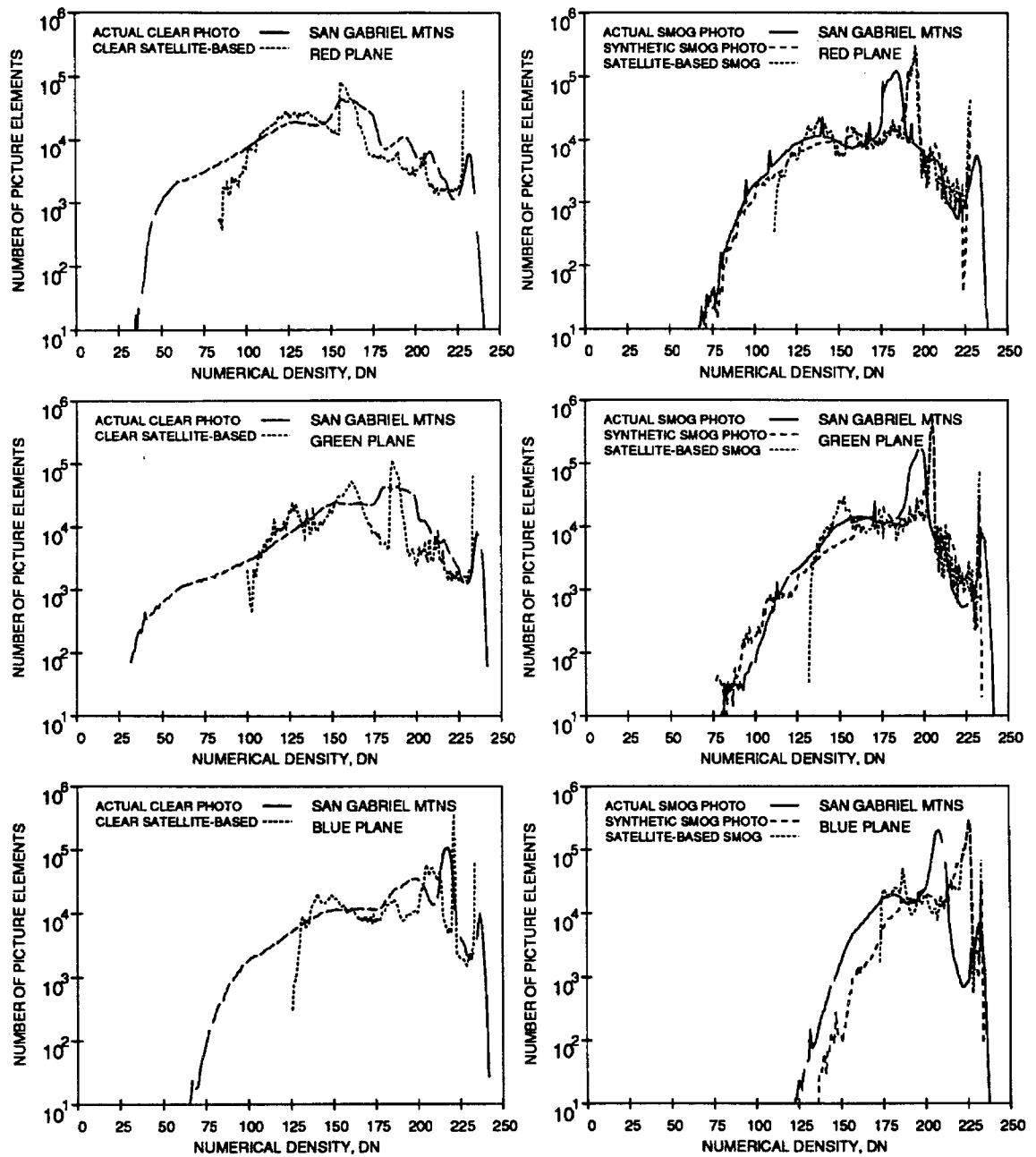


Figure 5.2: Frequency distribution of numerical differences between synthetic and actual images of the San Gabriel Mountains scene shown in Figure 5.1.

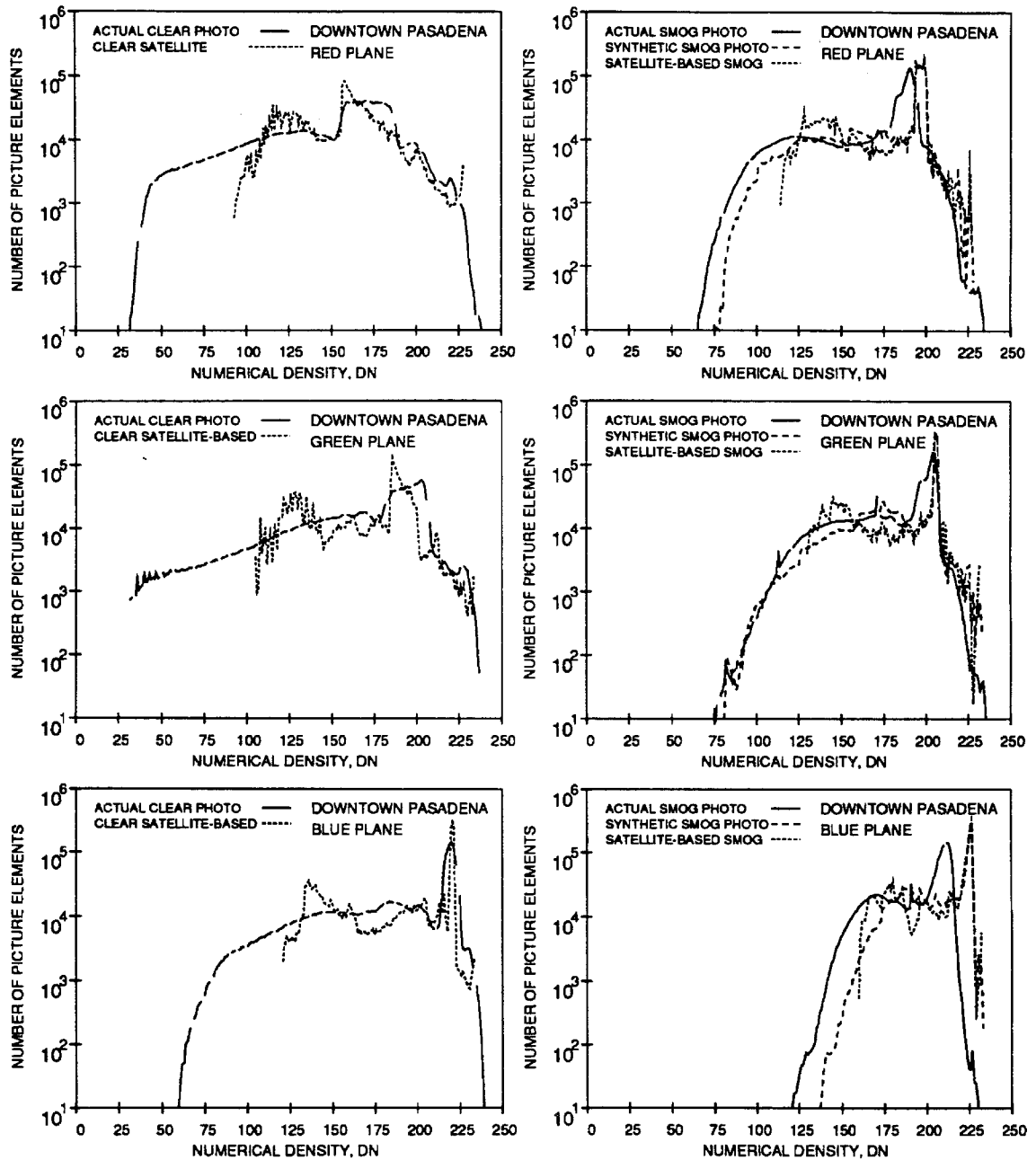


Figure 5.3: Frequency distribution of numerical differences between synthetic and actual images of the Downtown Pasadena scene shown in Figure 4.1.

viously mentioned, the original Landsat TM images are coded in a narrow band of DN values that had to be stretched to create false color images. This stretching process opens gaps in the consecutive sequence of DN values with some DN values not used. A histogram showing the frequency of occurrence of DN values in the satellite base image drawn in terms of consecutive DN values thus appears to be rough, with some DN values appearing more frequently than would be the case in a true color photograph, and other immediately adjacent values not appearing at all. To smooth the histogram, while introducing a nearly unnoticeable reduction in sharpness in the photograph, a simple filter was applied to the satellite image. Each DN values assigned to each picture element was weighted as 80% of its original value plus 20% of the average of the DN values of the eight adjacent picture elements. This was applied only to the clear day satellite-based images for production of the histograms; the photographs in Figure 5.1, and the data in Figures 5.4 and 5.5 that follow were not smoothed. The skylight addition calculation for the heavy smog event provided sufficient smoothing in that case, and thus the filter is only applied to the clear day image prior to drawing the histograms of Figures 5.2 and 5.3.

If the synthetic images were to exactly match the photographs, the histograms of Figures 5.2 and 5.3 would completely overlap. The histograms do not match exactly, but they agree very well. For the clear day images of both scenes, we see that the TM-derived images do not contain data in the lowest (darkest) DN range, but in the range 125 to 255 DN units, the histograms match well. The DN values that represent the clear day sky (the tall hump near 220 DN units in the blue plane, between 180 and 210 units in the green plane, and between 150 and 190 DN units in the red plane) have

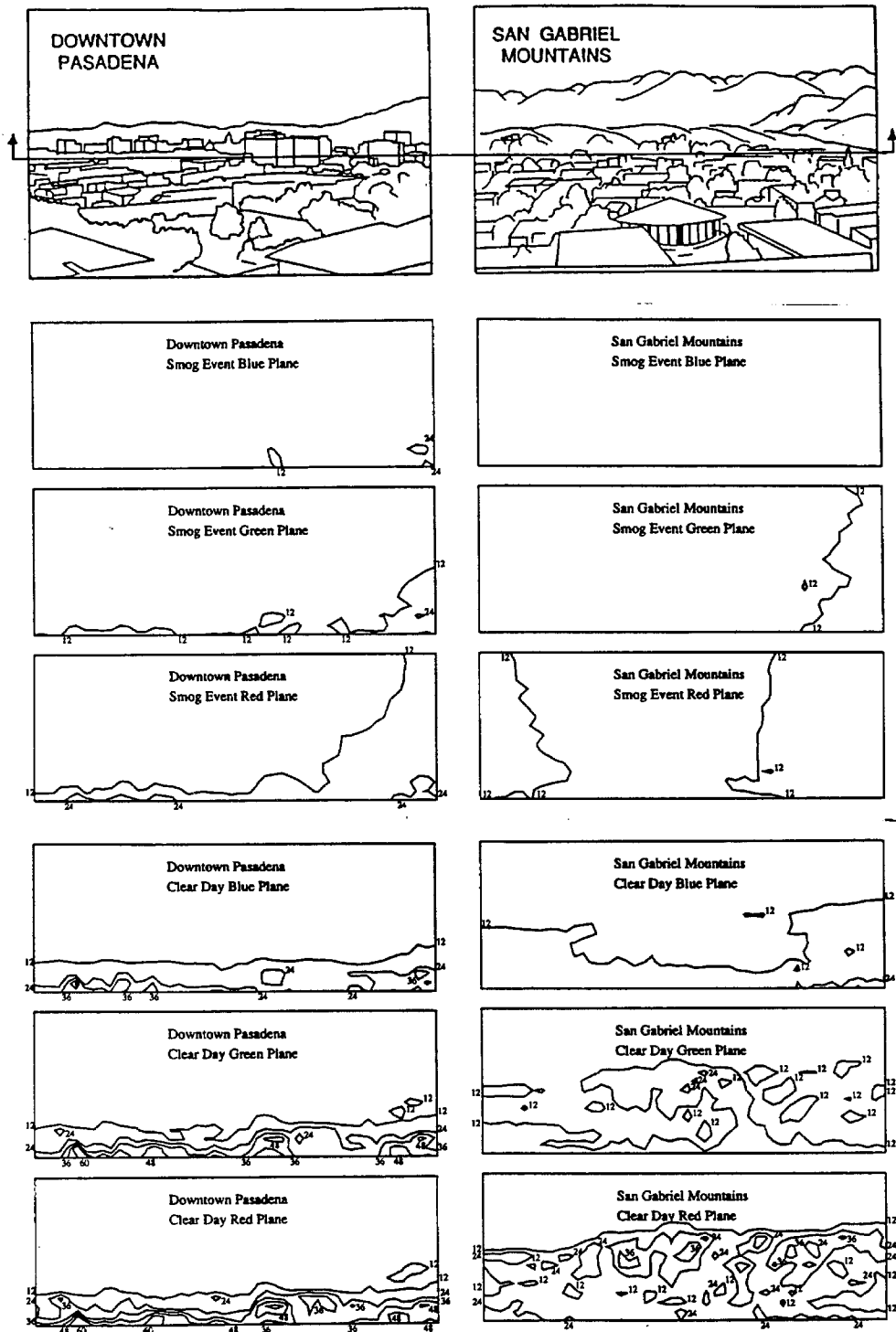


Figure 5.4: Contour diagrams of the absolute numerical density differences between the satellite-based synthetic photographs and the actual photographs of the clear day and the heavy smog event. Contour diagrams are given for the upper portion of each image; that is the portion above the section line shown in the sketches of each scene at the top of the figure.

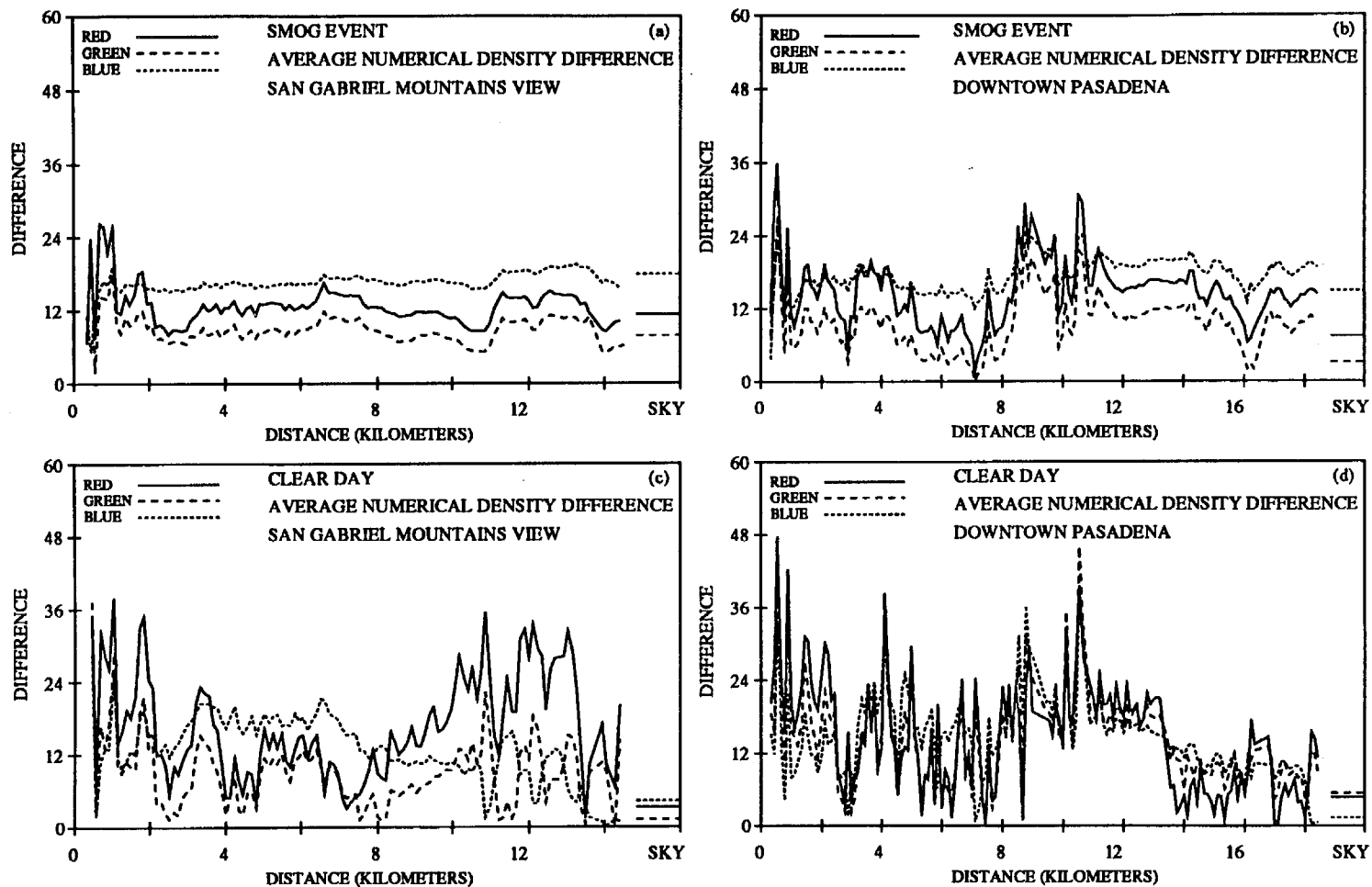


Figure 5.5: Average of the absolute value of the numerical density difference between actual and satellite--based synthetic photographs as a function of distance from the observer: (a) San Gabriel Mountains scene, smog event; (b) Downtown Pasadena scene, smog event; (c) San Gabriel Mountains scene, clear day; (d) Downtown Pasadena scene, clear day.

a slightly smaller range in the TM images than in the actual photographs. For the smog event images, the distribution of DN values for the satellite-based synthetic images and clear day photograph-based synthetic images are quite similar, and they both match the histograms drawn from an actual photograph of the smog event being simulated quite well. Examination of DN distribution histograms for particular portions of both the clear day and smoggy day images shows that the discrepancies occur mostly in the foreground area (portions of the image less than 4 km from the observer). One would expect the foreground areas to differ somewhat, since the TM image does not represent urban buildings, automobiles, and individual trees well.

Contour plots that represent the absolute value of the difference between numerical densities (DN) of the actual photographs and satellite-based images as a function of location in the images are shown in Figure 5.4. These contour plots show only the upper portion of the images (i.e., that above the section line in the sketches of the scenes at the top of Figure 5.4), as the urban foreground is not comparable. Contours are drawn at increments of 12 DN units, where 12 DN units represent less than 5% of the full dynamic range of 256 units used by the image processing system. The sky portions of the images have very low numerical density differences. For the smoggy days, when the mountains and some buildings are obscured by the smog, the overall numerical differences are quite small throughout the entire portion of each color plane. In the case of the clear day simulation, the blue color plane is reproduced very well throughout the whole image in both scenes. The green color planes in both images generally are well matched, with the major differences occurring in an area of hillside in the center of the San Gabriel Mountains scene that was more recently burned over by the Pine Crest Drive

Fire of 1979 (Hawkins, 1993) at the time of the 1983 actual clear day photograph than at the time of the later 1985 Landsat TM image. The red planes of the clear day images differ more noticeably, and again the largest differences in the San Gabriel Mountains scene may arise from regrowth of vegetation on burned hillsides between 1983 and 1985.

It is also useful to look at the numerical density differences as a function of the distance from the observer. For this analysis, the absolute average numerical density difference between the actual photograph and the synthetic image is calculated for all picture elements that fall into consecutive 10 m distance increments. Figure 5.5 shows the results of this analysis for the heavy smog event and for the clear day simulation. For the heavy smog event day, the absolute values of the DN differences in the mid- and far-field are quite small (about 12 DN units or 5% of full scale in the green color plane; a little less in the red; a little more in the blue), with the very near field (less than 2 km) differences being somewhat larger. For the San Gabriel Mountains scene (see Figure 5.5a), the graph of DN differences as a function of distance generated when using the satellite model is almost identical to the same comparison reported for the prior model in which the smog event calculation begins from a clear day actual ground-based color photograph. (Compare Figure 5.5a of the present chapter to Figure 6a of Elderling *et al.*, 1993.) For the clear day images (Figures 5.5c and 5.5d), higher numerical density differences exist in the foreground of the synthetic images because those images lack the buildings and the other urban landscape elements present in the actual photograph. For the Downtown Pasadena scene, the majority of the image is less than 7 km from the observer. The range of hills behind the downtown core of the city begin at a distance of

5 km from the observer and extend to about 17 km distance. The natural landscape elements (e.g., the nearest hillsides at 5 to 8 km distance and the farthest hills at 14 to 17 km distance) present in the Downtown Pasadena clear day simulations are reproduced quite accurately, as is the clear day sky. In the case of the San Gabriel Mountains scene, the color and intensity of the clear day sky again is calculated quite closely. While the numerical density difference plots for the San Gabriel Mountains view are more irregular for the clear day than for the smog event, the average values of these differences (e.g., the bias in the model) is about the same in both the clear day and smog event cases. The exception to this is that larger differences exist between the red color planes of the actual photograph and the satellite based simulation at distances corresponding to the mountainside (8 km to 14 km distance). As mentioned previously, this is believed to be due to the two additional years of vegetation regrowth following a hillside fire that distinguishes the 1983 clear day photograph from the 1985 Landsat TM data.

## 5.6 Conclusions

A visibility model has been developed based on satellite and topographic images that creates synthetic photographs of the appearance of the scene of interest in the presence of specified levels of air pollution. Light extinction and sky color are calculated from data on the aerosol size distribution,  $\text{NO}_2$  concentration, temperature and relative humidity. The synthetic images created depict natural landscape elements such as hillsides and sky color that are very similar in appearance and color to actual photographs taken on the days modeled. The model is suitable at present for evaluating visibility-related phenomena in rural settings such as wilderness areas and national

parks. The Landsat TM data and USGS topographic data used with the present model application do not provide enough spatial resolution to accurately depict air pollution effects on the appearance of urban landscapes, because single buildings cannot be resolved. However, if data from satellites with higher resolution imaging systems and altimeters were made available, then urban landscapes could be depicted.

Since the model operates from satellite observations that are available over the surface of most of the earth, and uses standard data transformations, it is possible to apply this model on a global scale. Data on terrain features can be taken from satellites in orbit around other planets. Therefore, it should be possible to use this method to depict the appearance of landscapes as they would be seen through other planetary atmospheres.

## 6 Conclusions

### 6.1 Summary of Results

Four mathematical models, representing three distinct methods for predicting air pollution and its effects on visual range and the appearance of a scene, have been presented. These models have been verified against data collected during the 1987 Southern California Air Quality Study (SCAQS) and against data taken from photographs of the scenes that were modeled.

The first visibility model examined was one intended for use in translating atmospheric aerosol size distribution information collected by continuous air monitoring networks into estimates of visual range. The model operated by applying Mie theory light scattering and absorption calculations to atmospheric particle size distribution data taken continuously by electrical aerosol analyzers and optical particle counters, along with filter-based samples from which the aerosol chemical composition and refractive index can be determined. The model was tested against data taken during the Southern California Air Quality Study (SCAQS). It was found that the data collected during the SCAQS experiment were of sufficient quality to support such calculations. The measured light extinction coefficient was reproduced well by Mie theory calculations, although the instrumentation used tended to dry the aerosol, and nephelometer readings were found to be sensitive to instrument maintenance practices. When visual range predicted by the model was compared to visual range observations made by human observers at nearby

airports, good agreement was found. In two cases where airport human observer visual range estimates were not in good agreement with model predictions, the nephelometer measurements of the light scattering coefficient and model predictions of the light scattering coefficient are in agreement, suggesting that the lack of agreement in visual range is due to spatial inhomogeneities in air pollutant levels between the airport and the location of the SCAQS measurements. It is concluded that continuous air monitoring networks can be built and operated in which continuous measurements of the aerosol size distribution are used to supply data to mathematical models that in turn can predict visual range.

The second visibility model assembled is one that translates air pollutant emissions from sources into estimates of visual range at locations downwind from the sources. A Lagrangian trajectory air quality model is supplied with data on the size distribution and chemical composition of primary particle emissions from sources along with gaseous pollutant emissions. Condensible species produced by gas-phase chemical reactions cause the primary particles to grow in size and change in composition as gas-to-particle conversion processes proceed in the atmosphere. Sulfur dioxide oxidation in fogs is simulated along with dry deposition processes. Resulting predictions of the aerosol size distribution and chemical composition at downwind locations are translated into estimated visual range estimates via Mie theory and Koschmieder's formula.

In the course of testing the source-oriented visibility model, procedures were developed that characterize the size distribution and chemical composition of primary particle emissions from sources. This is a critical step in such a model because these primary particles form the seed aerosol upon which

later gas-to-particle conversion processes occur, thereby shaping the ultimate particle size distribution. When the aerosol emissions data developed during the present work were compared to previous governmental emissions inventories for Southern California, very large errors in the governmental inventories were found and corrected.

The source-oriented visibility model was tested by examining air parcels traveling across Southern California, arriving at Claremont, California, on August 28, 1987. The trajectory-based visibility model successfully predicts the fine and coarse aerosol mass, as well as the size distribution of individual chemical species in the particle phase. The overall aerosol size distributions predicted by this model capture the features of the observed aerosol size distributions. Model predictions of particle light scattering coefficient values are also in good agreement with observations. It is concluded that air pollutant emissions from a complex industrial and urbanized region can be related directly to downwind visual range via a mechanistic model for aerosol processes combined with light scattering calculations. The importance of this development is that it provides a means for assessing the effect of proposed emission controls on visibility in advance of the adoption of such control programs.

Two technical challenges were addressed and overcome in order to improve and extend a visibility model that produces photograph-like images of the effects of smog on the appearance of a scene. The first accomplishment was the development of a method that relates a solution of the radiative transfer equation, that provides theoretical predictions of light intensity at points in the sky, to the intensity of light as recorded on photographic film. In doing so, it was shown that the color of the sky, as described in CIE color coordinates, could be predicted accurately by solving the radiative transfer

equation. Additionally, an image could be produced that accurately depicted the effect of smog on the appearance of a scene. Point by point comparison of actual photographs and the synthetic image showed only small differences between the images. The importance of this development is that an accurate method now is available for communicating complex and subtle changes in the appearance of a scene that would result from changes in air pollutant concentrations.

The photograph based image processing visibility model has some limitations, namely, the need to begin calculations from data extracted from a clear day base photograph of the scene of interest and the need for a map of the distance from the observer to all, or at least a few thousand points in the image (a distance map). The opportunity to take a clear day photograph can be rare, as in Los Angeles, and a change in the location of the observer requires a large investment of time to recalculate the distance map. A model was developed that relies on Landsat Thematic Mapper (TM) data and US Geological Survey terrain elevation data to create a base image of the terrain as seen by a ground-based observer. At the same time, a detailed map can be created automatically that states the distance from the observer to all points in the field of view. When light scattering by air molecules was interposed between the observer and the scene, an image very similar to a clear day base photograph of the same scene was produced. An image showing the effects of smog on the appearance of the scene was also created by adding the extra light scattered and absorbed by pollutant particles and gases. This technique provided great flexibility because Landsat TM data, which are used to create the base image, are available over most of the earth.

## 6.2 Recommendations for Future Research

The extension of the Caltech trajectory model has resulted in a model that has the capability of treating particles from different emission sources as if they have different properties such as chemical composition and wettability. Experimental evidence suggests that aerosol particles are externally mixed, meaning that particles of the same size frequently have different chemical composition. Thus, it would be desirable to utilize this trajectory model to explore the influence of an external mixture on the size distribution, chemical composition, and light scattering properties of an ambient aerosol.

The models developed here are well suited to the task of evaluating control strategies for the abatement of particulate matter air pollution. It has been demonstrated that the trajectory model can predict the observed levels of light scattering. The next logical step would be to modify the emissions inventory according to planned emissions controls, exercise the model, and produce data and images describing the level of light scattering and the possible appearance of scenes of interest in the presence of future emission controls.

## Bibliography

- [1] Allen, P. D. (1992) Modeling emissions data system. Personal communication of data to Annmarie Eldering from the Technical Support Division, California Air Resources Board, Sacramento, California.
- [2] Appel, B. R., Wall, S. M., Tokiwa, Y., and Haik, M. (1980) Simultaneous nitric acid, particulate nitrate and acidity measurements in ambient air. *Atmos. Environ.*, **14**, 549–554.
- [3] Billmeyer, F. W. and Saltzman, M. (1981) *Principles of Color Technology*. John Wiley and Sons, second edition, 34–60.
- [4] Blumenthal, D. L., Watson, J., and Lawson, D. (1986) *Southern California Air Quality Study Suggested Program Plan*. California Air Resources Board, Sacramento, California.
- [5] Carter, W. P. L. (1990) A detailed mechanism for the gas-phase atmospheric reactions of organic compounds. *Atmos. Environ.*, **24A**, 481–518.
- [6] Cass, G. R. (1976) *On the Relationship Between Sulfate Air Quality and Visibility in Los Angeles*. Environmental Quality Laboratory Memorandum 18, California Institute of Technology.
- [7] Cass, G. R. (1979) On the relationship between sulfate air quality and visibility with examples in Los Angeles. *Atmos. Environ.*, **13**, 1069–1084.
- [8] Cassmassi, J. (1988) Personal communication, South Coast Air Qual-

ity Management District.

- [9] Chan, M. and Durkee, K. (1989) *Southern California Air Quality Study B-Site Operations*. California Air Resources Board contract A5-196-32, Aerovironment, Inc., Monrovia, California.
- [10] Chandrasekhar, S. (1960) *Radiative Transfer*, Dover Publications, New York, New York, first edition. 9-18.
- [11] Chang, E., Nolan, K., Dais, M., Chico, T., Chan, S., and Pang, E. (1991) *Final Appendix III-A, 1987 Emissions Inventory for the South Coast Air Basin: Average Annual Day*. South Coast Air Quality Management District, Diamond Bar, California.
- [12] Christoforou, C. (1993) Personal communication of data to Annmarie Eldering from the Environmental Quality Laboratory, California Institute of Technology.
- [13] Coakley, J. A. and Chylek, P. (1975) The two-stream approximation in radiative transfer: including the angle of incident radiation. *J. Atmos. Sci.*, **32**, 409-418.
- [14] Cooper, J. A., Redline, D. C., Sherman, J. R., Valdovinos, L. M., Scavone, L. C., and Badgett-West, C. (1989) *Final Appendix V-G, PM10 Source Composition Library for the South Coast Air Basin*. South Coast Air Quality Management District, Diamond Bar, California.
- [15] Dave, J. V. and Canosa, J. (1974) A direct solution of the radiative transfer equation: application to atmospheric models with arbitrary vertical inhomogeneities. *J. Atmos. Sci.*, **31**, 1089-1101.
- [16] Eldering, A., Cass, G. R., and Moon, K. C. (1994) An air monitoring network using continuous size distribution monitors: connecting pollutant properties to visibility via Mie scattering calculations. *Atmos.*

*Environ.*, **Part A**, in press.

- [17] Eldering, A., Larson, S. M., Hall, J. R., Hussey, K. J., and Cass, G. R. (1993) Development of an improved image processing based visibility model. *Environ. Sci. Technol.*, **27**, 626–635.
- [18] Eldering, A., Solomon, P. A., Salmon, L. G., Fall, T., and Cass, G. R. (1991) Hydrochloric acid: A regional perspective on concentrations and formation in the atmosphere of Southern California. *Atmos. Environ.*, **25A**, 2091–2102.
- [19] Englehart, P. J. and Muleski, G. E. (1991) *Final Technical Report III-F, Inventory of PM10 Emissions from Fugitive Dust Sources in the South Coast Air Basin*. South Coast Air Quality Management District, Diamond Bar, California.
- [20] Erel, Y., Pehkonen, S. O., and Hoffmann, M. R. (1993) Redox chemistry of iron in fog and stratus clouds. *J. Geophys. Res.*, **98**, 18423–18434.
- [21] Ferguson, B., editor (1980) *KODAK Color Films*. Eastman Kodak Company, Rochester, New York.
- [22] Fitz, D., Chan, M., Cass, G. R., Lawson, D., and Ashbaugh, L. (1989) A multi-component size-classifying aerosol and gas sampler for ambient air monitoring. Air and Waste Management Association paper 89-140.1.
- [23] Gharib, S. and Cass, G. R. (1984) *Ammonia Emissions in the South Coast Air Basin, Open file report 84-2*. Environmental Quality Laboratory, California Institute of Technology.
- [24] Goodin, W. R., McRae, G. J., and Seinfeld, J. H. (1979) A comparison of interpolation methods for sparse data: application to wind and

- concentration fields. *J. appl. Met.*, **18**, 761–771.
- [25] Gordon, J. I. (1984) Daytime visibility, a conceptual review. *J. Opt. Soc. Am.*, **1**, 1324–1324.
- [26] Gray, H. A. (1986) *Control of Atmospheric Fine Primary Carbon Particle Concentrations*. Ph.D. dissertation, also published as Environmental Quality Laboratory Report 23, California Institute of Technology.
- [27] Gray, H. A., Cass, G. R., Huntzicker, J. J., Heyerdahl, E. K., and Rau, J. A. (1986) Characteristics of atmospheric organic and elemental carbon particle concentrations in Los Angeles. *Environ. Sci. Technol.*, **20**, 580–589.
- [28] Groblicki, P. J., Wolff, G. T., and Countess, R. J. (1981) Visibility reducing species in the Denver “brown cloud” – I. Relationships between extinction and chemical composition. *Atmos. Environ.*, **15**, 2473–2484.
- [29] Hansen, J. E. and Travis, L. D. (1974) Light scattering in planetary atmospheres. *Space Sci. Rev.*, **16**, 527–610.
- [30] Harley, R. A., Hannigan, M. P., and Cass, G. R. (1992) Respeciation of organic gas emissions and the detection of excess unburned gasoline in the atmosphere. *Environ. Sci. Technol.*, **26**, 2395–2408.
- [31] Harley, R. A., Russell, A. G., McRae, G. J., Cass, G. R., and Seinfeld, J. H. (1993) Photochemical modeling of the Southern California Air Quality Study. *Environ. Sci. Technol.*, **27**, 378–388.
- [32] Hasan, H. and Lewis, C. W. (1983) Integrating nephelometer response corrections for bimodal size distributions. *Aerosol Sci. Technol.*, **2**, 443–453.
- [33] Hawkins, R. (1993) personal communication, Fire Management Offi-

- cer, Arroyo Seco Ranger District, U. S. Forest Service.
- [34] Heisler, S. L. and Friedlander, S. K. (1977) Gas-to-particle conversion in photochemical smog: Aerosol growth laws and mechanisms for organics. *Atmos. Environ.*, **11**, 157-168.
- [35] Hering, S. V. (1990) *Southern California Air Quality Study Aerosol Data Management Report, Final Report*. Contract A832-086, California Air Resources Board, Sacramento, California.
- [36] Hering, S. V. and Blumenthal, D. L. (1989) *Southern California Air Quality Study Description of Measurement Activities, Final Report*. Contract A5-157-32, California Air Resources Board, Sacramento, California.
- [37] Hering, S. V. and Friedlander, S. K. (1982) Origins of aerosol sulfur size distributions in the Los Angeles basin. *Atmos. Environ.*, **16**, 2647-2656.
- [38] Hering, S. V. and McMurry, P. H. (1991) Optical counter response to monodisperse atmospheric aerosols. *Atmos. Environ.*, **25A**, 463-468.
- [39] Hering, S. V. and others (1988) The nitric acid shootout: Field comparison of measurement methods. *Atmos. Environ.*, **22**, 1519-1539.
- [40] Hildemann, L. M., Cass, G. R., and Markowski, G. R. (1989) A dilution stack sampler for collection of organic aerosol emissions: Design, characterization and field tests. *Aerosol Sci. Technol.*, **10**, 193-204.
- [41] Hildemann, L. M., Markowski, G. R., and Cass, G. R. (1991a) Chemical composition of emissions from urban sources of fine organic aerosol. *Environ. Sci. Technol.*, **25**, 744-759.
- [42] Hildemann, L. M., Markowski, G. R., Jones, M. C., and Cass, G. R. (1991b) Submicrometer aerosol mass distributions of emissions

- from boilers, fireplaces, automobiles, diesel trucks, and meat-cooking operations. *Aerosol Sci. Technol.*, **14**, 138–152.
- [43] Hildemann, L. M., Russell, A. G., and Cass, G. R. (1984) Ammonia and nitric acid concentrations in equilibrium with atmospheric aerosols: Experiment vs. theory. *Atmos. Environ.*, **18**, 1737–1750.
- [44] Hodkinson, J. R. (1966) Calculations of color and visibility in urban atmospheres polluted by gaseous NO<sub>2</sub>. *Air Water Pollut. Int. J.*, **10**, 137–144.
- [45] Hoffmann, M. R. and Calvert, J. G. (1985) *Chemical Transformation Modules for Eulerian and Deposition Models, Volume II: The Aqueous Phase Chemistry*. EPA 600/3-85/036, U. S. Environmental Protection Agency, Research Triangle Park, North Carolina.
- [46] Houck, J. E., Chow, J. C., Watson, J. G., Simons, C. A., Pritchett, L. C., Goulct, J. M., and Frazier, C. A. (1989) *Determination of Particle Size Distribution and Chemical Composition of Particulate Matter from Selected Sources in California*. California Air Resources Board contract A6-175-32, OMNI Environmental Services, Inc., and Desert Research Institute, Beaverton, Oregon.
- [47] Ingalls, M. N. (1989) On-road vehicle emission factors from measurements in a Los Angeles area tunnel. Paper No. 89-137.3, presented at the Air and Waste Management Association 82nd Annual Meeting.
- [48] Jacob, D. J., Waldman, J. M., Munger, J. W., and Hoffman, M. R. (1985) Fogwater chemistry in an urban atmosphere. *Environ. Sci. Technol.*, **19**, 730–736.
- [49] John, W. and Reischl, G. (1980) A cyclone for size-selective sampling of ambient air. *J. Air Pollut. Control Assoc.*, **30**, 872–876.

- [50] John, W., Wall, S. M., Ondo, J. L., and Winklmayr, W. (1989) *Acidic Aerosol Size Distributions during SCAQS*. Contract A6-112-39, California Air Resources Board, Sacramento, California.
- [51] John, W., Wall, S. M., Ondo, J. L., and Winklmayr, W. (1990) Modes in the size distribution of atmospheric inorganic aerosol. *Atmos. Environ.*, **24A**, 2349-2359.
- [52] Johnson, R. L., Shah, J. J., Cary, R. A., and Huntzicker, J. J. (1981) An automated thermal:optical method for the analysis of carbonaceous aerosol. In Macias, E. S. and Hopke, P. K., editors, *Atmospheric Aerosols: Source/Air Quality Relationships*, chapter 12, pages 223-233, American Chemical Society, Washington, D. C.
- [53] Kaufman, Y. J. (1979) Effect of the earth's atmosphere on contrast for zenith observations. *J. Geophys. Res.*, **84**, 3165-3172.
- [54] Larson, S. M. and Cass, G. R. (1989) Characteristics of summer midday low-visibility events in the Los Angeles area. *Environ. Sci. Technol.*, **23**, 281-289.
- [55] Larson, S. M., Cass, G. R., and Gray, H. A. (1989) Atmospheric carbon particles and the Los Angeles visibility problem. *Aerosol Sci. Technol.*, **10**, 118-130.
- [56] Larson, S. M., Cass, G. R., Hussey, K. J., and Luce, F. (1988) Verification of image processing based visibility models. *Environ. Sci. Technol.*, **22**, 629-637.
- [57] Lawson, D. R. (1990) The Southern California air quality study. *J. Air Waste Manage. Assoc.*, **40**, 156-165.
- [58] Li, W. and Hopke, P. K. (1993) Initial size distribution and hygroscopicity of indoor combustion aerosol particles. *Aerosol Sci. Technol.*,

- 19, 305–316.
- [59] Ligocki, M. P., Liu, H. I. H., Cass, G. R., and John, W. (1990) Measurements of particle deposition rates inside Southern California museums. *Aerosol Sci. Technol.*, **13**, 85–101.
- [60] Lin, C., Baker, M., and Charlson, R. J. (1973) Absorption coefficient of atmospheric aerosol: A method for measurement. *Appl. Opt.*, **12**, 1356–1363.
- [61] Liou, K. (1974) Analytic, two-stream and four-stream solutions for radiative transfer. *J. Atmos. Sci.*, **31**, 1473–1475.
- [62] MacAdam, D. L. (1981) Perceptual significance of colorimetric data for colors of plumes and haze. *Atmos. Environ.*, **15**, 1797–1803.
- [63] Malm, W. C., Molenar, J. V., and Chan, L. L. (1983) Photographic simulation techniques for visualizing the effects of uniform haze on a scenic resource. *J. Air Pollut. Control Assoc.*, **33**, 126–129.
- [64] Matsumura, R. T. and Cahill, T. A. (1991) *Spatial Inhomogeneities in SCAQS Filters*. Contract A832-128, California Air Resources Board, Sacramento, California.
- [65] McMurry, P. H. and Wilson, J. C. (1983) Droplet phase (heterogeneous) and gas phase (homogeneous) contributions to secondary ambient aerosol formation as functions of relative humidity. *J. Geophys. Res.*, **8**, 5101–5108.
- [66] McRae, G. J., Goodin, W. R., and Seinfeld, J. H. (1982) Development of a second-generation mathematical model for urban air pollution – I. Model formulation. *Atmos. Environ.*, **16**, 679–696.
- [67] Meador, W. E. and Weaver, W. R. (1980) Two-stream approximations to radiative transfer in planetary atmospheres: A unified description of

- existing methods and a new improvement. *J. Atmos. Sci.*, **37**, 630–643.
- [68] Meng, Z. and Seinfeld, J. H. (1994) On the source of the submicron droplet mode of urban and regional aerosols. *Aerosol Sci. Technol.*, **20**, 253–265.
- [69] Middleton, W. E. K. (1952) *Vision Through the Atmosphere*. University of Toronto Press.
- [70] Munger, J. W., Jacob, D. J., Waldman, J. M., and Hoffman, M. R. (1983) Fogwater chemistry in an urban atmosphere. *J. Geophys. Res.*, **88**, 5109–5121.
- [71] NRC (National Research Council) (1993) *Protecting Visibility in National Parks and Wilderness Areas*. National Academy Press, Washington, D.C.
- [72] Ouimette, J. R. (1980) *Chemical Species Contributions to the Extinction Coefficient*. Ph.D. thesis, California Institute of Technology.
- [73] Ouimette, J. R. and Flagan, R. C. (1982) The extinction coefficient of multicomponent aerosols. *Atmos. Environ.*, **16**, 2405–2419.
- [74] Pandis, S. N., Harley, R. A., Cass, G. R., and Seinfeld, J. H. (1992a) Secondary organic aerosol formation and transport. *Atmos. Environ.*, **26A**, 2269–2282.
- [75] Pandis, S. N. and Seinfeld, J. H. (1989) Sensitivity analysis of a chemical mechanism for aqueous phase atmospheric chemistry. *J. Geophys. Res.*, **94**, 1105–1126.
- [76] Pandis, S. N., Seinfeld, J. H., and Pilinis, C. (1992b) Heterogeneous sulfate formation in an urban fog. *Atmos. Environ.*, **26A**, 2509–2522.
- [77] Parker, V. B., Wagman, D. D., and Garvin, D. (1976) *Selected Thermodynamic Data Compatible with the CODATA Recommendations*. NB-

- SIR 75-968.
- [78] Penndorf, R. (1957) Tables of the refractive index for standard air and the Rayleigh scattering coefficient for the spectral region between 0.2 and  $20.0\mu\text{m}$  and their application to atmospheric optics. *J. Opt. Soc. Am.*, **47**, 176-182.
- [79] Pierson, W. R., Gertler, A. W., and Bradow, R. L. (1990) Comparison of the SCAQS tunnel study with other on-road vehicle emission data. *J. Air Waste Manage. Assoc.*, **40**, 1495-1504.
- [80] Pilinis, C. and Seinfeld, J. H. (1988) Development and evaluation of an Eulerian photochemical gas-aerosol model. *Atmos. Environ.*, **22**, 1985-2001.
- [81] Plass, G. N. and Kattawar, G. W. (1968) Calculations of reflected and transmitted radiance for earth's atmosphere. *Appl. Opt.*, **7**, 1129-1135.
- [82] Pruppacher, H. R. and Klett, J. D. (1978) *Microphysics of Clouds and Precipitation*. D. Reidel Publishing Company, Boston, Massachusetts.
- [83] Rood, M. J., Covert, D. S., and Larson, T. V. (1987) Temperature and humidity controlled nephelometry: Improvements and calibration. *Aerosol Sci. Technol.*, **7**, 57-65.
- [84] Ruby, M. G. and Waggoner, A. P. (1981) Intercomparison of integrating nephelometer measurements. *Environ. Sci. Technol.*, **15**, 109-113.
- [85] Russell, A. G. and Cass, G. R. (1986) Verification of a mathematical model for aerosol nitrate and nitric acid formation and its use for control measure evaluation. *Atmos. Environ.*, **20**, 2011-2025.
- [86] Russell, A. G., McCue, K. F., and Cass, G. R. (1988) Mathematical modeling of the formation of nitrogen-containing air pollutants. 1. Evaluation of an Eulerian photochemical model. *Environ. Sci. Tech-*

- nol.*, **22**, 263–271.
- [87] Russell, A. G., McRae, G. J., and Cass, G. R. (1984) Acid deposition of photochemical oxidation products – a study using a Lagrangian trajectory model. In deWispelaere, C., editor, *Air Pollution Modeling and Its Application III*, pages 539–564, Plenum Publishing.
- [88] Russell, A. G., McRae, G. J., and Cass, G. R. (1983) Mathematical modeling of the formation and transport of ammonium nitrate aerosol. *Atmos. Environ.*, **17**, 949–964.
- [89] Seinfeld, J. H. (1986) *Atmospheric Chemistry and Physics of Air Pollution*. John Wiley and Sons, New York, New York.
- [90] Slinn, S. A. and Slinn, W. G. N. (1980) Predictions for particle deposition on natural waters. *Atmos. Environ.*, **14**, 1013–1016.
- [91] Sloane, C. S. (1988) Contribution of NO<sub>2</sub> and soot to the discoloration of urban skies. *Atmos. Environ.*, **22**, 2021–2031.
- [92] Sloane, C. S. (1986) Effect of composition on aerosol light scattering efficiencies. *Atmos. Environ.*, **20**, 1025–1037.
- [93] Sloane, C. S. (1984a) *Fortran Algorithm for the Calculation of Light Scattering by Stratified Spheres*. Report RM 11–70, General Motors Research Laboratories, Warren, Michigan.
- [94] Sloane, C. S. (1983) Optical properties of aerosols – comparison of measurement with model calculations. *Atmos. Environ.*, **17**, 409–416.
- [95] Sloane, C. S. (1984b) Optical properties of aerosols of mixed composition. *Atmos. Environ.*, **18**, 871–878.
- [96] Sloane, C. S. and Groblicki, P. J. (1981) Denver's visibility history. *Atmos. Environ.*, **15**, 2631–2638.
- [97] Sloane, C. S., Rood, M. J., and Rogers, C. F. (1991) Measurements of

- aerosol particle size: improved precision by simultaneous use of optical particle counter and nephelometer. *Aerosol Sci. Technol.*, **14**, 289–301.
- [98] Solomon, P. A., Larson, S. M., Fall, T., and Cass, G. R. (1988) Basin-wide nitric acid and related species concentrations observed during the Claremont nitrogen species comparison study. *Atmos. Environ.*, **22**, 1587–1594.
- [99] Stelson, A. W. (1990) Urban aerosol refractive index prediction by partial molar refraction approach. *Environ. Sci. Technol.*, **24**, 1676–1679.
- [100] Stelson, A. W. and Seinfeld, J. H. (1981) Chemical mass accounting of urban aerosol. *Environ. Sci. Technol.*, **15**, 671–679.
- [101] Stelson, A. W. and Seinfeld, J. H. (1982) Relative humidity and temperature dependence of the ammonium nitrate dissociation constant. *Atmos. Environ.*, **5**, 983–992.
- [102] Taback, H. J., Brienza, A. R., Macko, J., and Brunetz, N. (1979) *Fine Particle Emissions from Stationary and Miscellaneous Sources in the South Coast Air Basin*. California Air Resources Board contract A6-191-30, KVB, Inc., Research-Cottrell, Tustin, California.
- [103] Trijonis, J. (1982a) Existing and natural background levels of visibility and fine particles in the rural east. *Atmos. Environ.*, **10**, 2431–2445.
- [104] Trijonis, J. (1982b) Visibility in California. *J. Air Pollut. Control Assoc.*, **32**, 165–169.
- [105] Trijonis, J. (1979) Visibility in the southwest – an exploration of the historical database. *Atmos. Environ.*, **13**, 833–843.
- [106] Trijonis, J., Malm, W., Pitchford, M., and White, W. H. (1990) Visibility: existing and historical conditions – causes and effects. In *State-*

- of-Science/Technology Report 24, Volume III of the National Acid Precipitation Assessment Program (NAPAP)*, The NAPAP Office of the Director, Washington, D. C.
- [107] Twomey, S., Jacobowitz, H., and Howell, H. B. (1966) Matrix methods for multiple-scattering problems. *J. Atmos. Sci.*, **23**, 289–296.
- [108] van de Hulst, H. C. (1957) *Light Scattering by Small Particles*. John Wiley, New York, New York.
- [109] Wagner, K. K. and Allen, P. D. (1990) personal communication of data to Robert A. Harley from the Technical Support Division, California Air Resources Board, Sacramento, California.
- [110] Waldman, J. M. (1985) *Depositional Aspects of Pollutant Behavior in Fog*. Ph.D. thesis, California Institute of Technology.
- [111] Weast, R. C., editor(1985) *CRC Handbook of Chemistry and Physics*, CRC Press, 66th edition, pages B67–B161.
- [112] Wexler, A. S. and Seinfeld, J. H. (1992) Analysis of aerosol ammonium nitrate: Departures from equilibrium during SCAQS. *Atmos. Environ.*, **26A**, 579–591.
- [113] Wexler, A. S. and Seinfeld, J. H. (1991) Second-generation inorganic aerosol model. *Atmos. Environ.*, **25A**, 2731–2748.
- [114] White, W. H. and Roberts, P. T. (1977) On the nature and origins of visibility-reducing aerosols in the Los Angeles air basin. *Atmos. Environ.*, **11**, 803–812.
- [115] Williams, M. D., Treiman, E., and Wecksung, M. (1980) Plume blight visibility model with a simulated photograph technique. *J. Air Pollut. Control Assoc.*, **30**, 131–134.
- [116] Wiscombe, W. (1983) Atmospheric radiation 1975-1983. *Rev. Geo-*

- phys. Space Phys.*, **21**, 997–1021.
- [117] Woodleif, T., editor (1973) *SPSE Handbook of Photographic Science and Engineering*. John Wiley and Sons.
- [118] Wyszecki, G. and Stiles, W. S. (1982) *Color Science*. John Wiley and Sons, second edition.
- [119] Young, T. and Boris, J. (1977) A numerical technique for solving stiff ordinary differential equations associated with the chemical kinetics of reactive flow problems. *J. Phys. Chem.*, **81**, 2424–2427.
- [120] Zhang, X. Q. (1990) *Measurements of Size Resolved Atmospheric Aerosol Chemical Composition with Impactors: Data Integrity and Applications*. Ph.D. thesis, University of Minnesota.
- [121] Zhang, X. Q., McMurry, P. H., Hering, S. V., and Casuccio, G. S. (1993) Mixing characteristics and water content of submicron aerosols measured in Los Angeles and at the Grand Canyon. *Atmos. Environ.*, **27A**, 1593–1607.